UNIVERSITY OF OKLAHOMA

GRADUATE COLLEGE

MULTISTAGE TRIAXIAL TEST ON CONVENTIONAL AND UNCONVENTIONAL ROCKS

A THESIS

SUBMITTED TO THE GRADUATE FACULTY

in partial fulfillment of the requirements for the

Degree of

MASTER OF SCIENCE

By

TITO HENAO
Norman, Oklahoma
2017

MULTISTAGE TRIAXIAL TEST ON CONVENTIONAL AND UNCONVENTIONAL ROCKS

A THESIS APPROVED FOR THE
MEWBOURNE SCHOOL OF PETROLEUM AND GEOLOGICAL ENGINEERING

BY

Dr. Carl Sondergeld, Chair

Dr. Chandra Rai

Dr. Deepak Devegowda

To my wife, Theresa, and my parents, Tito and Martha.
For all their support and love.

Acknowledgments

I thank Dr. Carl Sondergeld and Dr. Chandra Rai for their guidance and thoughtful contributions to my research and professional career. My sincere gratitude to graduate liaison and committee member Dr. Deepak Devegowda who was the first one to open the door to the high quality education I have received from the Mewbourne School of Petroleum and Geological Engineering. Thank you for your trust and guidance through this Master's degree.

My utmost thanks to Gary Stowe, Bruce Spears, Micaela Langevin, Jeremy Jernigen, and Dr. Mark Curtis who contributed to this thesis from their respective roles at the Integrated Core Characterization Center (IC^3). I recognize the work of fellow students and research assistants who helped me converting experimental results into valuable insights, especially Son Dang. I acknowledge IC^3 graduate Aristotelis Pagoulatos for his valuable contributions to the protocol of the multistage triaxial test—the experimental foundation of this thesis.

This thesis was supported by the members of the Unconventional Shale Gas Consortium and the Rock Physics Consortium: Total, Apache, Shell, Devon, BHP Billiton, and Cimarex.

Table of Contents

List of Tables

List of Figures

Abstract

The triaxial test is a technique commonly used to determine the failure stress of rocks in compression. Typically, a series of triaxial tests are needed to establish a failure envelope. Unfortunately, the practical constraint on the number of available samples prohibits a multitude of tests from core recovered from reservoirs. Furthermore, if multiple samples are taken they are offset in depth which introduces geological variability.

This thesis presents the mechanics of a multistage triaxial test (Pagoulatos, 2004) as a more efficient technique to determine the mechanical properties at multiple stress states. Each multistage experiment provides the failure envelope and the pressure dependence of elastic moduli using a single sample. Previous work indicates that there is a static offset between the conventional testing results and the multistage testing results. Thus, a simple rescaling recovers the multi–sample equivalent failure envelope.

In this study, we explore the pore fluid dependence of the mechanical behavior of conventional rocks by testing samples of Berea, Bandera, Lyons, and Tennessee sandstones under drained multistage triaxial tests. Moreover, we extend the scope of the multistage triaxial test to unconventional rocks by testing eight samples from the Eagle Ford and Woodford shales. The effect of preexisting weakness planes remains to be the biggest limitation for multistage testing on shales.

Chapter 1: Introduction

1.1 Brittle Crack Propagation

Crack propagation is more likely to occur in brittle rocks than ductile rocks (Zehnder, 2012). Multiple solid mechanics models (e.g. Inglis, 1913, Tada et al., 1985) have aimed to quantify the stress and strain fields near the tip of a crack upon the action of a remote load. Crack propagation occurs as the stress field is intensified beyond the cohesive forces of its molecular or atomic bounds (Fig. 1). Part of the provided energy is absorbed as elastic strain, to be released upon crack propagation, and a remnant is dissipated as non–recoverable plastic strain.

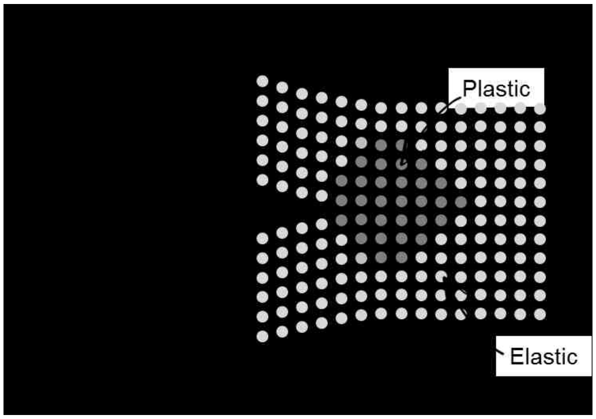

Fig. 1. Simplified molecular model of brittle crack propagation
Note the plastic strain near the tip of the crack, and the broken bounds.

Griffith's (1921) theory of brittle failure states that a crack only propagates if increasing its length, by *c* units, it releases as much elastic strain energy, U_s, as what is thermodynamically required to create two free surfaces, U_γ:

$$\frac{d\mathrm{U}_\gamma}{dc} < \frac{d\mathrm{U}_s}{dc} \tag{1}$$

The critical stress, σ_c, required to release the absorbed elastic energy can be calculated by redefining U_s in terms of the Young's modulus, E, and U_γ in terms of the free surface energy, γ. Thus, Griffith's criterion of brittle failure becomes:

$$\sqrt{\frac{2\gamma E}{\pi c}} < \sigma_c \tag{2}$$

In ductile materials, like metals, a more robust criterion is required to account for the energy dissipated energy in plastic deformation. Irwin (1957) adapted Griffith's brittle failure to account for significant energy dissipation:

$$\sqrt{\frac{2(\gamma+\gamma')E}{\pi c}} < \sigma_c \tag{3}$$

The additional term, γ', accounts for the additional energy dissipated as plastic deformation. In metals, γ might be as low as 0.5 J/m^2 and γ' might be as high as 1000 J/m^2. This implies that, in some cases, σ_c might by systematically underestimated if Irwin's modification is ignored.

1.2 Friction and Cohesion of Brittle Rocks

The strength of rocks under compression depends upon the applied stress state. Compressive failure in reservoir rocks typically follows the frictional behavior distinctive of brittle materials. By association, the compressive strength of rocks is sometimes referred to as brittle strength. Byerlee (1978) defined a universal friction law for rocks by collecting results from fractures induced under triaxial compression and direct shearing, and from artificial saw-cut faults. This compilation suggested a linear relationship between the shear and normal stresses at frictional sliding, Fig. 2:

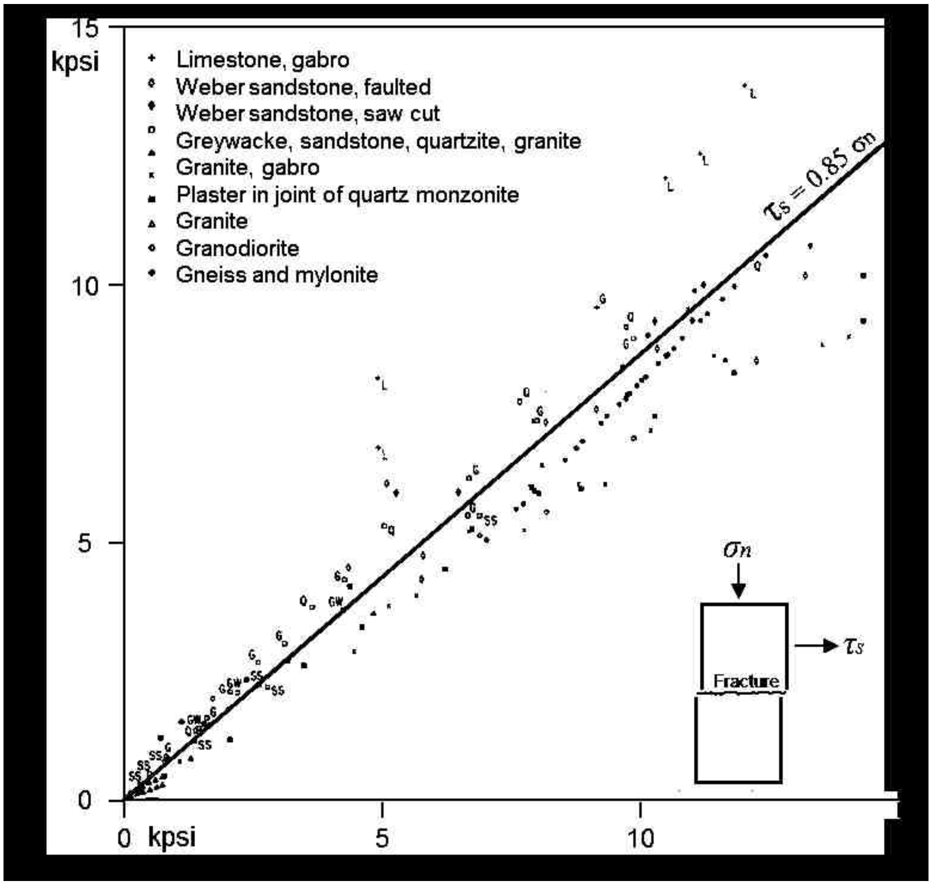

Fig. 2. Shear and normal stresses at failure for broken rocks.
Note: Reprinted from Byerlee (1978)

At high confinement and high temperature, rock failure transitions to follow the steady–state flow behavior typical of ductile materials. The brittle–ductile transition occurs when the friction and the normal stress acting on the shearing planes are high enough to withstand the imposed shear stresses (Orowan, 1960). Scholz (1988) places the transition depth between 11 and 22 km, equivalent to 200 and 500 MPa (29 kpsi and 73 kpsi), Fig. 3:

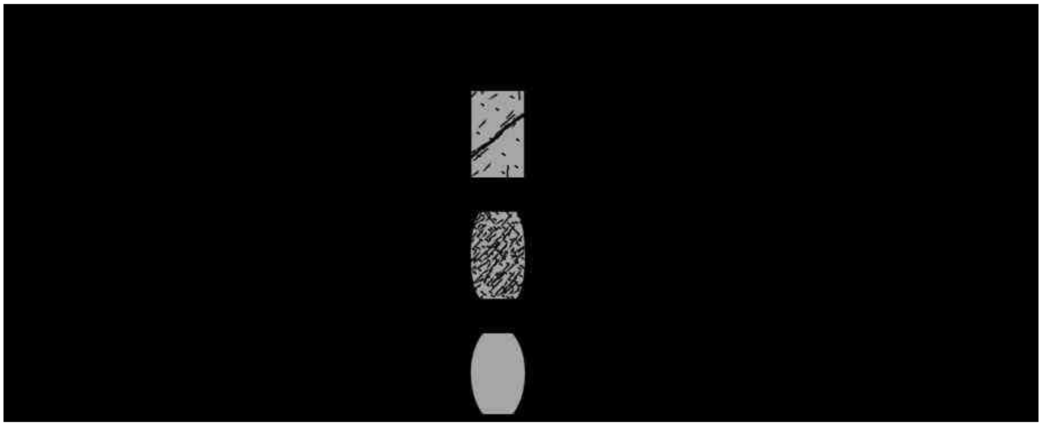

Fig. 3. Brittle–ductile transition of rocks

Note: Based on Evans et al. (1990)

1.3 Stress State at Compressive Failure

The principal stresses, σ_1 and σ_3, acting on a solid failing under compression can be decomposed into their shear and normal components, σ_n and τ_s, acting on its failure plane (Eq. 4 and 5; Fig. 4).

$$\sigma_n = \left(\frac{\sigma_1+\sigma_3}{2}\right) + \left(\frac{\sigma_1-\sigma_3}{2}\right)\cos(2\theta) \tag{4}$$

$$\tau_s = \left(\frac{\sigma_1-\sigma_3}{2}\right)\sin(2\theta) \tag{5}$$

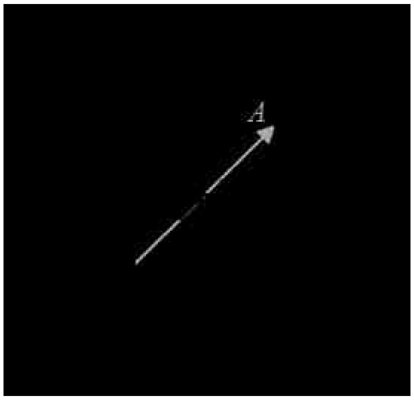

Fig. 4. σ_1 and σ_3 decomposed into σ_n and τ_s

Note: σ_n and τ_s are acting on the direction of reference vector A, by convention, defined by the angle θ from the direction of σ_3.

Note that Eq. 4 and 5 are a set of parametric equations, in terms of θ, representing a 'Mohr's circle' (Mohr, 1882) in the σ_n–τ_s space, Fig. 5:

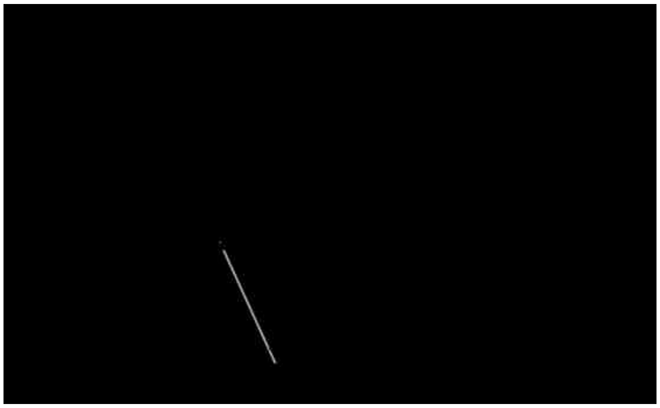

Fig. 5. Schematic of a Mohr's circle in the σ_n–τ_s space.
Note: The angle θ preserves its definition from Fig. 4.

2.1 Linear Mohr–Coulomb Failure Envelope

Coulomb's (1776) friction theory also establishes a linear relationship between τ_s and σ_n at failure. Thus, one might fit a straight line—a linear failure Mohr–Coulomb failure envelope, to describe the stress state at failure, Eq. 6 and Fig. 6:

$$\tau_s = \mu\sigma_n + C \tag{6}$$

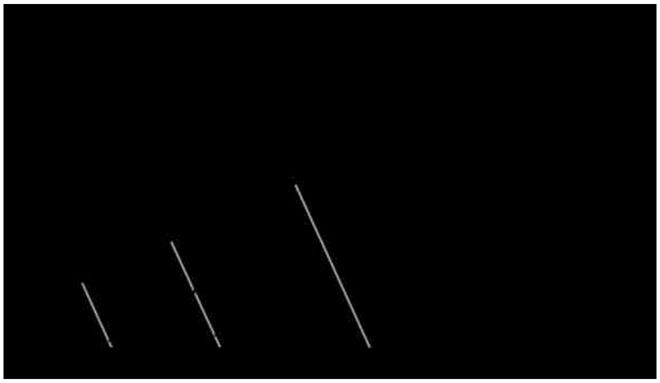

Fig. 6. Schematic of multiple Mohr's circles along with a linear failure envelope.

The slope μ, related to θ (Eq. 7), is the 'friction coefficient', and the intercept C is the 'cohesive strength' or the 'cohesion'.

$$\mu = \tan(\theta) \tag{7}$$

Note that a linear failure envelope in the τ_s and σ_n space implies a linear relationship between σ_1 and σ_3 at failure (Eq. 8, by substituting Eq. 4 and 5 into Eq. 6).

$$\sigma_1 = m\sigma_3 + UCS \tag{8}$$

The slope m and the intercept UCS (Uniaxial Compressive Strength) are related to μ and C by Eq. 9 and 10:

$$m = \frac{\sqrt{\mu^2+1}+\mu}{\sqrt{\mu^2+1}-\mu} \tag{9}$$

$$UCS = 2C\left(\sqrt{\mu^2+1}+\mu\right) \tag{10}$$

In this investigation, the failure envelope is constructed by a linear regression of σ_1 and σ_3 at failure. Eq. 11 and 12 can be solved to calculate μ and C in terms of the slope m and the intercept UCS found with such regression.

$$\mu = \frac{m-1}{2\sqrt{m}} \tag{11}$$

$$C = \frac{UCS}{2\left(\sqrt{\mu^2+1}+\mu\right)} \tag{12}$$

Chapter 2: Multistage Triaxial Testing Methods

The recommended method by the American Society for Testing and Materials (ASTM) for triaxial testing in intact rocks is the standard D7012–14. This protocol starts at an initial hydrostatic stress state (*H* in Fig. 7) to axially compress the sample to its catastrophic failure (*F*) at constant confining pressure. Hence, defining a failure envelope requires a multitude of conventional triaxial tests at as many confining pressures.

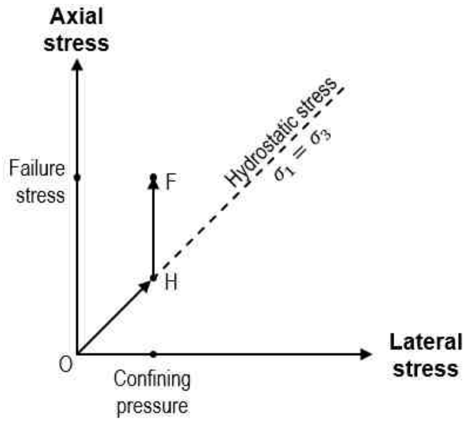

Fig. 7. Schematic of the stress path for the conventional triaxial test.

Three main phases are distinguished during the axial load ($\overrightarrow{HF}$ in Fig. 7, also see Fig. 8):

(1) Crack closure: characterized by an early non–linearity in the strain curves.

(2) Elastic deformation: characterized by the linearity of the strain curves. It occurs as a combined response of the elastic compressibility of equant pores and the elastic compressibility of the mineral matrix of the rock.

(3) Crack growth: characterized by a late non–linearity in the strain curves. It occurs as the preexisting cracks propagate, grow, and coalesce as failure planes, ultimately leading to the catastrophic failure of the rock.

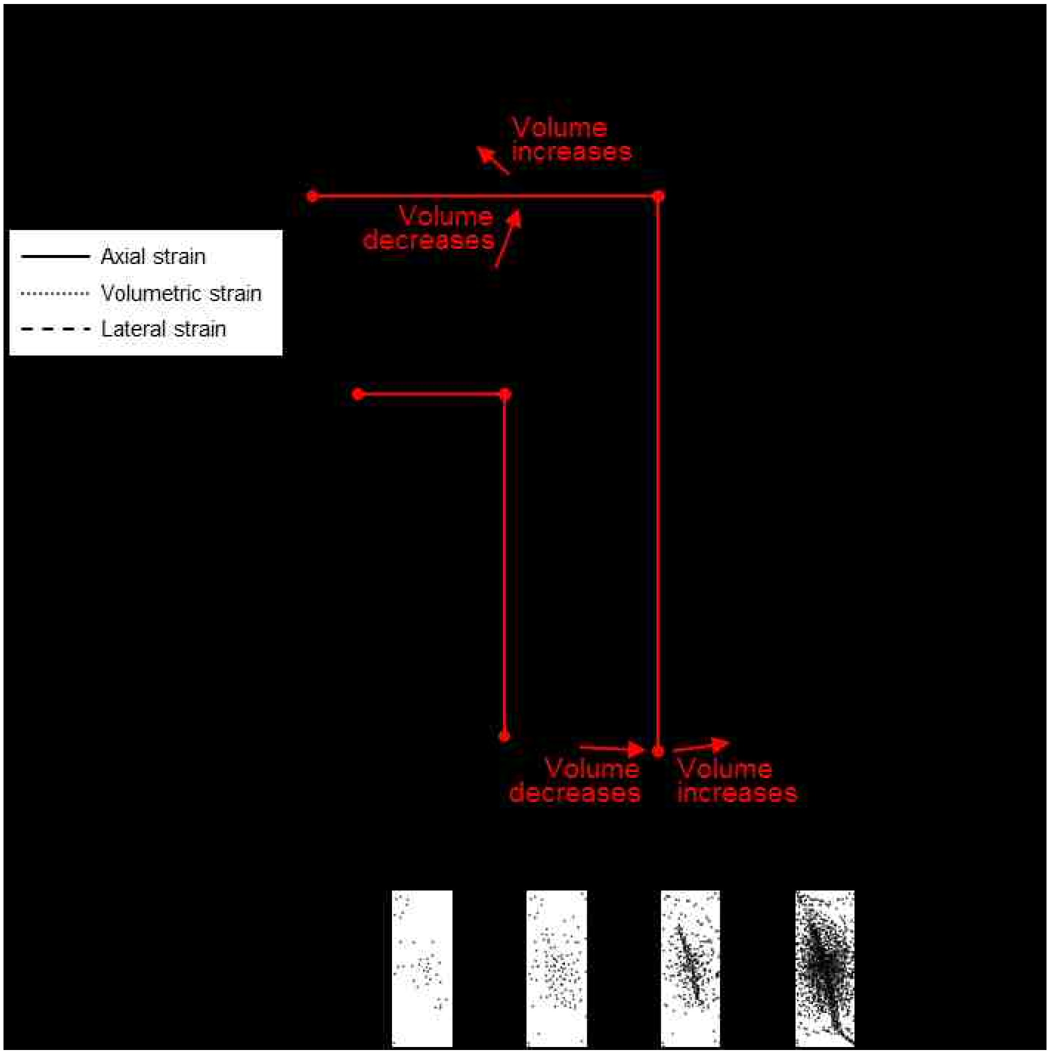

Fig. 8. Schematics for a conventional triaxial test.
Note: (a) Stress–strain curves (after Martin, 1993).
(b) Volumetric strain–axial strain curve (after Martin, 1993).
(c) AE events locations (Hallbauer et. al, 1973).

Different populations of cracks close and grow at different stress states depending on their orientation and aspect ratio (O'Connell and Budiansky, 1974). The extent of each of the three defined phases depends on the rheological properties of the rock and crack closure and crack growth occur more like as a probability distribution rather than as unique stress values.

2.1 Multiple and Continuous Failure State Triaxial Test (Kovári and Tisa, 1975)

Kovári and Tisa (1975) introduced two alternatives to construct a failure envelope using a single sample when sample heterogeneity or availability limit the possibility of performing multiple conventional triaxial tests in as many samples. These two methods differ in their stress paths, as shown in Fig. 9:

[redacted]

Fig. 9. Schematics of the stress paths of the MFS and CFS triaxial test.
Note: (a) Multiple Failure State – MFS triaxial test
(b) Continuous Failure State – CFS triaxial test
Schematic based on Kovári and Tisa (1975)

The MFS triaxial test measures multiple peak stresses (F_i in Fig. 9) at multiple confining stress states. The confining stress is increased by stages while keeping axial stress constant (F_i to H_{i+1}). Kovári and Tisa (1975) briefly approached the question of whether the peak strength decreases in the latest stages by performing a series of reversed MFS triaxial tests on Buchberg sandstone and Carrara marble. Their validation demonstrated that it is possible to obtain a representative failure envelope from the MFS triaxial test as the strength loss between stages is less than 14%, see Fig. 10:

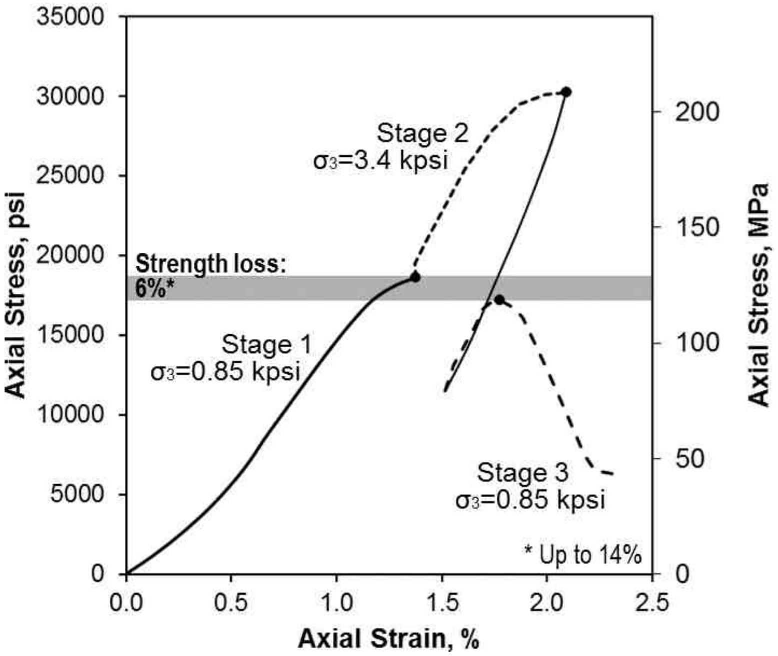

Fig. 10. Stress–strain curve under a reversed MFS triaxial test
Rock: Buchberg sandstone
38% calcite, 35% quartz, 21% feldspar, 6% others
6% porosity; 8 kpsi UCS
Note: Reprinted from Kovári and Tisa (1975)

Additional validation of the MFS triaxial test (Kim and Ko, 1979) suggested that *C* and *μ* can be systematically over and underestimated in brittle sandstones, see Table 1:

Rock	Strength loss	$\frac{C_{MFS} - C}{C}$	$\frac{\mu_{MFS} - \mu}{\mu}$
Buchberg sandstone¹	< 14%	—	—
Carrara marble¹	< 5%	—	—
Pierre shale²	< 5%	+1%	–19%
Raton shale²	< 8%	+14%	–25%
Lyons sandstone²	< 18%	+62%	–34%

Table 1. Strength loss during the last stages of the MFS triaxial test.
Note: (1) Data from Kovári and Tisa (1975)
(2) Data from Kim and Ko (1979)
C and *μ* from conventional triaxial test (single–stage).
C_{MFS} and μ_{MFS} from the MFS triaxial test.

Kovári and Tisa (1975) introduced the CFS triaxial test to describe a continuous failure envelope. The initial axial loading stops upon the detection of the elastic limit on the stress–strain curve (*A* in Fig. 11a and 11b), followed by the simultaneous increment of the confining pressure and the axial load. This is done at a strain rate that makes the stress–strain curve to increase with a constant slope, *ΔP*, lower than the Young's modulus, *E* (see Fig. 11b). The sample is further compressed under constant confining pressure until failure (*F* in Fig. 11a and 11b):

Fig. 11. Schematics of the CFS triaxial test.
Note: (a) Stress path
(b) Axial stress–strain curve
Schematic based on Kovári and Tisa (1975)

A series of failure envelopes for Gotthard granite samples inferred from the CFS triaxial are presented in Fig. 12. Note that the conventional test appears to be a tangent to the CFS triaxial test. The effect of the arbitrary and predefined value of slope *ΔP* was also studied in a series of CFS triaxial tests in Carrara marble samples (Fig. 13). Note that the lower the slope *ΔP*, the lower the slope *m* and the higher the *UCS*, associated with μ by Eq. 11 and with *C* by Eq. 12 respectively.

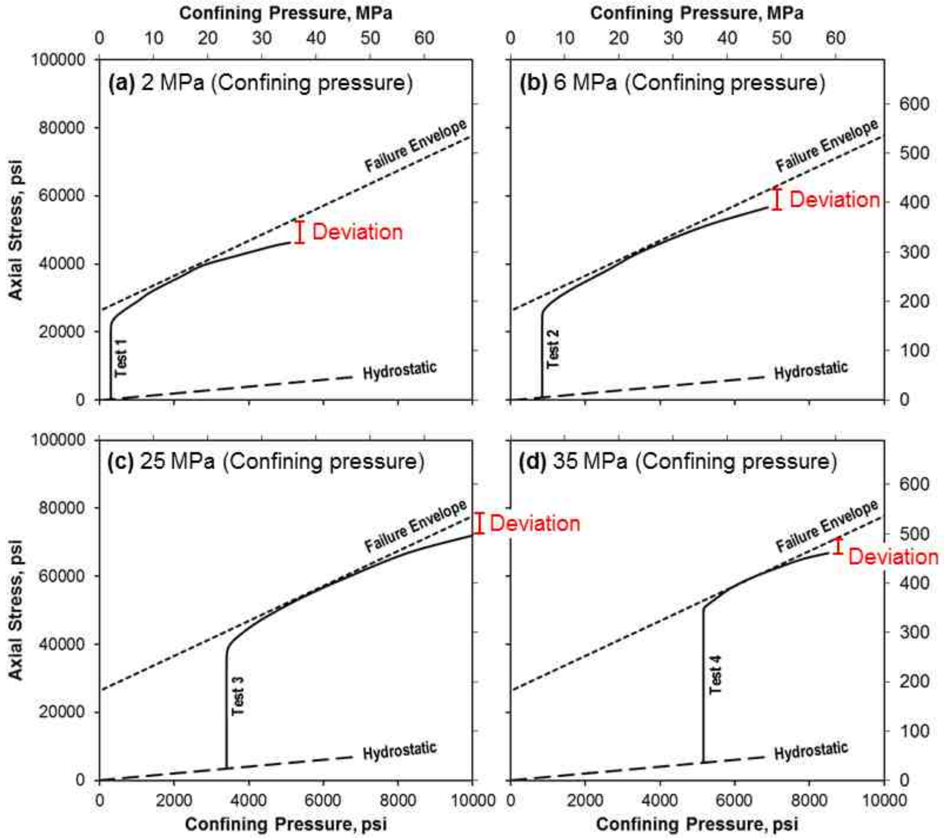

Fig. 12. Failure envelope from the CFS test at confining pressures (a) 2 MPa, (b) 6 MPa, (c) 25 MPa, and (d) 35 MPa.

Rock: Gotthard granite (28% quartz, 59% feldspars, 13% others; 1 % porosity; 24 kpsi *UCS*)

Note: Upper dashed line: Linear failure envelope from the conventional triaxial testing.
Continuous line: Failure envelope from the CFS triaxial test.
Reprinted from Kovári and Tisa (1975)

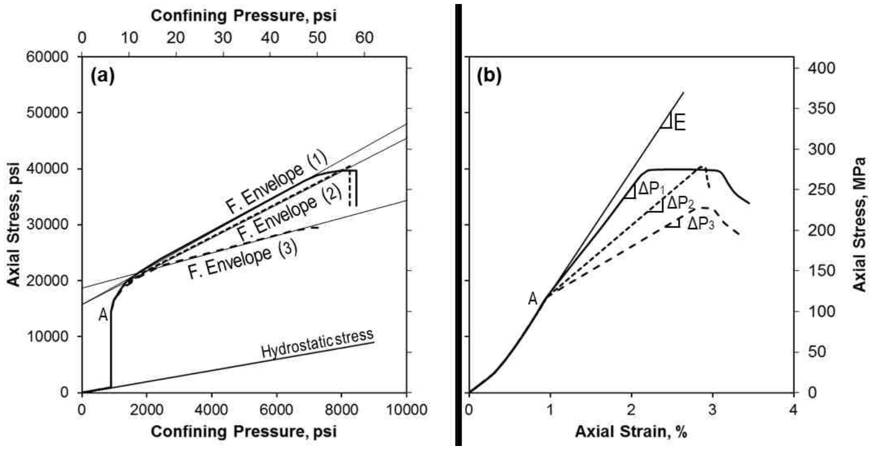

Fig. 13. Effect of ΔP on the failure envelope from the CFS triaxial test

Rock: Carrara marble (100% calcite; <1% porosity, 16 kpsi *UCS*)

Note: (a) Failure envelopes and stress path.
(b) Axial stress–strain curves for $\Delta P_3 < \Delta P_2 < \Delta P_1$
Reprinted from Kovári and Tisa (1975)

2.2 Modified Multiple Failure State Triaxial Test (Crawford and Wylie, 1987)

Crawford and Wylie (1987) pointed that the success of the multistage triaxial testing techniques depends on avoiding sample damage. This lead them to propose two modifications to the MFS test described by Kovári and Tisa (1975):

(1) To stop the axial loading upon the detection of the crack growth onset (f_i in Fig. 14, with $i = 1, 2, 3\ldots$), instead of the peak strength.

(2) To return to the initial hydrostatic stress state (H_i in Fig. 14) after each stage, going through hydrostatic loading in between stages.

Fig. 14. Stress path of the modified MFS triaxial test
Note: Schematic based on Crawford and Wylie (1987)

The crack growth onset is proposed to be detected by two alternatives based on the net volumetric strain (see Fig. 15):

(1) The volumetric strain returns to zero, meaning that the crack growth volume equals the summation of the crack closure and pore compression volumes.

(2) The volumetric strain reaches a critical deflection point, meaning the net volumetric strain switches from closure induced–compaction to crack growth dilatancy.

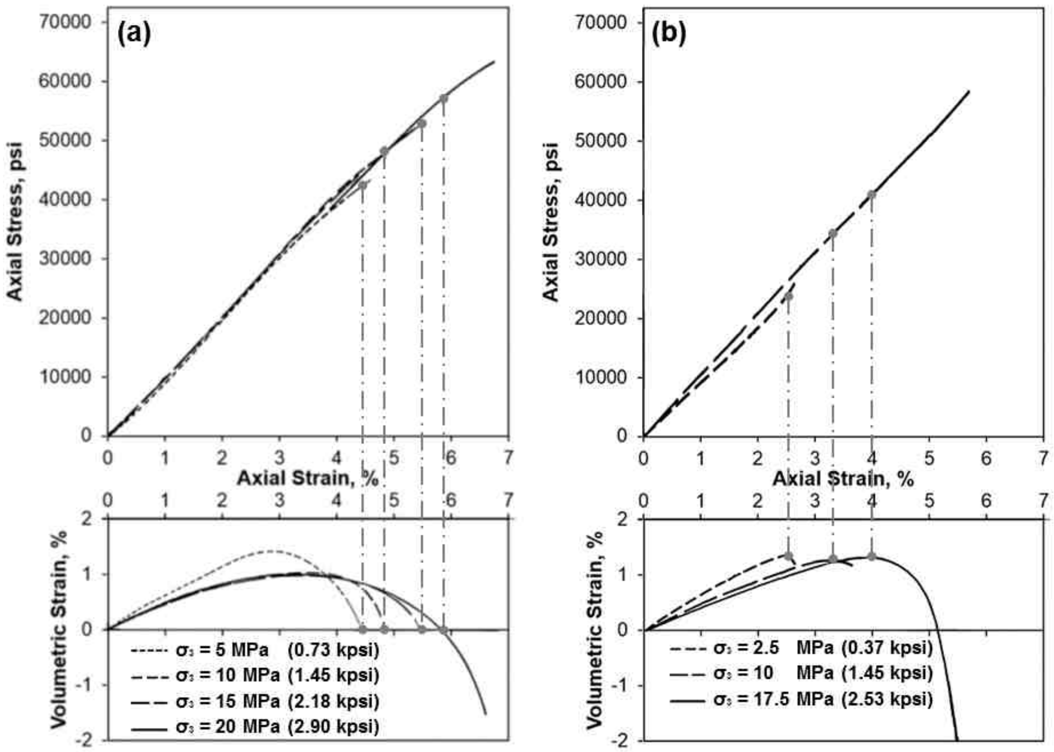

Fig. 15. Detected crack growth onset
Rock: Lac du Bonnet granite
<1% porosity, 34 kpsi UCS
Note: Top: Axial stress–axial strain
Bottom: Volumetric strain–axial strain
(a) Zero volumetric strain criterion
(b) Deflection of the volumetric strain criterion
After Crawford and Wylie (1987)

Fig. 16 presents two failure envelopes for the Lac du Bonnet granite derived from each termination criterion. Note that using the zero volumetric strain criterion significantly underestimates the slope *m* as there is a significant strength loss in the last part of the test. Conversely, the deflection point yields a better estimation of slope *m* but significantly underestimates the *UCS*.

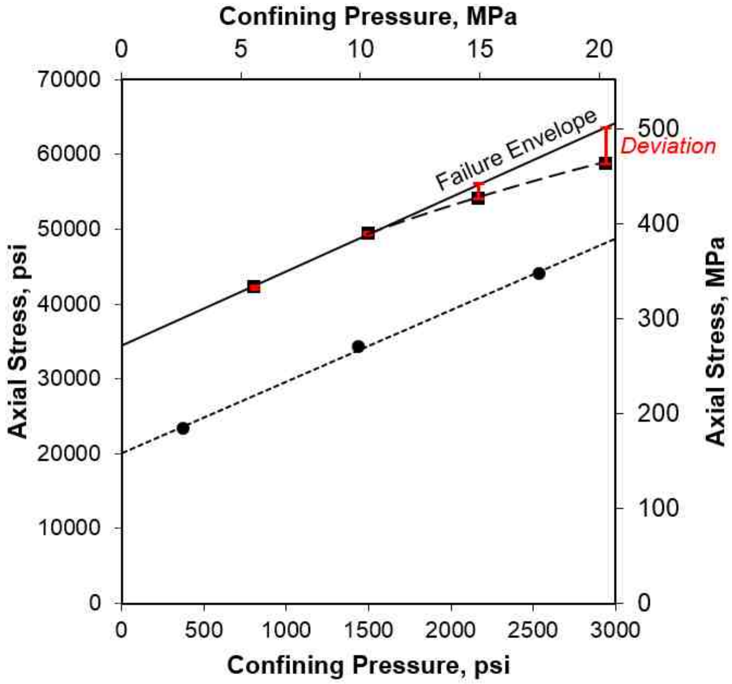

Fig. 16. Failure envelope from conventional and modified MFS triaxial testing.
Rock: Lac du Bonnet granite
<1% porosity, 34 kpsi UCS
Note: (1) Continuous line: Linear failure envelope from conventional triaxial testing.
(2) Upper dashed line: Modified MFS based on the zero volumetric strain criterion.
(3) Lower dashed line: Modified MFS based on the deflection point criterion.
After Crawford and Wylie (1987).

2.3 Multistage Triaxial Test (Pagoulatos, 2004)

Pagoulatos (2004) adopted the termination criterion based on the deflection of the volumetric strain described by Crawford and Wylie (1987), but continuing the last loading stage until failure (*F* in Fig. 17). Hence, the intercept *UCS* is inferred by linear extrapolation using *F* and *m'*, which is assumed to be equal to the slope *m* of the failure envelope in the σ_1–σ_3 space, see Fig. 17. This simple rescaling recovers static offset between the single–stage testing results and the multistage testing results.

Fig. 17. Schematic of the stress path of the multistage triaxial test
Note: *UCS* extrapolated from *F* (i.e. failure stress) using slope *m'*
Slope *m'* is assumed to be equal to failure envelope slope *m*
Based on Pagoulatos (2004)

Pagoulatos (2004) extensively tested this methodology in Berea sandstone yielding a failure envelope of $\tau_s = 0.62\ \sigma_n + 2.3$ kpsi, broadly comparable to the failure envelope from the conventional triaxial test, $\tau_s = 0.62\ \sigma_n + 2.1$ kpsi:

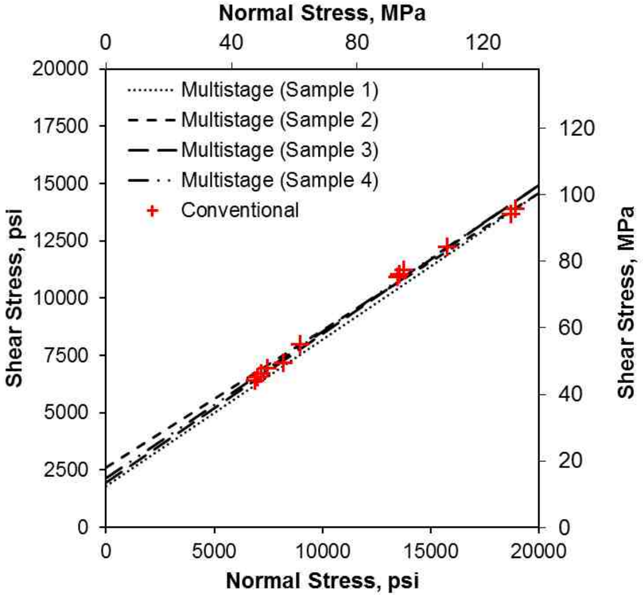

Fig. 18. Linear failure envelopes inferred from conventional and multistage testing.
Rock: Berea sandstone
Note: (1) Discreet data points from conventional triaxial (12 samples)
(2) Dashed lines from multistage triaxial test (4 samples)
Based on Pagoulatos (2004)

Chapter 3: Mechanical Testing Equipment

All the mechanical tests reported here were carried out using a GCTS RTX–1500 Triaxial Testing System capable of independently applying axial load, and confining pressure up to 335 kip, and 10 kpsi, Fig. 19:

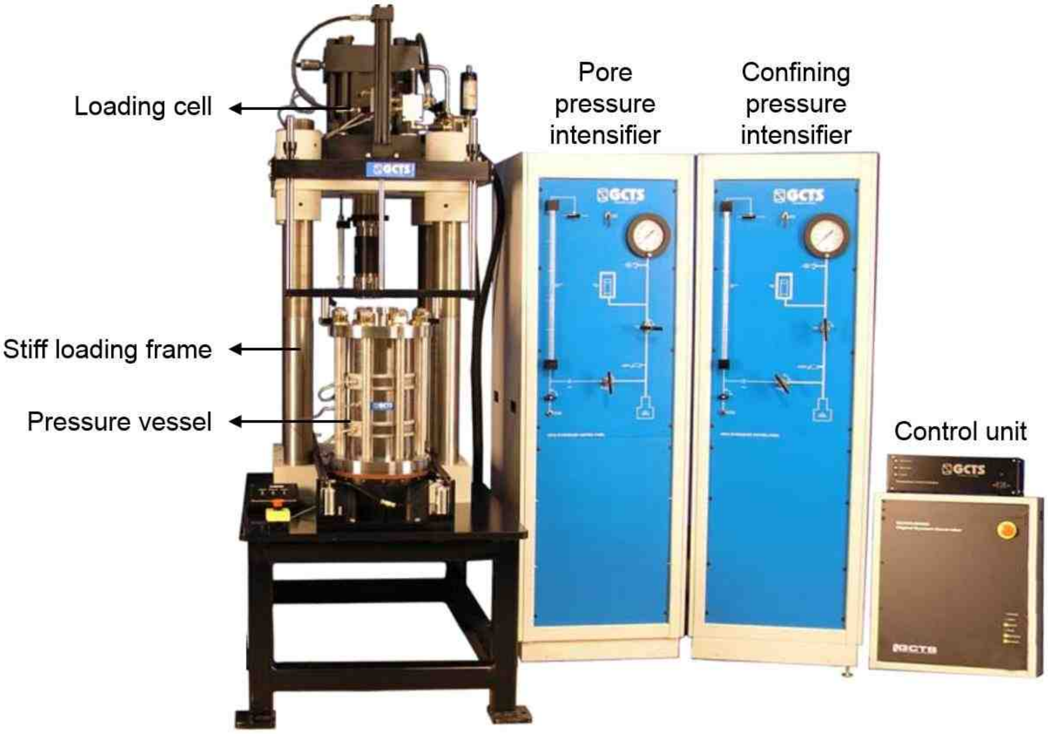

Fig. 19. GCTS RTX–1500 Triaxial Testing System (GCTS, 2008).

Two loading platens were used to transfer the axial force from the piston of the triaxial testing system to the sample (Fig. 20). The samples were jacketed with a polyolefin shrinking tubing to prevent intrusion from the confining fluid. A thin layer of silicon–based vacuum grease and a pair of nitrile o–rings completed the seal between the jacket and the platens.

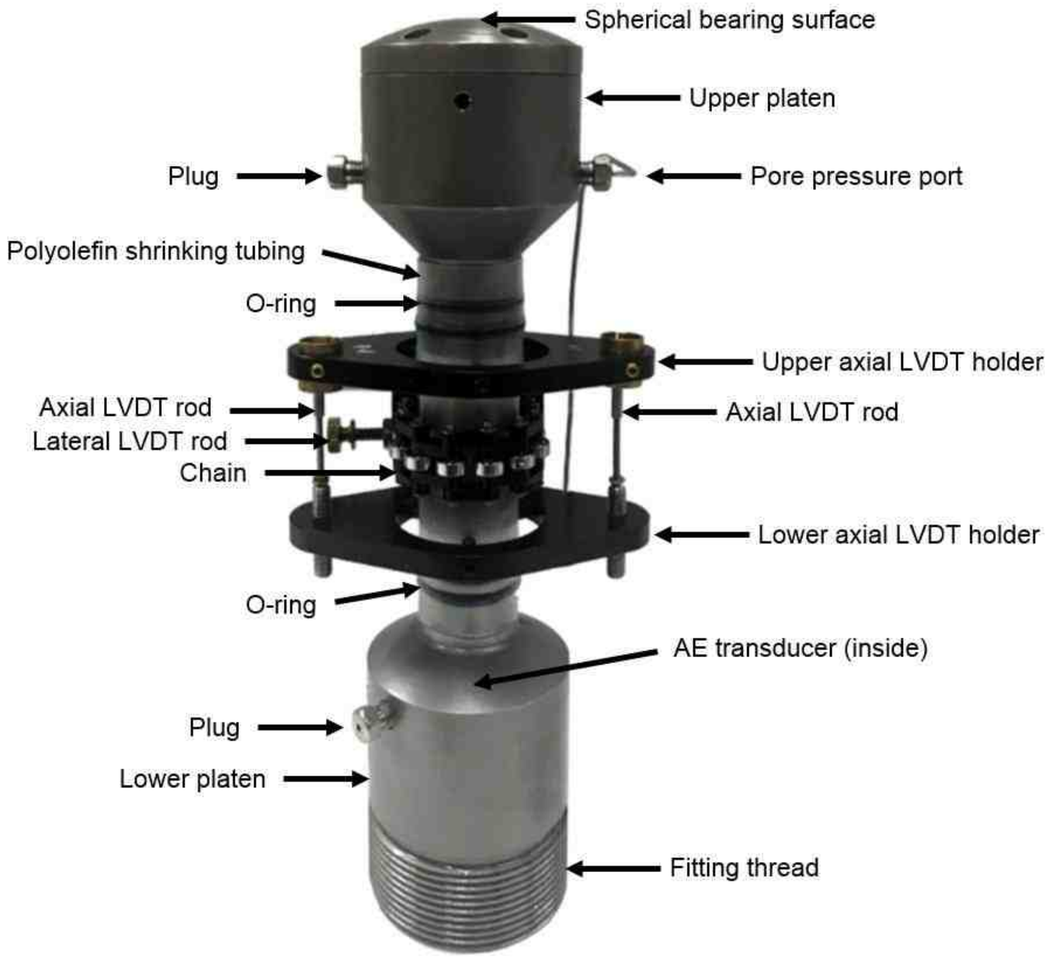

Fig. 20. Rock deformation device, and loading platens.
Note: (1) The upper loading platen and its pore pressure port.
(2) The lower loading platen and the internal AE transducer.
(3) The axial and lateral displacement sensors–LVDTs.

3.1 Strain Measurements

Two Linear Variable Differential Transformers (LVDT) were used to measure the axial displacement, ΔL. The axial strain, ε_{axial}, was calculated by dividing average axial displacement, ΔL_{avg}, by the initial length of the sample, L:

$$\varepsilon_{\mathrm{axial}} = \frac{\Delta \mathrm{L}_{\mathrm{avg}}}{\mathrm{L}} \tag{13}$$

A roller chain and a third LVDT were mounted around the jacketed sample to measure its perimeter change, Fig. 21:

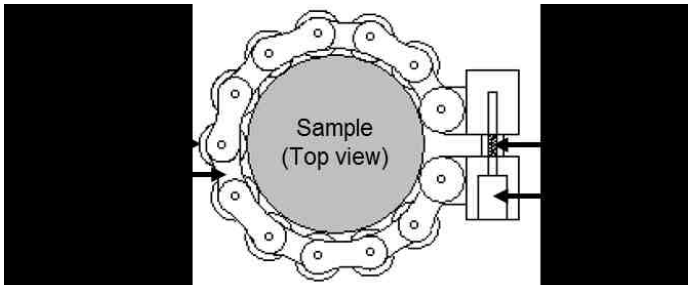

Fig. 21. Top view of the lateral deformation device (GCTS, 2008).

The average radial displacement, ΔR_{avg}, was calculated as a function of the measured change in the perimeter, Δp, the length of the chain, L_c, the chain rollers radius, r, and the initial radius of the sample, R:

$$\Delta R_{avg} = \frac{\pi \Delta p}{\sin\left(\pi - \frac{L_c}{2R+2r}\right) + \left(\frac{L_c}{2R+2r}\right)\cos\left(\pi - \frac{L_c}{2R+2r}\right)} \tag{14}$$

The average lateral strain, $\varepsilon_{lateral}$, is calculated by dividing ΔR_{avg} by R, and the volumetric strain is calculated a function of ε_{axial} and $\varepsilon_{lateral}$:

$$\varepsilon_{lateral} = \frac{\Delta R_{avg}}{R} \tag{15}$$

$$\varepsilon_{vol} = \varepsilon_{axial} + 2\varepsilon_{lateral} \tag{16}$$

3.2 Acoustic Emissions Monitoring

A 1 MHz piezoelectric transducer placed inside the lower loading platen senses the Acoustic Emissions (AE) during the test. The raw signal from the transducer is pre–amplified by 40 dB and recorded by a DiSP Acoustic Emission Workstation™, Fig. 22:

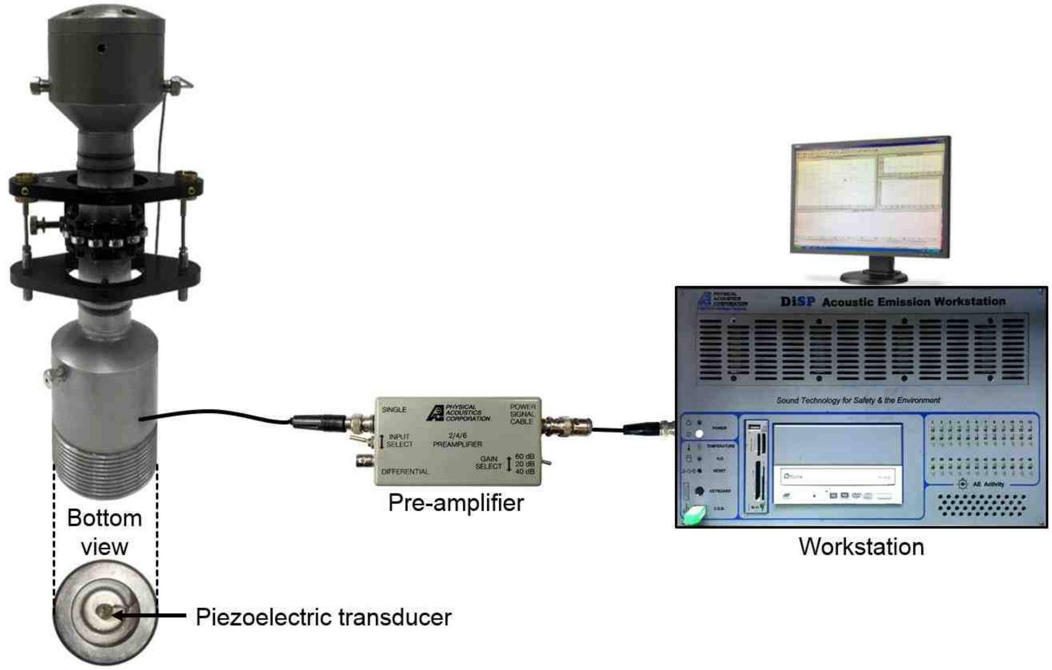

Fig. 22. AE monitoring system.

Note: Left: Piezoelectric transducer inside the lower platen rock deformation device.
Center: Signal preamplifier.
Rigth: DiSP Acoustic Emission Workstation™.

The recording threshold for the AE activity is set 1 dB above the background noise, typically between 70 and 85 dB. A pencil–lead breakage (PLB) test (Hsu and Breckenridge, 1981) is performed before each stage to set the noise threshold.

Chapter 4: Sample Preparation

4.1 Sandstones

Multiple vertical sandstone plugs of 2.0″ long by 1.0″ in diameter were cored, cut, and polished for a series of multistage triaxial tests. An additional suite of horizontal disks of 1.5″ in diameter by 0.75″ thick were prepared for Brazilian tensile testing. A schematic of the coring orientations, with respect to the bedding planes is presented in Fig. 23. Photographs are presented in Fig. 24.

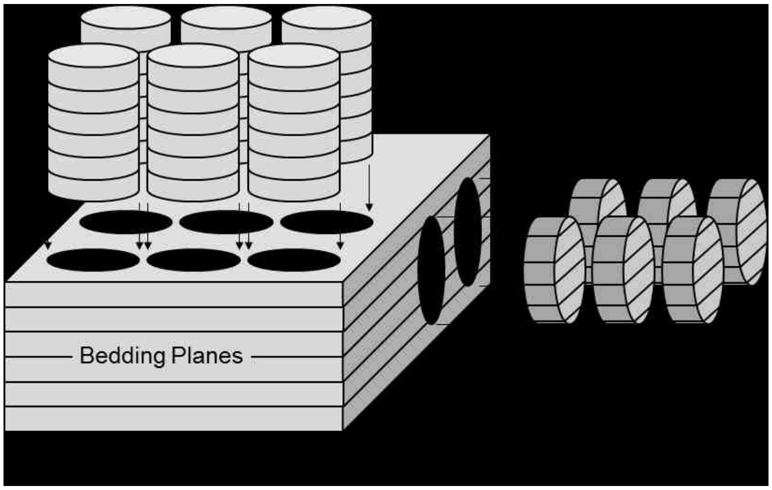

Fig. 23. Schematic of the coring orientations for the sandstone samples.
Note: Vertical plugs for triaxial testing
Horizontal disks for Brazilian tensile testing.
The selected orientations were intended to reduce sample heterogeneity.

The samples were cleaned in a Soxhlet extractor and dried in a vacuum oven for over 24 hours at 100 °C. 'Dry' measurements are reported for plugs and disks tested under ambient temperature and humidity conditions. 'Wet' measurements refer to brine (distilled water + 20000 ppm of KCl), and dodecane saturated samples. All the tests were done under 'drained conditions' allowing the saturating fluids to escape the pores.

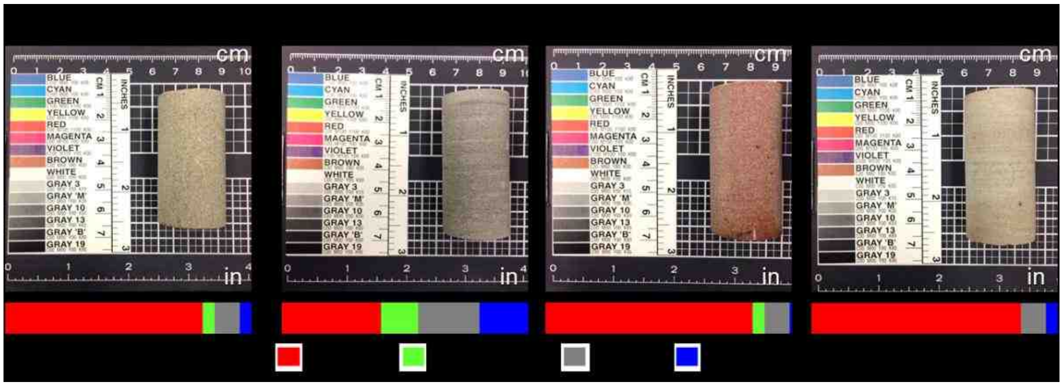

Fig. 24. Photographs of the sandstones core plugs.
Note: Horizontal bars are mineral composition, in wt% (see Table 1).

4.2 Shale

Four horizontal plugs from the Eagle Ford shale and four Woodford shale were cored, cut, and polished. All samples were 1.0″ in diameter and lengths varied between 1.5″ and 2.0″ (see Table 2). The shale samples were tested at native saturation, drained conditions, ambient temperature, and ambient humidity. A schematic of the coring orientations is shown in Fig. 25. Photographs of the shale plugs are presented in Fig. 26.

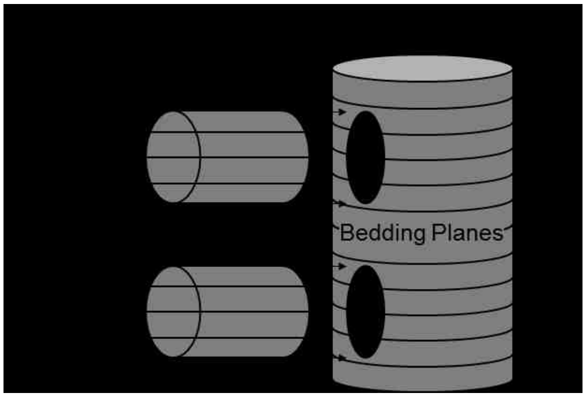

Fig. 25. Schematic of the coring orientations for the tested shales.
Note: Horizontal plugs 1 and 2 are from different depths.
No additional samples were taken for tensile testing.

Fig. 26. Photographs and schematics of the tested shales.

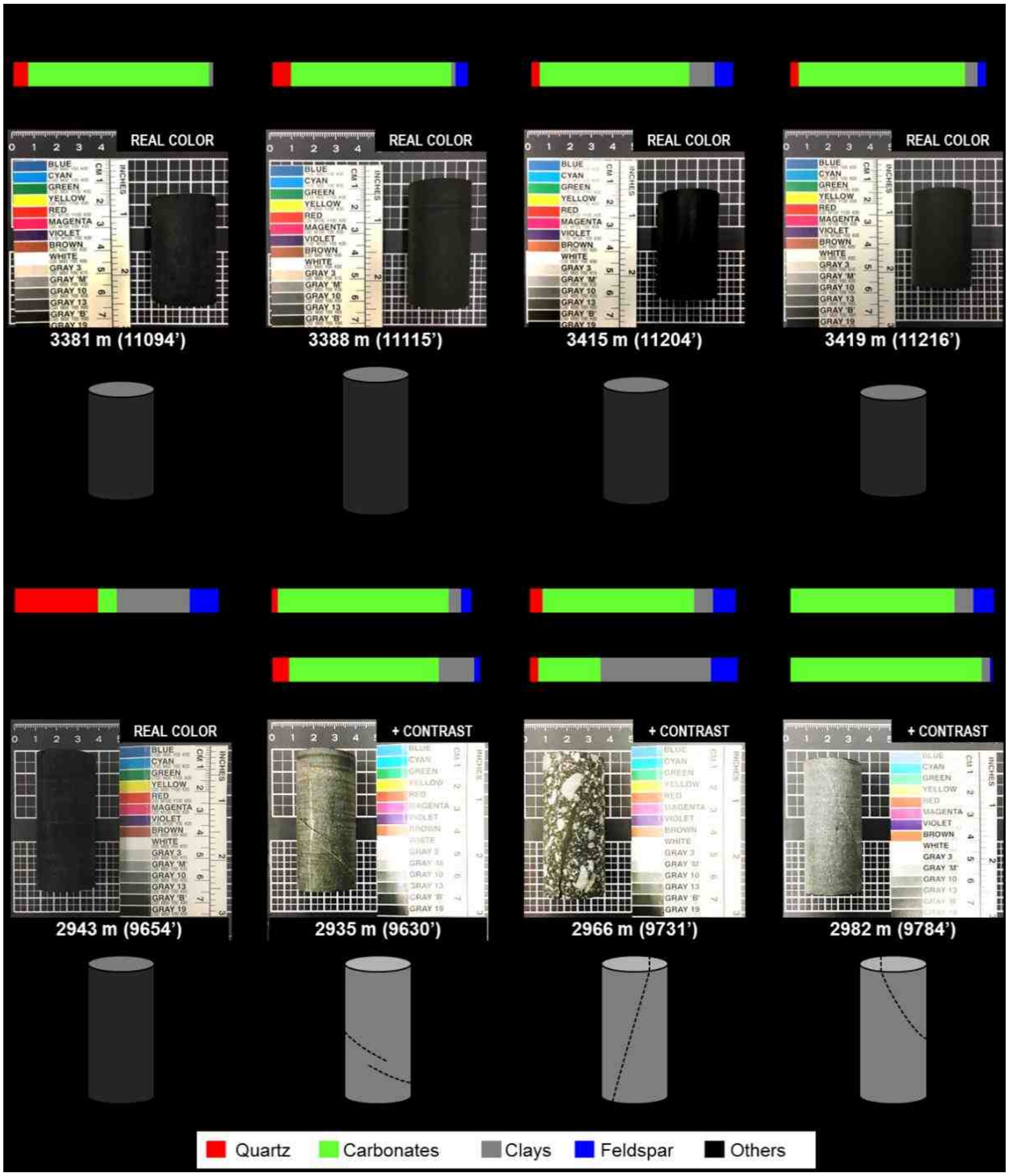

Note: Top: Eagle Ford shale.
Bottom: Woodford shale.

1. Horizontal bars are matrix and vein composition, in wt% (see Table 2).
2. Woodford samples from 9630', 9731', and 9784' presented preexisting veins.
3. Improved contrast and brightness of the photographs of the veined samples.
4. Woodford sample 9731' should be described as a breccia rather than a shale (maximum and average fragment size of 1.2 and 0.25 cm).

Chapter 5: Sample Characterization

Table 2 summarizes the petrophysical properties of the entire inventory of samples. The standardized procedures regarding the petrophysical characterization of the samples are described next.

		Sandstones				Eagle Ford shale				Woodford Shale			
		Bandera	Berea	Lyons	Tennessee	11094.89'	11115.35'	11204.47'	11216.15'	9654.29'	9630.94'	9731.26'	9784.58'
Length (in)		2.0	2.0	2.0	2.0	1.6	2.0	1.6	1.5	2.0	2.0	2.0	2.0
Porosity (%)		19	20	7	6	6	6	4	5	9	1	5	2
Permeability (md)		40	160	0.02	0.01	–	–	–	–	–	–	–	–
Mean grain size (μm)		170	160	190	175	–	–	–	–	–	–	–	–
Total Organic Content (wt%)		0.5	0.3	0.1	0.4	5.9	6.1	4.8	4.9	2.6	0.3	1.8	0.4
Matrix Composition (wt %)	Quartz	40	80	85	85	7	9	4	40	4	3	6	0
	Carbonates	15	5	5	0	87	77	72	9	80	82	73	79
	Clays	25	10	10	10	2	2	12	35	6	6	9	9
	Feldspars	20	5	0	5	0	6	9	14	4	5	11	10
	Others	0	0	0	0	4	6	3	2	6	4	1	2

		Veins		
Orientation (°)		33	67	74
Mineral Coating Composition (wt%)	Quartz	8	4	0
	Carbonates	72	30	92
	Clays	17	53	4
	Feldspars	3	13	1
	Others	0	0	3

Table 2. Inventory of samples.

Note: (1) Porosity from helium expansion measurements on entire (sandstones) and crushed (shales) samples
(2) Permeability from Klinkenberg–corrected pressure decay (only in sandstones)
(3) Mean grain size from micro–CT image analysis (only in sandstones)
(4) Total Organic Content from combustion, non–dispersive infrared detection
(4) Composition from FTIR spectroscopy analysis
(5) Veined samples are highlighted on gray
    (5.2.) Orientation from micro–CT imaging and from the orientation of σ_3
    (5.1.) Coating scratched after failure for composition analysis

5.1 Porosity Measurements

The porosity of the samples was measured using a Boyle's Law porosimeter. The sandstone samples were placed inside a chamber of known volume, v_1, at low pressure, P_1 (Fig. 27). This chamber is connected to a second chamber with reference volume, v_2, and pressurized with helium, typically at P_2 = 100 psia.

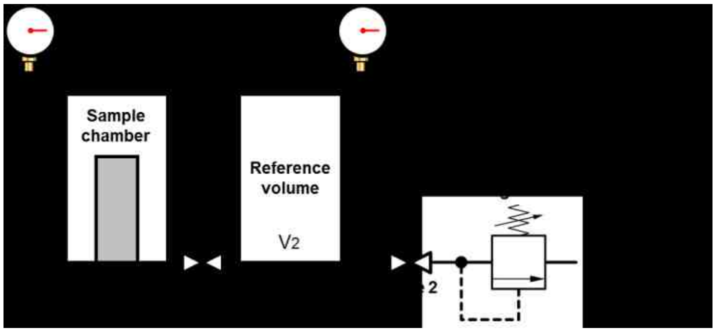

Fig. 27. Boyle's Law porosimeter
Note: After Monicard (1980)

The pressure in both chambers, P_f, after the valve 2 is opened, accounts for the expansion of the helium in the sample chamber. Boyle's Law is used to determine the grain volume, v_g, which in turn is used to calculate porosity, ϕ, in terms of the bulk rock volume, v_b:

$$\mathrm{v_g} = \frac{\mathrm{v_1(P_f - P_1) + v_2(P_f - P_2)}}{\mathrm{P_f - P_1}} \tag{17}$$

$$\phi = \frac{\mathrm{v_b - v_g}}{\mathrm{v_b}} \tag{18}$$

Katastathis (2007) proposed to shorten the long equilibration times that are required for shales by crushing the samples. Thus, the grain volume is inferred and corrected by the sample mass lost during crushing, m_{loss}:

$$\mathrm{v_g^*} = \mathrm{v_g} + \frac{\mathrm{m_{loss}}}{\rho_\mathrm{g}} \tag{19}$$

5.2 Permeability Measurements

The absolute permeability of the sandstones was determined using the pressure decay technique to measure the Klinkenberg–corrected permeability to helium to a resolution of 0.001 md.

5.3 Mineral Composition Measurements

The mineral composition of the rocks, and the mineral coating of the veins (scratched after failure) was quantified using transmission Fourier Transform Infrared (FTIR) spectroscopy. A small portion of the sample is finely crushed, sieved (< 25 μm), heated, and ashed to remove any trace of organic matter. The processed powder carefully weighed and mixed with potassium bromide (KBr) and pressed under 10 kpsi to create a 13 mm disk, transparent to mid–infrared radiation. The disk is placed inside the spectrometer in the path of an infrared beam to record the absorbance of its spectrum, which is the sum of the products of the absorptivity of each individual mineral, ε_i, their concentration, c_i, and the path length, l_i (see Beer's law). An inversion scheme (Sondergeld and Rai, 1993) based on characteristic absorption spectra of each mineral is used to find c_i, as weight percentage:

$$\mathrm{A} = \sum_{\mathrm{i}=1}^{\mathrm{n}} \varepsilon_{\mathrm{i}}\, \mathrm{l}_{\mathrm{i}} \mathrm{c}_{\mathrm{i}} \tag{20}$$

5.4 Total Organic Content Measurements

The Total Organic Content (TOC) was measured using a LECOs' CS844 Series Carbon Determinator™. A small portion of the crushed sample was pre–

treated with hydrogen chloride (HCl) to remove any trace of carbonates, i.e. inorganic carbon. The sample is then combusted to transform whatever organic carbon is present to carbon dioxide. TOC is measured by a non-dispersive infrared detection cell as weight percentage.

5.5 Ultrasonic Velocity Measurements

The travel times, of the ultrasonic compressional 1 MHz and shear 500 kHz waves, Δt_p and Δt_s, were measured under confining pressure. The samples were jacketed with rubber tubing to prevent intrusion from the confining fluid. The compressional and shear waves velocities, V_p and V_s, were calculated from the sample length and the observed travel times:

$$\mathrm{V_p} = \frac{\mathrm{L}}{\Delta \mathrm{t_p}} \tag{21}$$

$$\mathrm{V_s} = \frac{\mathrm{L}}{\Delta \mathrm{t_s}} \tag{22}$$

The dynamic Poisson's ratio, v_{dyn}, and Young's modulus, E_{dyn}, are calculated from the sample bulk density and the wave velocities:

$$v_{dyn} = \frac{1}{2} \frac{\left(\mathrm{V_p}/\mathrm{V_s}\right)^2 - 2}{\left(\mathrm{V_p}/\mathrm{V_s}\right)^2 - 1} \tag{23}$$

$$E_{dyn} = \rho \left(\mathrm{V_p}^2 - \frac{4}{3}\mathrm{V_s}^2\right)(3 - 6\, v_{dyn}) \tag{24}$$

Chapter 6: Results and Discussion

The complete stress paths and failure envelopes from all the multistage triaxial tests are presented in Appendix I. The stress–strain curves, and AE activity for each one of the testing stages are compiled in Appendix II.

6.1 Sandstones

We validated our implementation of the multistage triaxial test by comparing the inferred μ, C, and UCS for Berea sandstone tested at dry and brine saturated conditions with literature values, Table 3 and Fig. 28:

Sample	Fluid	Reference	Test	μ	C, kpsi	UCS, kpsi	T, kpsi
Berea Sandstone	Dry	This work	Multistage Triaxial + Brazilian	0.64	2.2	8.1	0.7
		Handin and Hager (1957)	Conventional Triaxial	0.52	3.1	10.2	-
		Gnirk and Cheatham (1963)	Conventional Triaxial + Brazilian	0.56	2.4	8.1	0.4
		Wilhelmi and Somerton (1967)	Conventional Triaxial	0.66	2.2	8.3	-
		Aldritch (1969)	Conventional Triaxial	0.67	2.7	9.9	-
		Twiss and Moores (1992)	Conventional Triaxial	0.49	3.5	11.2	-
		Baud et al. (2000)	Conventional Triaxial	0.56	-	-	-
		Pagoulatos (2004)	Conventional Triaxial	0.62	2.3	8.1	-
		Pagoulatos (2004)	Multistage Triaxial	0.62	2.1	7.7	-
	Brine	This work	Multistage Triaxial + Brazilian	0.60	1.7	6.0	0.4
		Aldritch (1969)	Conventional Triaxial	0.65	2.3	8.4	-
		Baud et al. (2000)	Conventional Triaxial	0.51	-	-	-
	Dodecane	This work	Multistage Triaxial + Brazilian	0.62	2.0	7.2	0.7

Table 3. μ, C, UCS, and T of Berea sandstone (dry and wet).

Note: (1) Results from this work are highlighted, strain rate 5×10^{-6} s^{-1} (multistage triaxial test, Pagoulatos' (2004) method) and 0.27 kip/min (Brazilian tensile test).
(2) The literature values have been constrained to a linear failure envelope.

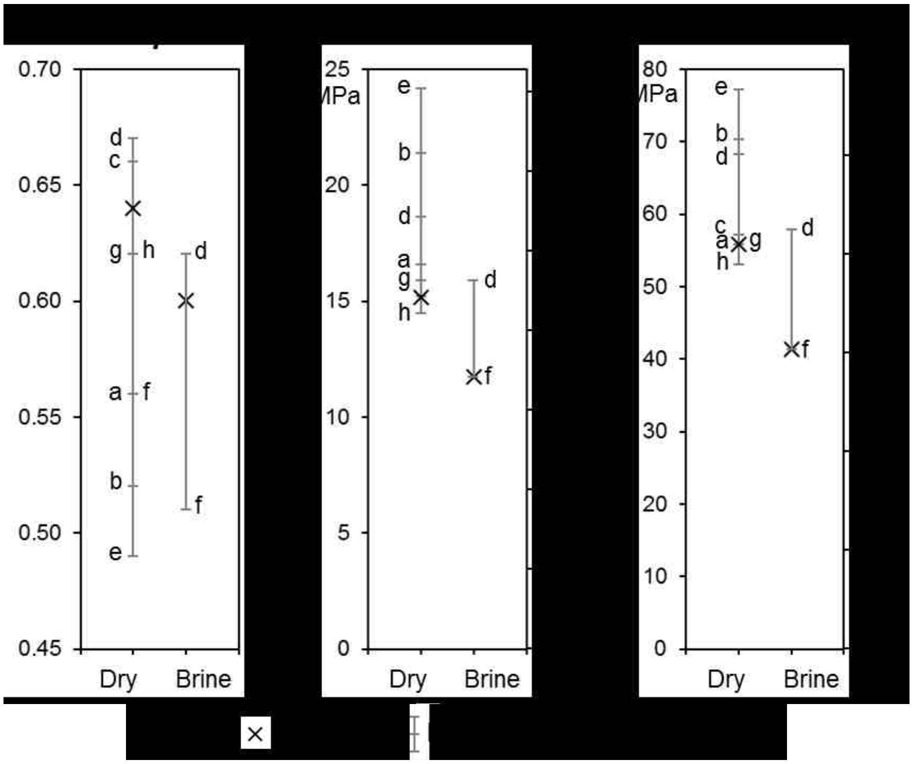

	Reference	Triaxial Test
a)	Gnirk and Cheatham (1963)	Conventional
b)	Handin and Hager (1963)	Conventional
c)	Wilhelmi and Somerton (1967)	Conventional
d)	Aldritch (1969)	Conventional
e)	Twiss and Moores (1992)	Conventional
f)	Baud et al. (2000)	Conventional
g)	Pagoulatos (2004)	Conventional
h)	Pagoulatos (2004)	Multistage

Fig. 28. μ, C, and UCS of dry, and brine saturated Berea sandstone.

Note that the values of μ and C inferred from the multistage triaxial test are in the upper and lower part of the respective bar of reference values. This ultimately places the inferred UCS in the lower part of its bar of reference values. Table 3 (Part II) presents the remaining μ, C, and UCS values for the remaining sandstones tested under the multistage triaxial test along with some additional literature values.

Sample	Fluid	Reference	Test	μ	*C*, kpsi	*UCS*, kpsi	*T*, kpsi
Bandera Sandstone	Dry	This work	Multistage Triaxial + Brazilian	0.44	2.0	6.1	0.6
		Handin and Hager (1957)	Conventional Triaxial	0.62	2.2	8.1	-
		Gnirk and Cheatham (1963)	Conventional Triaxial + Brazilian	0.44	2.0	6.1	0.4
	Brine	This work	Multistage Triaxial + Brazilian	0.35	1.4	4.0	0.4
	Dodecane	This work	Multistage Triaxial + Brazilian	0.42	1.8	5.5	0.5
Lyons Sandstone	Dry	This work	Multistage Triaxial + Brazilian	0.98	4.2	20.0	1.4
		Mighani (2014)	Conventional Uniaxial + Brazilian	-	-	14.0	1.1
		Yagiz (2009)	Conventional Uniaxial	-	-	17.4	-
		Kim and Ko (1979)	Conventional Triaxial	1.6	6.5	45.3	-
		Kim and Ko (1979)	Multiple Failure State (MFS) Triaxial	1.1	4.0	20.7	-
		TNCA (2015)	Rock Block Uniaxial (ASTM C170)	-	-	32.4	-
		TNCA (2015)	Shear pull-meter (ASTM C1028)	1.2	-	-	-
	Brine	This work	Multistage Triaxial + Brazilian	0.83	4.2	17.8	1.2
		TNCA (2015)	Shear pull-meter (ASTM C1028)	1.07	-	-	-
	Dodecane	This work	Multistage Triaxial + Brazilian	0.95	4.1	19.2	1.5
Tennessee Sandstone	Dry	This work	Multistage Triaxial + Brazilian	0.91	7.8	35.4	2.6
		Handin (1969)	Conventional Triaxial	0.84	7.3	31.3	-
		Mighani (2014)	Brazilian	-	-	-	1.9
	Brine	This work	Multistage Triaxial + Brazilian	0.84	7.1	30.5	2.0
	Dodecane	This work	Multistage Triaxial + Brazilian	0.90	7.4	33.2	2.4

Table 3 (Part II). μ, *C*, *UCS*, and *T* of Bandera, Lyons and Tennessee sandstones (dry, brine, and dodecane saturated).

Note: (1) Results from this work are highlighted: strain rate 5×10^{-6} s^{-1} (multistage triaxial test, Pagoulatos' (2004) method) and 0.27 kip/min (Brazilian tensile test).
(2) The literature values have been constrained to a linear failure envelope.

6.1.1 Pore Fluid Effects on Compressive Strength

The wet and dry μ, *C*, and *UCS* from the multistage triaxial tests are cross–plotted in Fig. 29. For comparison purposes, the brine and dodecane saturated values have been plotted on the same *y*-axis, and dry values on the *x*-axis.

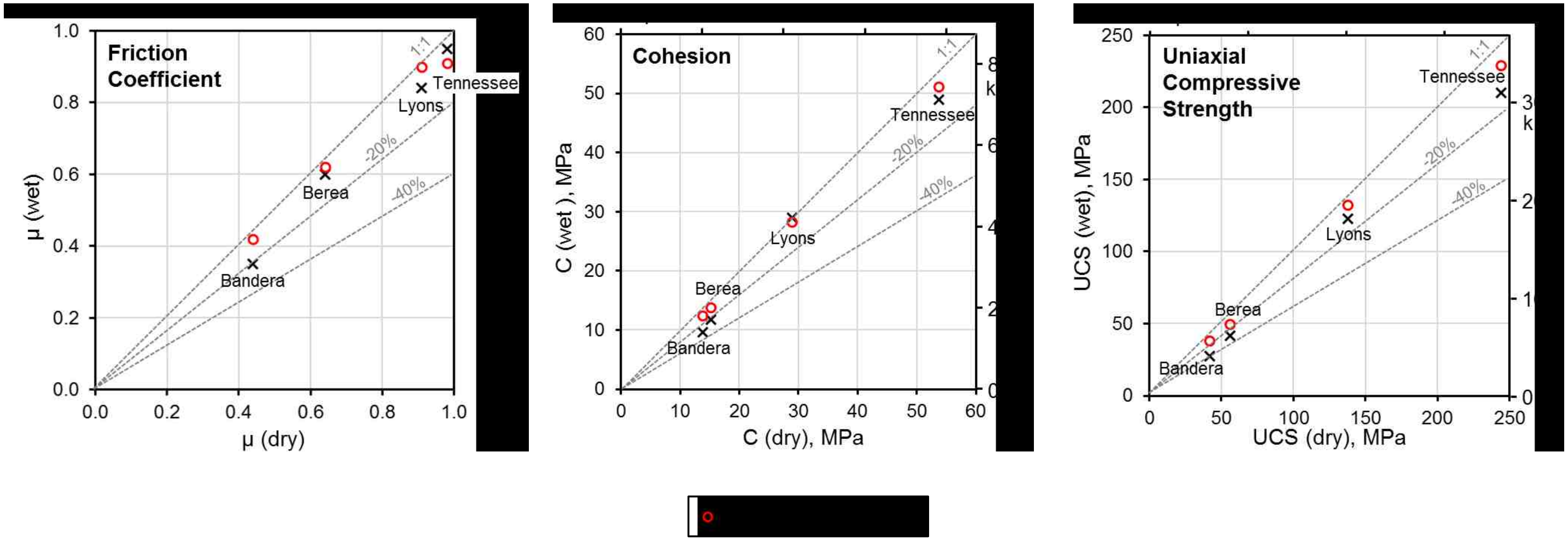

Fig. 29. μ, *C*, and *UCS* of the sandstones from multistage triaxial test (wet versus dry)

Note: *y*–axis corresponds to both brine and dodecane saturated samples.
μ, *C*, and *UCS* increase from Bandera, Berea, Lyons to Tennessee sandstone.
Both, brine and dodecane saturation reduce μ, *C*, and *UCS*.
The reduction is greater in brine saturated, and high porosity samples.
The *UCS* can be reduced up to 40%, i.e. brine saturated Bandera sandstone.

Griffith's theory (see Brittle Crack Propagation, Section 1.1.) can be referred to explain how the reduction of Young's modulus, *E*, and free surface energy, γ, in the presence of liquids reduce the critical strength for failure, σ_c. Van Voorhis et al. (1957) conducted a series of gravimetric adsorption experiments to calculate (see Gibbs adsorption equation for porous solids) the free surface energy of saturated silica, SiO_2, using synthetic porous plugs of compressed silica powder:

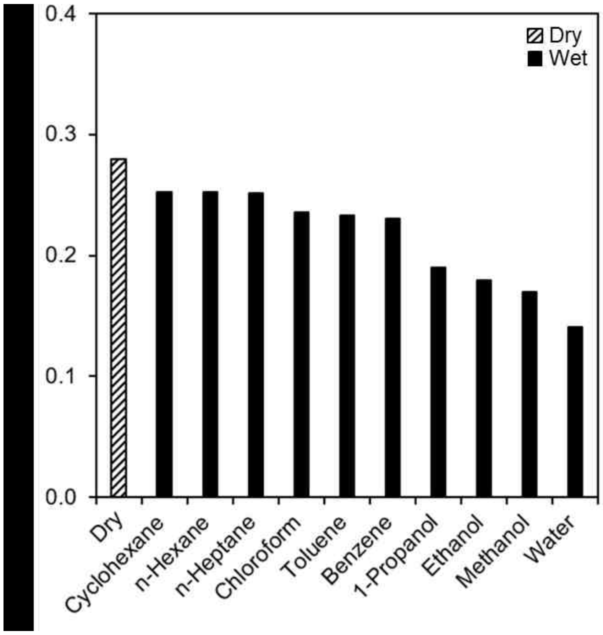

Fig. 30. Free surface energy of silica under dry and wet conditions.
Note: Dry value from Brunauer et al., 1956.
Wet values from Van Voorhis et al., 1957.
Water produces the greatest reduction of the free surface energy.

Paterson and Wong (1977) suggested that the hydration of polar SiO_2 molecules at the surface of silicate rocks causes stress corrosion (see Charles, 1959) in presence of H_2O. Fig. 31 suggests a strong linear relationship between molecular polarity and the wet and dry free surface energy of silica obtained by Van Voorhis et al. (1957).

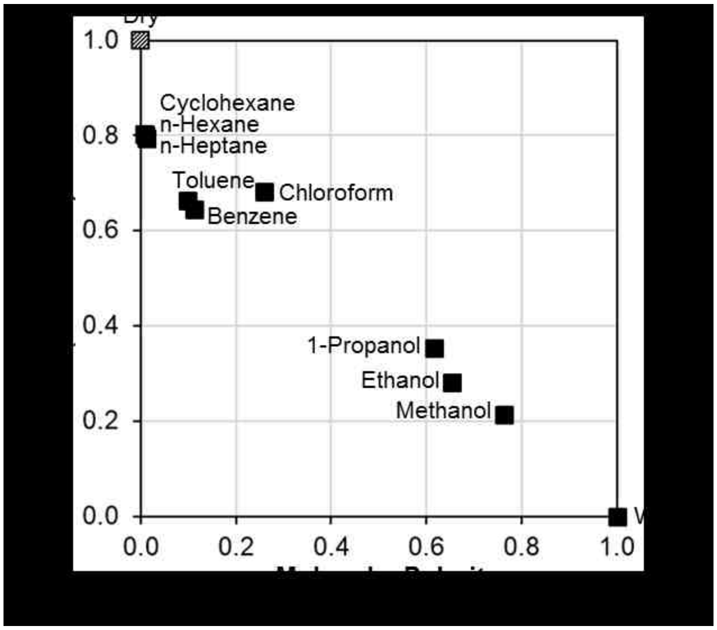

Fig. 31. Normalized free surface energy of wet and dry SiO_2 versus molecular polarity of the wetting fluids.

Note: *y*–axis: Free surface energy, experimental (Brunauer et al., 1956; Van Voorhis et al., 1957).
x–axis: Molecular polarity, theoretical (Reichardt, 2003).

Fig. 32 presents a schematic of the free surface energy changes associated to chemical adsorption processes. Extended periods of time and enhanced electrolyte concentrations increase the adsorbed mass of H_2O and further decrease the free surface energy.

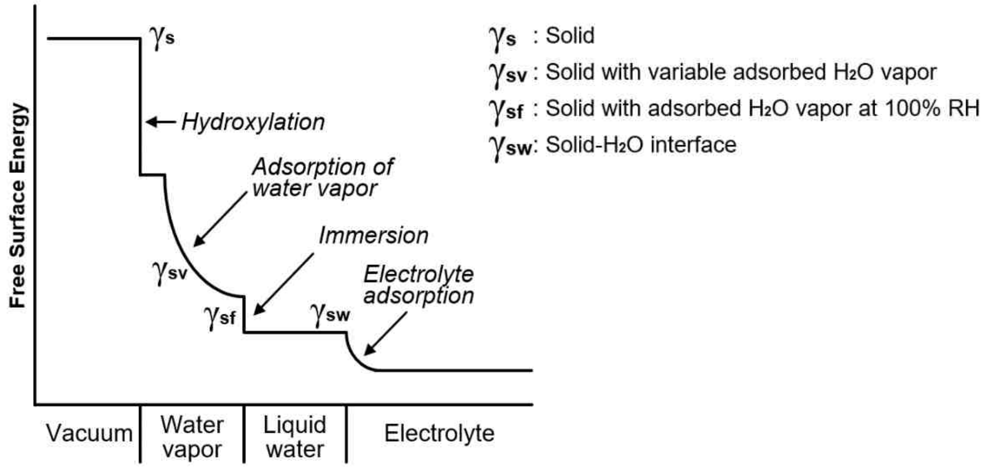

Fig. 32. Schematic of the effect of H_2O on the free surface energy
Note: After Parks (1984)

One question arises: why do non–polar molecules, such alkanes, somewhat reduce the free surface energy of polar surfaces such as silica? Non–polar molecules can certainty become induced–dipoles upon approach of either ions or strong dipoles, making adsorption possible, at least in theory. However, these induced–dipole forces are very weak and are unlikely to maintain a permanent monolayer over time. An alternative hypothesis is that the free surface energy reduction in the presence non–polar liquids has more to do with finite monolayers water vapor and residual liquid water suspended in those fluids. The relative humidity conditions of our experiments, and perhaps on the referenced free surface energy measurements, can indeed explain the observations.

The effect of finite small amounts of liquids on the mechanical behavior of rocks is not unknown. Tittmann et al. (1980) conducted a series of seismic attenuation measurements for shear elastic waves on wet Coconino sandstone (>95% quartz, 9% porosity) as a function of relative partial pressure (i.e. relative humidity) of benzene, hexane, methanol, ethanol, and water. The specific dissipation factor, Q^{-1}, was reported as the inverse of the seismic quality factor, Q:

$$Q^{-1} = \frac{2\pi W}{\Delta W} \tag{25}$$

Where W is the maximum value of elastic strain energy stored per cycle, and ΔW is the energy dissipated a cycle due attenuation mechanisms. Low Q^{-1} values are associated to weaker liquid–solid interaction, i.e. lower adsorption energies. The reader can refer to the literature (e.g. Cooper, 1979; Toksöz and Johnston, 1981) for details on seismic wave attenuation definitions and measurements.

The experiments reported by Tittmann et al. (1980) were carried out at about 10 kHz using the vibrating bar technique as described by Clark et al. (1980). Their findings suggest that low at low relative partial pressure ($P/P_o < 0.1$) polar liquids can have a dramatic effect on seismic attenuation. Non–polar liquids require much higher relative partial pressures ($P/P_o > 0.7$) to show any effect on seismic attenuation (Fig. 33a). The same information can be presented by plotting Q^{-1} versus the relative mass adsorbed (i.e. x with respect to the necessary adsorbate mass, x_m, to form a monolayer), Fig 33b:

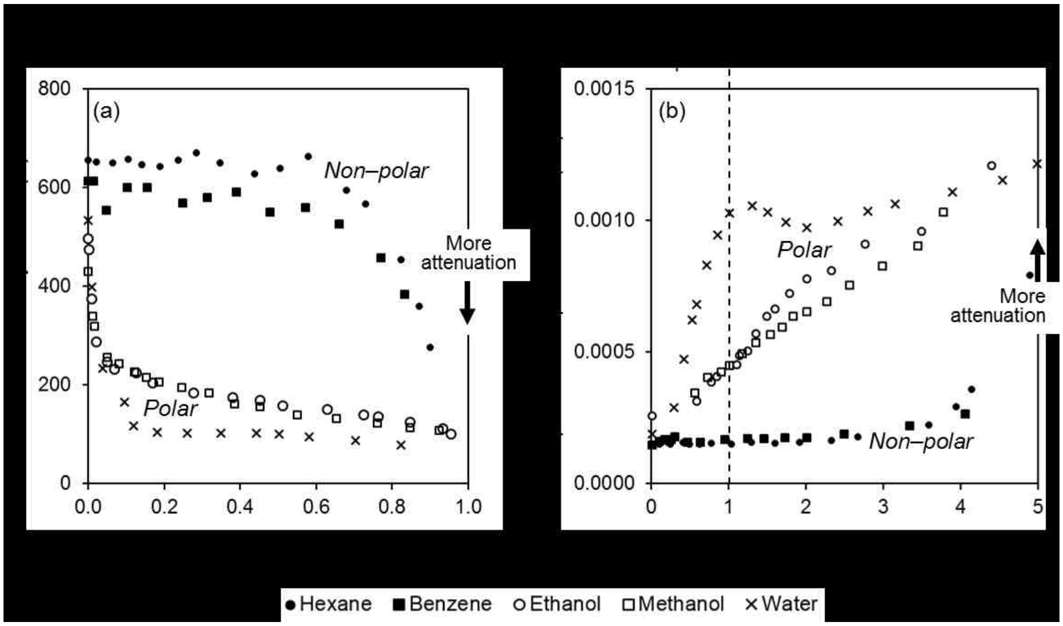

Fig. 33. Effect of humidity and mass adsorption on seismic attenuation (10 kHz).
Rock: Coconino sandstone (>95% quartz, 9% porosity)

(a) Seismic Quality Factor versus Relative Partial Pressure, note that:
$P/Po < 0.1$: Hydrocarbons have little effect on Q, alcohols intermediate, and water high
$P/Po > 0.7$: Hydrocarbons begin to reduce Q.

(b) Specific Dissipation Factor versus Relative Adsorbed Mass, note that:
The x/x_m values are scaled to the surface area determined for water
$x/x_m < 1$: Monolayer adsorption ("Regime I")
$x/x_m > 1$: Fluid condensation in capillaries, contributing to fluid flow ("Regime II")
There is an approximately linear dependence of Q^{-1} and x/x_m on Regime I.
After (Tittmann et al. 1978)

Note that there is an approximately linear dependence of Q^{-1} and x/x_m below x/x_m < 1.0 (i.e. Regime I: monolayer adsorption, or $x < x_m$). The slope of this behavior (ΔQ^{-1} per unit of $\Delta x/x_m$) was suggested to be related to the polarity of the adsorbate, Fig. 34:

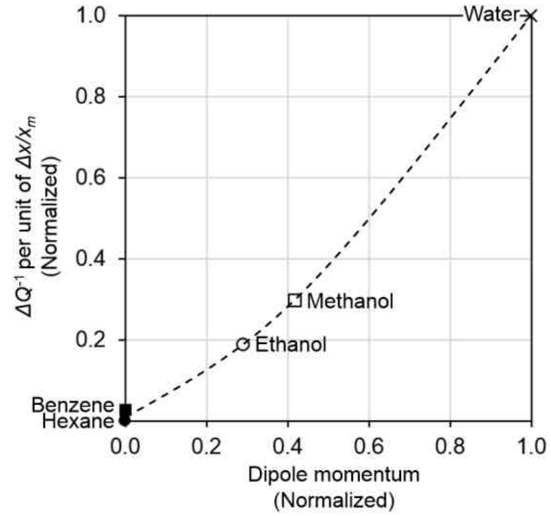

Fig. 34. Monolayer adsorption slope (ΔQ^{-1} per unit of $\Delta x/x_m$) versus dipole momentum.
Rock: Coconino sandstone (>95% quartz, 9% porosity)
Note: Slope taken as it appears on Fig. 35. during Regime I ($x/x_m < 1$)
Both variables have been normalized with respect to the case of water
After (Tittmann et al. 1978)

Colback and Wiid (1965) studied the effect of finite water saturation under variable relative humidity on rock strength carrying out as series of *UCS* measurements on a quarzitic sandstone (Ecca Series of the Karroo Basin, South Africa; 15% porosity). The relative humidity was controlled by placing the samples in a globe box in the presence of various saturated solutions. Their findings suggest that even small change of 0.7 wt% in moisture content (i.e. 10.5% in water saturation) can reduce the *UCS* by 40% (Fig. 35). Additional triaxial measurements on the Karoo Basin sandstone and on a quarzitic shale (<1% porosity, Jeppestown shale from the Witwatersrand Basin – South Africa) also suggest that water reduces both C and μ in the sandstone but only C in the shale (Fig. 36). A selected literature review on the effect of water on the mechanical properties of rocks, is presented in Table 4.

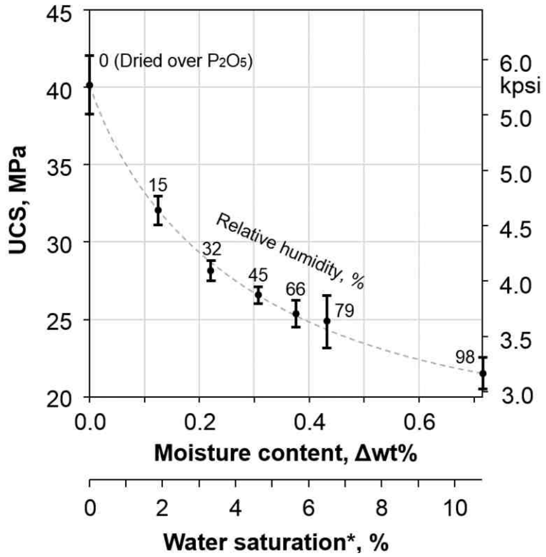

Fig. 35. *UCS* versus moisture content, and water saturation.

Note: Quarzitic sandstone (Ecca Series of the Karroo Basin, South Africa)
Change in water saturation calculated assuming a grain density of 2.65 g/cm^3 (quartz), 15% porosity, and establishing 0.0% relative humidity as zero datum.
After Colback and Wiid (1965)

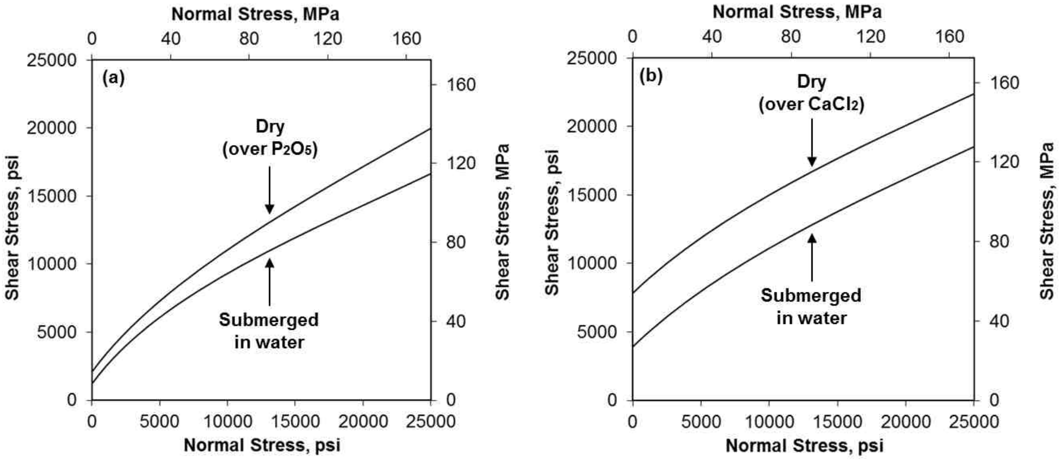

Fig. 36. Wet and dry non–linear failure envelopes from drained conventional triaxial tests

Note: (a) Karoo Basin quarzitic sandstone
(b) Jeppestown shale
After Colback and Wiid (1965)

Reference	Test	Rock	Fluid	Findings
Ojo and Brook (1989)	Triaxial Compression Uniaxial Tension Point Load Hardness	2 sandstones	Water	- Moisture content reduces rock strength and hardness. - Oven drying leads to anomalously high values of strength, atypical of *in-situ* conditions. - The effect of pH on rock strength is encouraged to be studied.
Hawkins and McConnell (1992)	Uniaxial Compression	35 sandstones	Water	- The reduction of the rock strength is controlled primarily by minerology and to a lesser extent by microstructure. - The strength reduction increases from quartz arenites, sublitharenite, lithic wacke, to quartz wacke.
Masuda (2000)	Triaxial Compression (Sensitivity to strain rate)	Granite Andesite	Water	- Water leads to a greater strain rate sensitivity of the compressive strength, which is greater at high confinement. - The effect of temperature on rock strength is encouraged to be studied.
Vásárhelyi and Van (2006)	Uniaxial Compression (Dry and Wet)	15 sandstones (Compilation)	Water (Sensitivity to saturation)	- The strength is “highly” dependent on the effective porosity. - The sensitivity to the Young’s modulus, and tensile strength is “likely” to be similar to that of the UCS.
Demarco et al. (2007)	Uniaxial Compression (Dry and Wet)	8 quarzitic sandstones	Water (Sensitivity to saturation)	- There is not simple relationship between porosity and strength reduction, the samples with medium porosity were most affected. - The smaller pores ($<0.1\ \mu$) are suspected to have in hygric expansion (i.e. disjoining pressures within small pores). - The hygric expansion suspected to be the underlying reason of the strength reduction, due to swelling clay minerals.
Mammen et al. (2009)	‘Cuttability’ performance	Quarzitic sandstone (Argillaceous)	Water	- Moisture content reduces the rock cutting and normal forces by 40% and 49%, Specific Energy for Impact wear by 80%, and compressive strength by 68%.
Ojala (2011)	Tensile Strength	2 sandstones 2 chalks 1 shale	CO_2–Water	- The strength reduction did not appear to be affected by the CO_2 environment - Water had a weakening effect in all the tested lithologies.
Wong et al. (2016)	Uniaxial Compression Tensile Strength Elastic Moduli	Sedimentary Igneous Metamorphic (Compilation)	Water (and others)	- Sedimentary rocks are more affected than igneous and metamorphic. - Water content is the most significant, but not the only weakening factor. Porosity, density, fabric, and test conditions are to be taken into account.

Table 4. Effect of liquids on the mechanical properties of rocks (selected literature review).

6.1.2 Pore Fluid Effects on Tensile Strength

The Brazilian test is a commonly used experiment to determine the tensile strength of rock. Carneiro (1943) based his method in Hertz (1895) point load theory to calculate the minimum stress in the center of a circular disk under diametrical compression, Fig. 37:

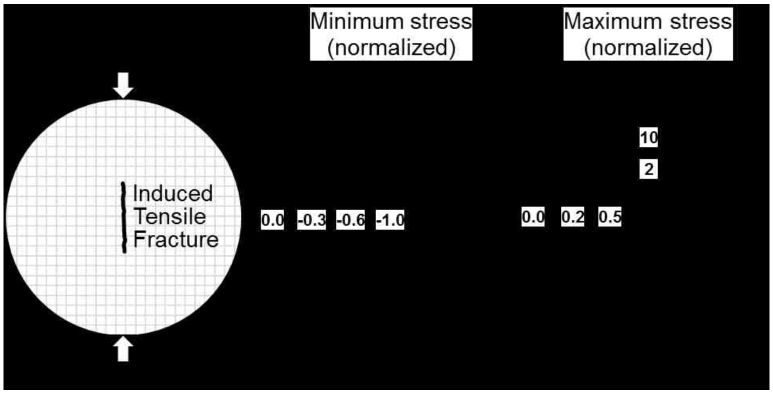

Fig. 37. Brazilian tensile test schematics.

Note: Left: Induced tensile fracture on the center the disk under diametrical compression.
Center: Normalized* minimum stress field.
Right: Normalized* maximum stress field.
*To the minimum and maximum stresses in the center of the disk.

This technique was inspired in observations of vertical tensile fractures being opened on cylindrical concrete rollers in between compression plates. The circumstances of these observations are not just curious, but worth mentioning: such rollers were being used to move a church in Rio de Janeiro in order to avoid its demolition. Concrete was used because the steel usage was directed to war efforts (Fairbairn and Ulm, 2002). Frocht (1948) developed 2D analytical solutions for the principal stresses, σ_1 and σ_3, in a Cartesian coordinate system, x–y, in terms of the applied point load, the radius, R, and thickness, t, of the disk. The tensile strength, T, is inferred from the minimum stress at the center of the disk at failure:

$$\mathrm{T} = \frac{-\mathrm{P}}{\pi \mathrm{R} \mathrm{t}} \tag{26}$$

This study uses a constant loading rate of 20 N/s (270 lbf/min) as recommended by the ISRM (1978) for the Brazilian test. All samples were loaded perpendicularly to their bedding planes (see Mighani, 2014 for the effect of bedding planes). Failure was detected via strain and sudden increase in the recorded AE count, Fig. 38:

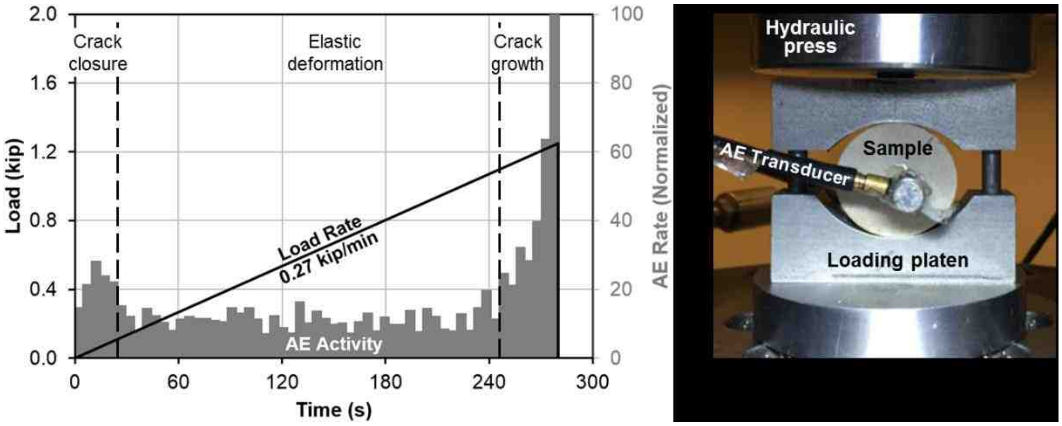

Fig. 38. Brazilian test in dry Berea sandstone
Note: Left: AE activity response under constant loading rate
Right: Configuration of the test
The AE transducer is attached to one of the flat sides of the disk

Fig. 39 presents cross plots of wet versus dry tensile strength, *T*, for all tested samples, note that there is a reduction of strength upon liquid saturation. *T* is significantly reduced in high porosity sandstones upon the presence of H_2O, being up to 45% lower (i.e. brine saturated Berea sandstone). Fig. 40 shows the *UCS* inferred from the multistage triaxial test versus *T* from the Brazilian tensile test. Note that *T* is about 6% or 7% of the *UCS*, regardless of the saturating fluid. This suggest that different fluids cause similar reductions to the compressive and tensile strength. Also, that the typical rule of thumb of assuming that *T* it is 10% of the *UCS* might result in a slight overestimation, at least based on this dataset.

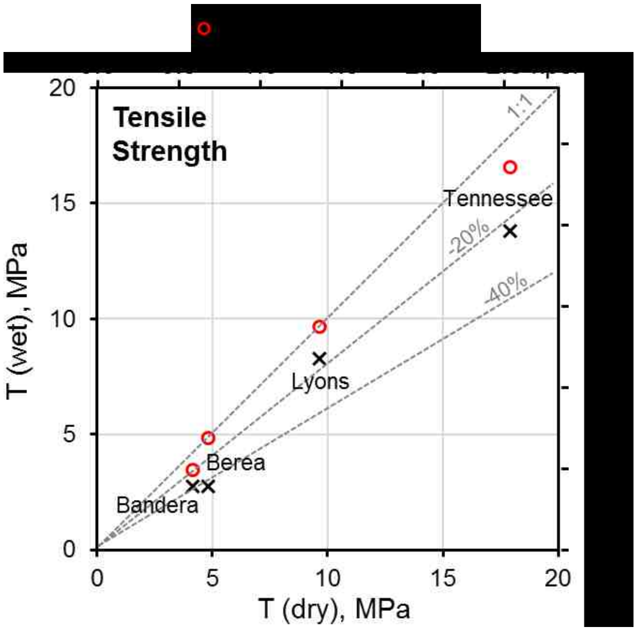

Fig. 39. *T* (wet versus dry) inferred from Brazilian tensile testing.

Note: *y*–axis corresponds to both brine and dodecane saturated samples.
T increases from Bandera, Berea, Lyons to Tennessee sandstone.
Both, brine and decane reduce *T*.
The reduction is greater in brine saturated, and high porosity samples.
T can be reduced up to 45%, i.e. brine saturated Berea sandstone.

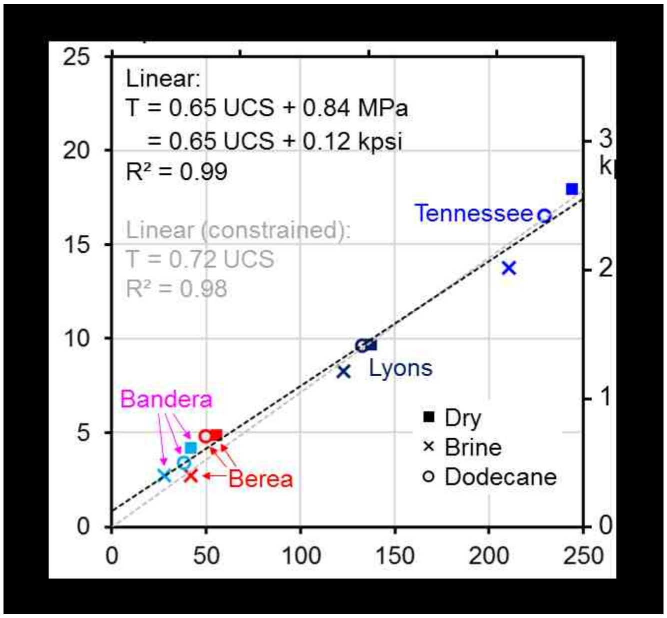

Fig. 40. *T* versus *UCS* for the tested sandstones.

Note: Constrained and unconstrained linear trends are set to fit the data.
T increases from Bandera, Berea, Lyons to Tennessee sandstone.
All the data points are roughly in the same trends.
Brine and dodecane have a similar weakening effect on *T* and *UCS*.
In this case, the rule of thumb, *T* it is 10% of the *UCS*, overestimates *T*.

6.1.3 Pore Fluid Effects on Elastic Moduli

Fig. 41 presents the static and dynamic Young's modulus dependence on confining pressure for the sandstones tested under drained wet and dry conditions.

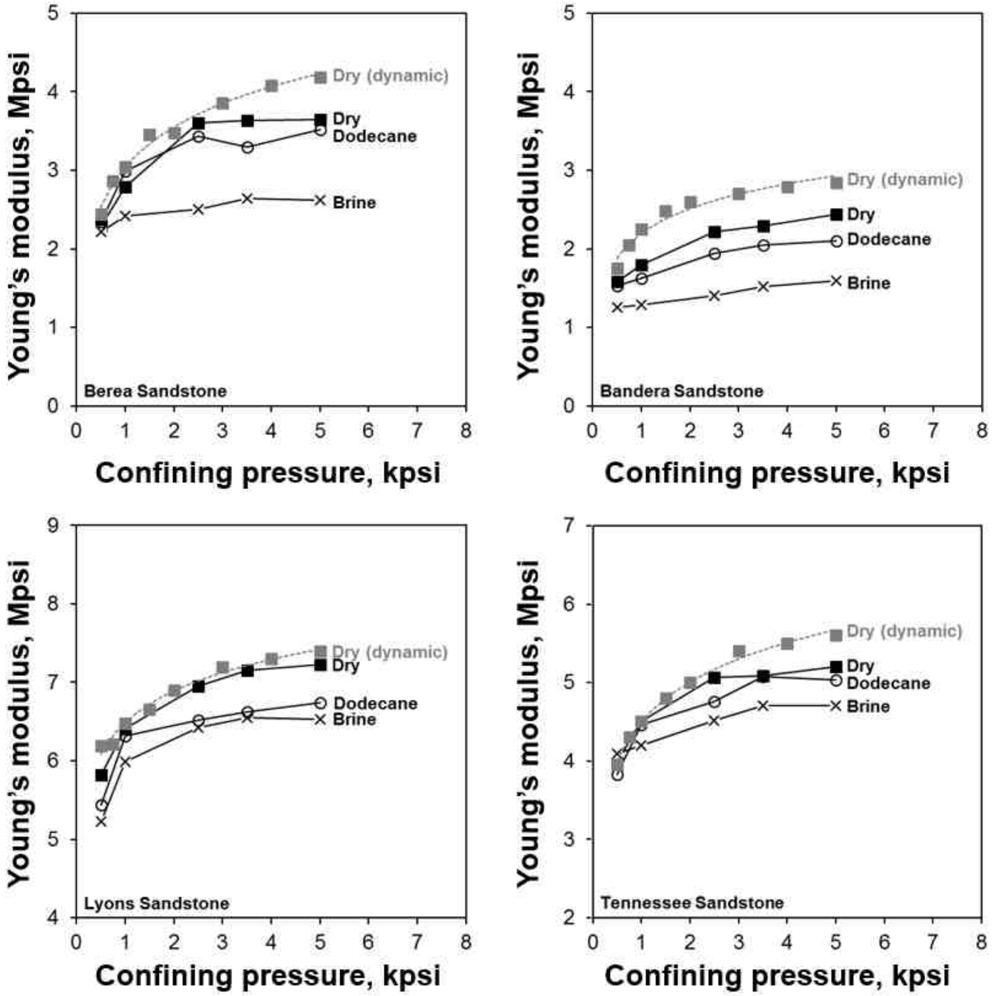

Fig. 41. Static and dynamic Young's modulus for sandstones at several confining pressures.
Note: (1) The dynamic modulus is an upper bound on all the drained static measurements.
(2) Both brine and dodecane reduce the stiffness of the sandstones.
(3) The reduction is greater in brine saturated and Bandera and Berea (higher porosity) samples.
(4) The reduction is greater at high confining pressure.

These dynamic observations are similar to the results referenced by Spencer (1981) from low frequency (i.e. 7–2100 Hz) measurements in dry, distilled water, ethanol, and n–decane saturated Navajo sandstone. There is a good correlation between the reduction of the free surface energy of wet silica, as proxy of the Navajo sandstone, and the observed saturated dynamic Young's modulus, Fig. 42:

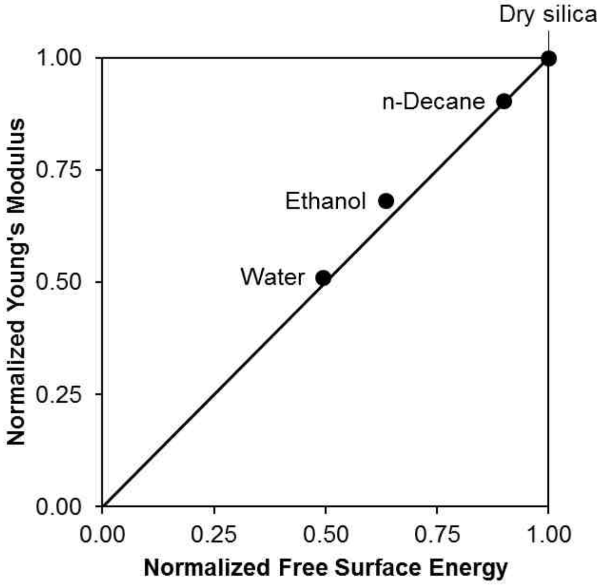

Fig. 42. Effect of immersing SiO_2 in liquids on its free surface energy of silica and dynamic Young's modulus. After Spencer (1981).

Fig. 43 presents the static and dynamic Poisson's ratio dependence on confining pressure for the tested sandstones. In general, the dry Poisson's ratio is lower, especially at low confining pressure. To explain this, one might refer to Eq. 23 by replacing the V_p and V_s ratio in terms of bulk and shear modulus, *K* and *G* (Eq. 27). Increasing the confining pressure increases *K* and *G* due to crack closure (see O'Connell and Budiansky, 1974). In dry rocks, *K* increases faster than *G* with confining pressure due to the high compressibility of the air filling their pores, ultimately resulting in an increment of *v*. In contrast, less compressible brine and dodecane make *K* less sensitive to confining pressure; then, *G* increases faster than *K*, resulting in a decrement of *v* as the confining pressure increases.

$$v = \frac{1}{2}\frac{\left(\frac{K}{G}+\frac{4}{3}\right)-2}{\left(\frac{K}{G}+\frac{4}{3}\right)-1} \qquad (27)$$

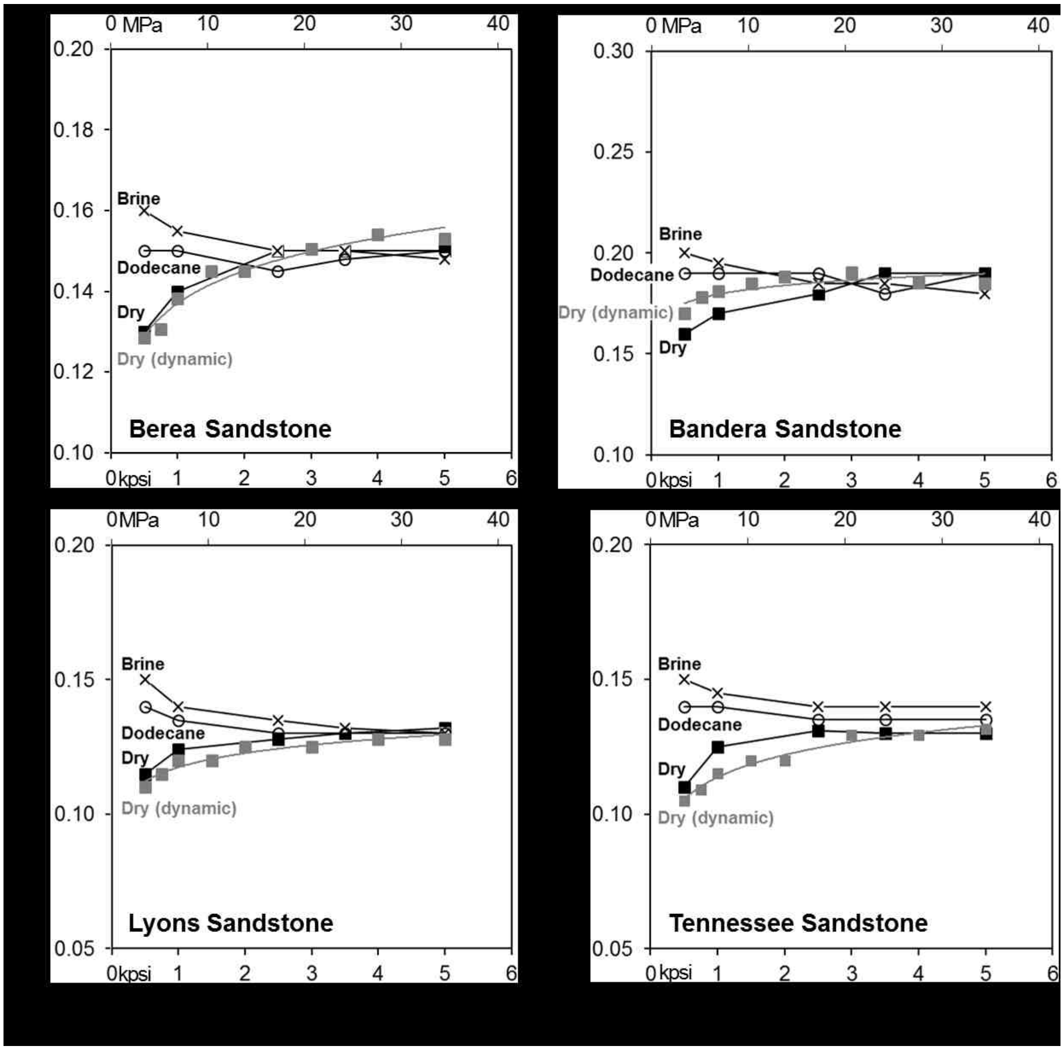

Fig. 43. Static and dynamic Poisson's ratio of the tested sandstones at several confining pressures.

Note: (1) Both brine and dodecane increase the Poisson's ratio of the sandstones.

(2) The increment is more significant at low confining pressure.

6.2 Shales

Table 5 summarizes the results from the triaxial testing on Eagle Ford and Woodford shales samples.

Shale	Depth (ft)	Test	Vein	μ	C, kpsi	UCS, kpsi
Eagle Ford	11094.89	Multi–stage	—	0.52	7.5	24.6
	11115.35	Multi–stage	—	0.60	7.0	24.7
	11204.47	Multi–stage	—	0.60	7.8	27.4
	11216.15	Multi–stage	—	0.69	6.5	24.9
Woodford	9654.29	Multi–stage	—	0.59	4.0	14.2
	9630.94	Single–stage	Calcite filled	0.63	*	—
	9731.26	Single–stage	Clay filled	1.16	*	—
	9784.58	Single–stage	Calcite filled	0.96	*	—

Table 5. μ, C, UCS of the Eagle Ford and Woodford shale samples.
Note: (1) All strain rates equal to 5×10^{-6} s^{-1}.
(2) Veined samples failed under a confining pressure of 500 psi.
*The cohesion of the veins, C', is assumed to be zero (See section 6.2.1)

6.2.1 Shear Reactivation of Preexisting Veins

Sudden shear reactivation of preexisting veins led to the catastrophic failure of the three veined of Woodford shale samples at 500 psi confining pressure, Fig. 44. It resulted impossible to detect the onset of crack growth using the volumetric strain or the AE count, making it impractical to render a multistage triaxial test. However, we assessed the friction coefficient of the veins (Fig. 45) by assuming that their cohesion is negligible relative to the cohesion of the matrix. Our results (i.e. $0.63 \leq \mu \leq 1.16$) are comparable to Byerlee's (1978) friction law (i.e. $\mu = 0.85$ if $\sigma_n < 200$ MPa), but always greater than the value reported by Jaeger (1971) (i.e. $\mu = 0.60$).

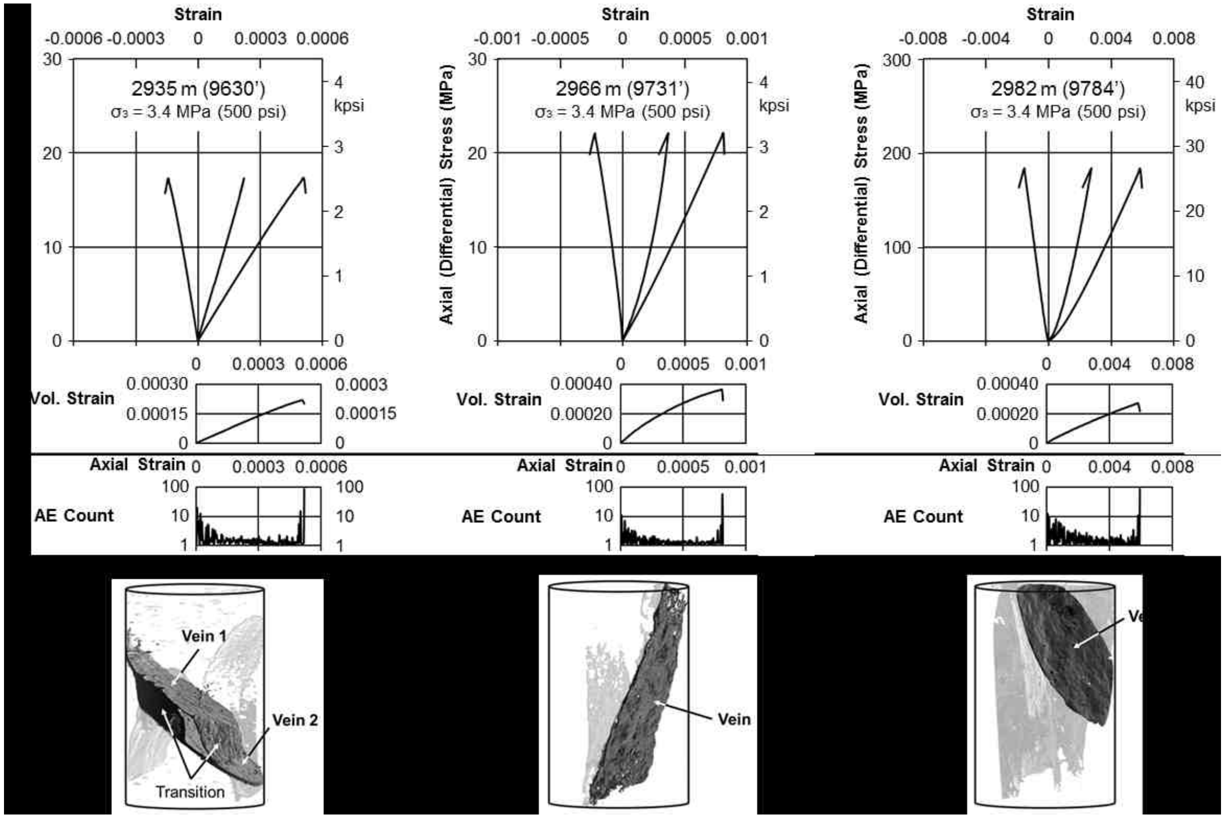

Fig. 44. Shear reactivation on three of the Woodford shale samples.

(1st, from top) Axial stress (differential) versus lateral, volumetric, and axial strain, (2nd) Volumetric strain versus axial strain (3rd) AE count versus axial strain, (4th) Post–failure µ–CT images:

- Darker shade: Shear reactivation of veins, resulting in very flat planes.
- Lighter shade: Shear failure of the intact rock matrix, thought to have occurred after the shear reactivation of veins.

Note: Rock failure occurred with no volumetric dilatancy and little to non-precursory AE activity.

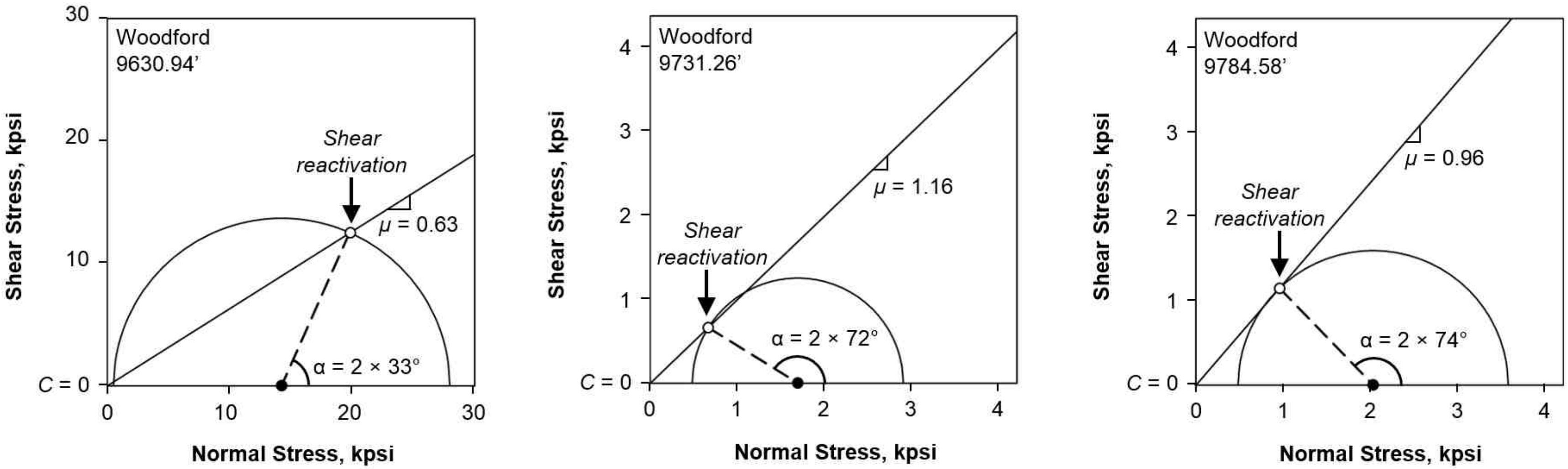

Fig. 45. Sliding envelopes of the three veined Woodford shale samples.

Note: (1) The sliding envelope defines the friction coefficient for the movement along the veins.
(2) The cohesion of the veins is assumed to be negligible relative to the cohesion of the matrix.
(3) τ_s and σ_n were calculated with σ_1 and σ_3 at failure, using the orientation of the veins from the direction of σ_3.
(4) The obtained μ values are comparable to Byerlee’s (1978) friction law (i.e. $\mu = 0.85$ if $\sigma_n < 200$ MPa), but always greater than the value reported by Jaeger (1971) (i.e. $\mu = 0.60$).

Veins, and weakness planes in general, can reduce the brittle strength of rocks depending upon their intrinsic strength, and, foremost, their orientation with respect to the applied stresses. Strength reductions of up to 95% have been reported in triaxial compression (e.g. Donath, 1966; McLamore and Gray, 1967; Fjær and Nes, 2013; and Jaeger and Cook, 1979) and indirect tension (e.g. Chen et al. 1998; Tavallali and Vervoort, 2013; Mighani, 2014).

6.2.2 Explicit Dependence of the Failure Envelope Parameters

A linear failure envelope from a multistage triaxial test must reproduce the observed σ_1 at failure, under the assumption that strength loss is negligible. To this end, substituting Eq. 4 and 5 into Eq. 6 yields a constrained mathematical relationship between C and μ:

$$C = \left(\frac{1}{\sqrt{\mu^2+1}} - \mu\right)\left(\frac{\sigma_1+\sigma_3}{2}\right) + \left(\frac{\mu^2}{\sqrt{\mu^2+1}}\right)\left(\frac{\sigma_1-\sigma_3}{2}\right) \qquad (28)$$

Eq. 28 describes all possible failure envelopes that are tangent to a given a Mohr's circle at failure. Hence, the dependence of the inferred failure envelope parameters can be presented in the C–μ space. For example, Fig. 46 for the Eagle Ford and Woodford shales tested under the multistage triaxial test.

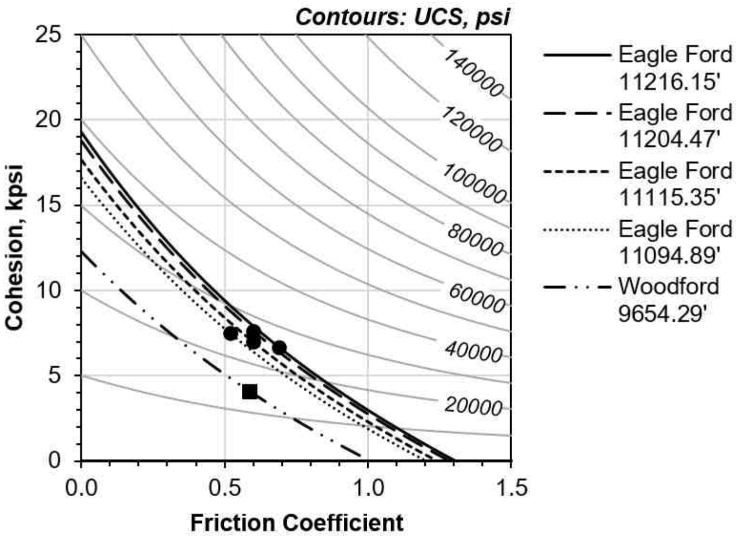

Fig. 46. *C*, μ and *UCS* dependence for the tested Eagle Ford and Woodford shales.
Note: Solid data markers are estimated values from the multistage triaxial test.
Dashed lines define the constrained relationship between *C* and μ (Eq. 28)
Solid contours give *UCS* as a function of the *C* and μ (Eq. 10)
Example: Assuming that $\mu = 0.85$ (i.e. Byerlee's law) would imply $C \approx 1.5$ kpsi and $UCS \approx 0.5$ kpsi (Woodford) and $C \approx 4.0$ and $UCS \approx 18$ kpsi (Eagle Ford).

6.2.3 Acoustic Emissions in Shales

Rock cement rupture and grain fracture are energy releasing processes that transform part of the stored elastic strain energy to radiation of elastic waves, i.e. Acoustic Emission (AE) events. We counted the AE events in each of the multistage triaxial tests in sandstones and shales (see Appendix II) and attempted to identify of the crack growth onset, which was previously identified using the termination criterion based on the deflection of the volumetric strain (Crawford and Wylie, 1987; Pagoulatos, 2004). Fig. 47 presents the AE count per incremental unit of axial strain for the last stage of each multistage experiment. We observe that in sandstones the crack growth onset is detectable by using both the volumetric strain curve and the AE count, regardless of the saturation fluid. That is not the case in shales, where the AE count is delayed, occurring just before the catastrophic failure. These findings might suggest that, in shales:

(1) These AE events might occur but remain undetected. The grain size of the shales is much smaller; therefore, their deformation and displacement results in smaller amplitude and higher frequency events, which in turn, have lower energy and attenuate quickly. Some examples of this have been presented by Eberhardt et al. (1999) on granites and by Mighani (2014) on Lyons sandstone and pyrophyllite.

(2) These AE events are rare. The more ductile characteristics of shales make plasticity the preferred deformation mechanism. Plastic deformation results in a continuous release of strain energy rather than the sudden release associated with discrete AE events. This has been widely studied in metallic materials were plastic deformation result on continuous basal dislocation-type AE events (Horváth et al., 2015; Kocich et al., 2012; Dobroň, 2016).

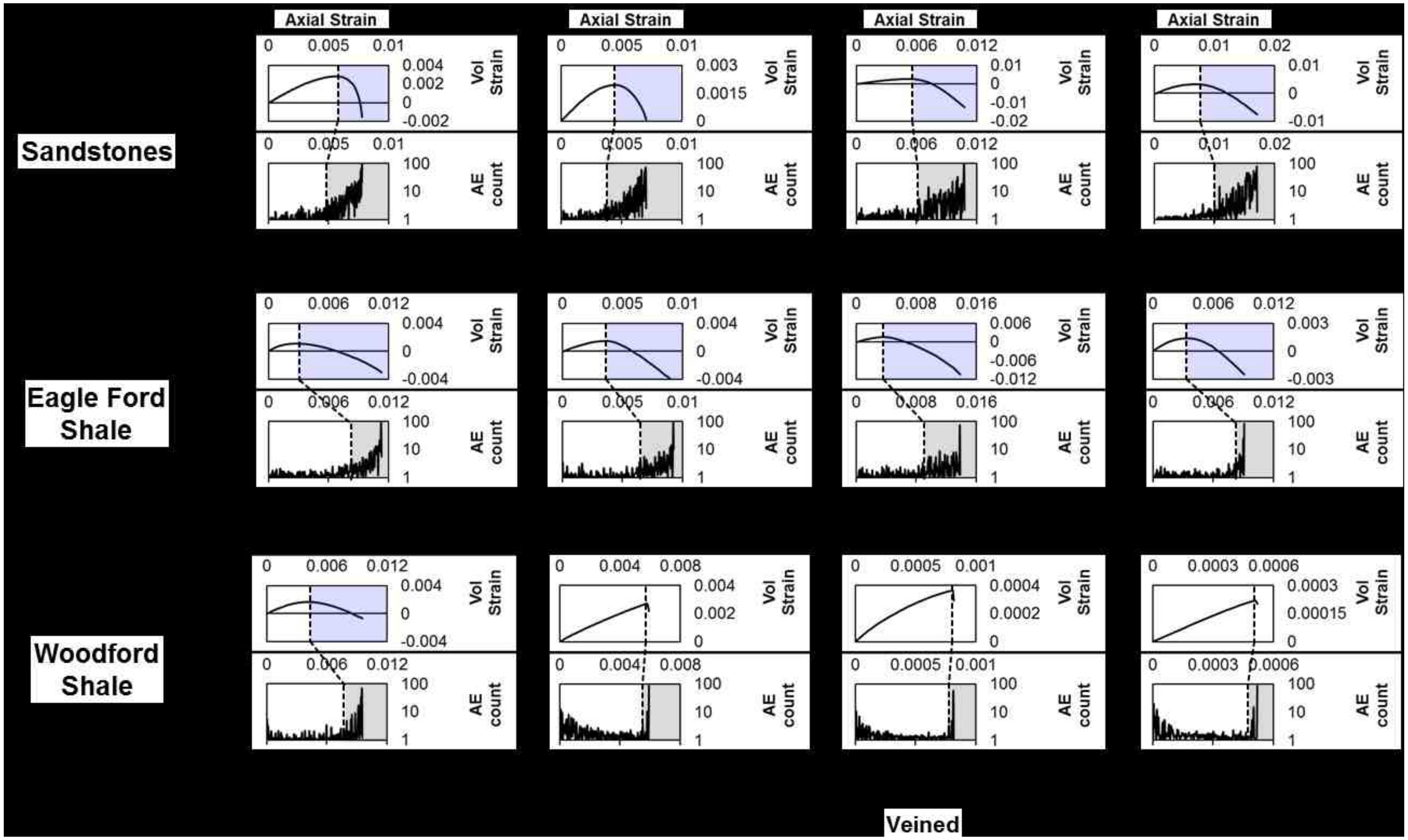

Fig. 47. Volumetric strain and the AE count per incremental unit of axial strain for the final testing stage on dry sandstones and shales.

Note: The shaded areas start at a crack growth onset defined with the maximum volumetric strain (dilatancy) and the AE activity onset.

- In sandstones: The AE activity onset occurred near the maximum volumetric strain, being slightly delayed on the tighter samples.
- In intact shales: The AE activity onset was significantly delayed with respect to the maximum volumetric strain.
- In veined shales: Rock failure occurred with no volumetric dilatancy and little to non-precursory AE activity.

Chapter 7: Summary and Conclusions

7.1 Sandstones

The multistage triaxial test (Pagoulatos, 2004) has proven to be a reliable alternative to determine a failure envelope using a single sample, when sample heterogeneity or availability limit the possibility of defining a failure envelope from a multitude of triaxial tests. A set of equations for the linear failure envelopes of Berea, Bandera, Lyons and Tennessee sandstones under dry, brine saturated and dodecane saturated conditions is presented in Table 6:

Formation	Fluid	Failure Envelope (kpsi)	%Error (*C*)	%Error (*UCS*)
Berea Sandstone	Dry	$\tau_s = 0.64\ \sigma_n + 2.2$	9.1	8.6
	Brine	$\tau_s = 0.60\ \sigma_n + 1.7$	11.8	10.0
	Dodecane	$\tau_s = 0.62\ \sigma_n + 2.0$	10.0	8.3
Bandera Sandstone	Dry	$\tau_s = 0.44\ \sigma_n + 2.0$	5.0	4.9
	Brine	$\tau_s = 0.35\ \sigma_n + 1.4$	14.3	15.0
	Dodecane	$\tau_s = 0.42\ \sigma_n + 1.8$	5.6	12.7
Lyons Sandstone	Dry	$\tau_s = 0.98\ \sigma_n + 4.2$	7.1	9.5
	Brine	$\tau_s = 0.83\ \sigma_n + 4.2$	2.4	3.9
	Dodecane	$\tau_s = 0.95\ \sigma_n + 4.1$	4.9	4.7
Tennessee Sandstone	Dry	$\tau_s = 0.91\ \sigma_n + 7.8$	5.1	1.1
	Brine	$\tau_s = 0.84\ \sigma_n + 7.1$	2.8	2.3
	Dodecane	$\tau_s = 0.90\ \sigma_n + 7.4$	2.7	1.5

Table 6. Failure envelope equations for the tested sandstones.

Note: Drained conditions, loading at a constant axial strain rate of $5 \times 10^{-6}\ s^{-1}$
Testing stages at confining pressures of 500, 1000, 2500, 3500, and 5000 psi.
The error of *C* is the maximum misfit between the fitted linear failure envelope and the Mohr's circles. The error of the *UCS* is calculated using the error of *C* (Eq. 10).

This investigation has demonstrated that rock strength can be reduced in the presence of liquids in accordance to previous studies (Table 4). Higher porosity sandstones (Berea and Bandera) had a greater reduction in strength upon liquid saturation. We observed that the compressive and tensile strength of sandstones could be reduced by up to 40% and 45% in the presence of brine, respectively and almost equally.

The weakening effect of liquids in sandstones is thought to be related to the reduction of the free surface energy and elastic moduli of SiO_2 in the presence of H_2O (see Van Voorhis et al., 1957; Colback and Wiid, 1965; Paterson and Wong, 1977; Spencer, 1981; and Parks, 1984). Non–polar liquids, such dodecane, are also reported to have similar but minor effect on free surface energy (Van Voorhis et al. 1957) and elastic moduli (Spencer, 1981). Although the attraction forces between polar surfaces and non–polar molecules are not sufficient to explain the free surface energy reduction associated with adsorption phenomena, we suspect that it has more to do with finite monolayers of water vapor under atmospheric conditions, or with residual water molecules present in those non–polar fluids (Tittmann et al., 1980). We recognize that the relative humidity conditions of our experiments, and perhaps in the referenced literature references, can indeed explain the observations.

7.1 Shales

This investigation also assessed the failure envelope of a suite of Eagle Ford and Woodford shale samples using a multistage triaxial test (Table 7). The multistage triaxial method was impractical for veined shales as the crack growth onset could not be detected via volumetric strain or AE activity. However, we assessed the friction coefficient of the veins of three Woodford shale samples if their cohesion is assumed to be negligible relative to the cohesion of the matrix. Our results found the following range of friction coefficient for the movement along the veins: $0.63 \leq \mu \leq 1.16$. Which is are comparable to Byerlee's (1978) friction law values, $\mu = 0.85$ if $\sigma_n < 200$ MPa, but always greater than the value reported by Jaeger (1971), $\mu = 0.60$.

Formation	Depth	Failure Envelope (kpsi)	%Error (*C*)	%Error (*UCS*)
Woodford Shale	9630.94’ (*)	$\tau_s = 0.63\ \sigma_n$	—	—
	9731.26’ (*)	$\tau_s = 1.16\ \sigma_n$	—	—
	9784.58’ (*)	$\tau_s = 0.96\ \sigma_n$	—	—
	9654.29’	$\tau_s = 0.59\ \sigma_n + 4.0$	9.9	9.2
Eagle Ford Shale	11094.89’	$\tau_s = 0.52\ \sigma_n + 7.5$	2.7	2.4
	11115.35’	$\tau_s = 0.60\ \sigma_n + 7.0$	8.6	8.1
	11204.47’	$\tau_s = 0.60\ \sigma_n + 7.8$	2.6	3.3
	11216.15’	$\tau_s = 0.69\ \sigma_n + 6.5$	3.1	3.2

Table 7. Failure envelope equations for the tested shales (intact samples).

Note: * Veined samples: Tested with a conventional single–stage test at 500 psi.
All test at drained conditions, loading at a constant axial strain rate of 5×10^{-6} s^{-1}
Testing stages at confining pressures of 500, 1000, 2500, 3500, and 5000 psi.
The error of *C* is the maximum misfit between the fitted linear failure envelope and the Mohr’s circles. The error of the *UCS* is calculated using the error of *C* (Eq. 10).

A good correlation between the AE activity onset and the deflection point of the volumetric strain curve was observed in the tested sandstones, regardless the saturating fluid. Unfortunately, this was not the case for the shales tested since the onset of AE activity appeared very late in the last loading stage when sample damage was already considered to be irreversible. These findings might suggest that in shales these AE events occur but have smaller amplitude and higher frequency events remaining undetected (Eberhardt et al., 1999; Mighani, 2014), or that these AE events are rare as plasticity is the preferred mechanism deformation (Horvath et al., 2015; Kocich et al., 2012; Dobroň, 2016). The consequences of either possibility deserves further investigation as it affects the interpretation of microseismic information used in the evaluation of hydraulic fracture propagation in shales.

References

Aldritch, M. J. (1969). Pore Pressure Effects on Berea Sandstone Subjected to Experimental Deformation. *Geological Society of America Bulletin*, 80, 1577–1586.

ASTM (2014). Standard Test Methods for Compressive Strength and Elastic Moduli of Intact Rock Core Specimens Under Varying States of Stress and Temperatures. D7012−14. *Annual Book of ASTM Standards*.

Baud, P., Zhu, W., Wong, T.F. (2000). Failure Mode and Weakening Effect of Water on Sandstone. *Journal of Geophysical Research*, 105 (B7), 16371–16389.

Brunauer, S., Kantro, D. L., Weise, C. H. (1956) The Surface Energies of Amorphous Silica and Hydrous Amorphous Silica, *Canadian Journal of Chemistry*, 34, 1483–1496.

Byerlee, J. D. (1978). Friction of Rocks. *Pure and Applied Geophysics*, 116, 615–626.

Carneiro, F. L. L. B., (1943) A New Method to Determine the Tensile Strength of Concrete, *Proceedings of the 5th meeting of the Brazilian Association for Technical Rules*, 3 (16), 126–129.

Charles, R. J. (1959). The Strength of Silicate Glasses and Some Crystalline Oxides. Fracture. *Proceedings of an International Conference on the Atomic Mechanisms (*ed. B. L. Averbach, D. K. Felbeck, S. T. Hahn and D. A. Thomas), 225–249.

Chen C.S., Pan E., Amadei B. (1998) Determination of Deformability and Tensile Strength of Anisotropic Rock Using Brazilian Tests. *International Journal of Rock Mechanics and Mining*. 35 (1), 43–61.

Clark, V. A., Tittmann, B. R., Spencer, T. W. (1980) Effect of Volatiles on Attenuation (Q^{-1}) and Velocity in Sedimentary Rocks. *Journal of Geophysical Research*, 85, 5190–5198.

Colback, P. S., Wiid, B. (1965). The Influence of Moisture Content on the Compressive Strength of Rocks. *Proceedings of the Rock Mechanics*, 3, 65–83.

Cooper, H. W. (1979) Attenuation in Igneous Rocks at Seismic Frequencies. Ph.D. Thesis. Massachusetts Institute of Technology, Cambridge, Massachusetts, USA.

Coulomb, C. (1776). Essai Sur une Application des Regles de Maximis et Minimis a Quelqes Problemas de Stratique Relatifs a L'architecture. *Memoires de Mathematique et de physique*, 7, 343–382.

Crawford, A., Wylie, D. (1987). A Modified Multiple Failure State Triaxial Testing Method. *28th US Symposium of Rock Mechanics*, 133–140.

Dobroň, P. (2016) An Acoustic Emission Study of Plasticity in Crystalline Materials. Habilitation Thesis, Charles University. Prague, Czech Republic.

Demarco, M. M., Jahns, E., Rüdrich, J., Oyhantcabal, P., Siegesmund, S. (2007). The Impact of Partial Water Saturation on Rock Strength: An Experimental Study on Sandstone. *German Journal of Geology*. 58 (4), 869–882.

Donath, F. A. (1964) Strength Variation and Deformational Behavior in Anisotropic Rock. *State of the Earth in the Earth's Crust*. New York: Elsevier, 281–298.

Eberhardt, E., Stimpson, B., Stead, D. (1999). Effects of Grain Size on the Initiation and Propagation Thresholds of Stress–Induced Brittle Fractures. *Rock Mechanics and Rock Engineering*, 32 (81), 81–99.

Evans, B., Fredrich, J. T., Wong, T. (1990). The Brittle–Ductile Transition in Rocks: Recent Experimental and Theoretical Progress. *Geophysical Monograph*, 56, 1–20.

Fairbairn, E. M. R., Ulm, F. J. (2002) A Tribute to Fernando L. L. B. Carneiro (1913 – 2001) Engineer and Scientist Who Invented the Brazilian Test. *Materials and Structures/Matériaux et Constructions*, 35, 195–196.

Fjær, E, Nes, O. M. (2013). Strength Anisotropy of Mancos Shale. *47th U.S. Rock Mechanics/Geomechanics Symposium*.

Frocht, M. M. (1948). Photoelasticity, 2. New York, Wiley.

GCTS (2008). CATS Triaxial Test Mode 2.00. Tempte, AZ. GCTS Testing Systems.

Gnirk, P., Cheatham, J. (1963). Indentation Experiments on Dry Rocks Under Pressure. *Journal of Petroleum Technology*, 15 (9), 1031–1039.

Griffith, A. (1921). The Phenomena of Rupture and Flows in Solids. *Philosophical Transactions of the Royal Society of London*, 221, 163–198.

Hallbauer, D. K., Wagner, H., Cook, N. G. (1973). Some Observations Concerning the Microscopic and Mechanical Behavior of Quartzite Specimens in Stiff, Triaxial Compression Test. *International Journal of Rock Mechanics and Mining Sciences Geomechanics Abstracts*, 10 (6), 713–726.

Handin, J., and Hager, R. V., Jr. (1957) Experimental Deformation of Sedimentary Rocks Under Confining Pressure: Tests at Room Temperature on Dry Samples. *Bulletin American Association of Petroleum Geologists*, 41, 1–50.

Handin, J. (1969). On the Coulomb–Mohr Failure Criterion. *Journal of Geophysical Research*, 74 (22), 5343–5348.

Hawkins, A. B., McConnell, B. J. (1992) Sensitivity of Sandstone Strength and Deformability to Changes in Moisture Content. *Quarterly Journal of Engineering Geology*, 25, 115–130.

Hertz, H. R. (1895). *Gesammelte Werke (Collected Works)*, 1. Leipzig, Germany.

Horváth, K., Drozdenko, D., Máthis, K., Bohlen, J. Dobroň, P. (2016) Deformation Behavior and Acoustic Emission Response on Uniaxial Compression Of Extruded Rectangular Profile of Mg–Zn–Zr Alloy. *Journal of Alloys and Compounds*, 680 (2016) 623–632.

Hsu, N., Breckenridge, F. R. (1981). Characterization and Calibration of Acoustic Emission Sensors. *Materials Evaluation*, 39 (1), 60–68.

Inglis, C. (1913). Stresses in A Plate Due to The Presence of Cracks and Sharp Corners. *Transactions of the Institute of Naval Architects*, 55, 219–242.

Irwin, G. (1957). Analysis of Stresses and Strains Near the End of a Crack Traversing. *Journal of Applied Mechanics*, 24, 361–364.

ISRM (1978). Suggested Methods for Determining Tensile Strength of Rock Materials. *International Journal of Rock Mechanics and Mining Sciences Geomechanics Abstracts*, 15 (3), 99–103.

Jaeger, J.C. (1971). Friction of Rocks and Stability of Rock Slopes. *Geotechnique*, 21, 91–134.

Jaeger, J.C., Cook, N.G.W. (1979) Fundamentals of Rock Mechanics, 3rd edition. Chapman and Hall, London.

Karastathis, A. (2007). Petrophysical Measurements on a Tight Gas Shale. M.S. Thesis. The University of Oklahoma, Norman, Oklahoma, USA.

Kim, M. M., Ko, H. Y. (1979). Multistage Triaxial Testing of Rocks. *Geotechnical Testic Journal*, 2 (2), 98–105.

Kocich, R., Cagala, M., Crha, J. Kozelsky, P. (2012). Character of Acoustic Emission Signal Generated During Plastic Deformation. *30th European Conference on Acoustic Emission Testing & 7th International Conference on Acoustic Emission*.

Kovári, K., Tisa, A. (1975). Multiple Failure State and Strain Controlled Triaxial Tests. *Rock Mechanics*, 7, 17–33.

Mammen, J., Saydam, S., Hagan, P. A. (2009) A Study on the Effect of Moisture Content on Rock Cutting Performance. *Coal 2009: Coal Operators' Conference*. 340–347.

Martin, C. D. (1993). Strength of Massive Lac du Bonnet Granite Around Underground Openings. Ph.D. Thesis, University of Manitoba. Winnipeg, Manitoba, Canada.

Masuda, K. (2000). Effects of Water on Rock Strength in Brittle Regime. *Journal of Structural Geology*, 23, 1653–1657.

McLamore, R., Gray K.E. (1967) The Mechanical Behavior of Anisotropic Sedimentary Rocks. *Journal of Manufacturing Science and Engineering*, 89, 62–76.

Mighani, S. (2014). Rock Tensile Failure Related to Improving Hydraulic Fracture. M.S. Thesis. The University of Oklahoma, Norman, Oklahoma, USA.

Mohr, O. (1882). Concerning the Representation of the Stress State of a Body Element. *Zivilingenieure*, 28, 113–156.

Monicard, R. (1980). Properties of Reservoir Rocks: Core Analysis. Paris, Springer.

O'Connell, R.J., Budiansky B. (1974). Seismic Velocities in Dry and Saturated Cracked Solids. *Journal of Geophysical Research*, 82, 5719–5736.

Ojala, I. O. (2011). The Effect of CO_2 On the Mechanical Properties of Reservoir and Cap Rock. *Energy Procedia*, 4, 5392–5397.

Ojo, O., Brook, N. (1989). The Effect of Moisture on Some Mechanical Properties of Rock. *Mining Science and Technology,* 10, 145–156.

Orowan, E. (1960). Mechanism of Seismic Faulting. *Geological Society of America Memoir*, 79, 323–345.

Pagoulatos, A. (2004). Evaluation of Multistage Triaxial Testing on Berea Sandstone. M.S. Thesis. The University of Oklahoma, Norman, Oklahoma, USA.

Parks, G. A. (1984). Surface and Interfacial Free Energies of Quartz. *Journal of Geophysical Research,* 89 (B6), 3997–4008.

Paterson, M., Wong, T.F. (1977). Experimental Rock Deformation – The Brittle Field. Berlin, Springer.

Reichardt, C. (2003). Solvents and Solvent Effects in Organic Chemistry, 3. Wiley.

Scholz, C. (1988). The Brittle–Plastic Transition and The Depth of Seismic Faulting. *Geologische Rundschau,* 77 (1), 319–328.

Sondergeld, C., Rai, C. (1993). A New Exploration Tool: Quantitative Core Characterization. *Pageoph,* 141, 249–268.

Spencer, J. W. (1981). Stress Relaxations at Low Frequencies in Fluid–Saturated Rocks: Attenuation and Modulus Dispersion. *Journal of Geophysical Research*. 86 (B3), 1803–1812.

Tada, H., Paris, P., Irwin, G. (1985). The Stress Analysis of Cracks Handbook, 2nd ed. St. Louis, Missouri: Paris Productions Inc.

Tavallali, A., Vervoort, A. (2013). Behavior of Layered Sandstone Under Brazilian Test Conditions: Layer Orientation and Shape Effects. *Journal of Rock Mechanics and Geotechnical Engineering*. 5 (5), 366–377.

TCNA. (2015). Lyons Sandstone Test Summaries. Lyons Sandstone Quarry and Fabrication.

Tittmann, B. R., Clark, V. A., Richardson, J. M., Spencer, T. W. (1980). Possible Mechanism of Seismic Attenuation in Rocks Containing Small Amounts of Volatiles, *Journal of Geophysical Research, 85, 5199–5208.*

Toksöz, M. N., Johnston, D. H. (1981). Seismic Wave Attenuation. *Society of Exploration Geophysicists*. Reprint Series 2.

Twiss, R., Moores, E. (1992). Structural Geology. New York, W.H. Freeman and Company.

Van Voorhis, J. J., Craig, R. G., Bartel, F. E. (1957). Free Energy of Immersion of Compressed Powders with Different Liquids, II, Silica Powder. *The Journal of Physical Chemistry*, 61, 1513–1519.

Vásárhelyi, B., Ván, P. (2006) Influence of Water Content on the Strength of Rock. *Engineering Geology,* 84, 70–74

Wilhelmi, B., Somerton, W. H. (1967). Simultaneous Measurement of Pore and Elastic Properties of Rocks Under Triaxial Test Conditions. *Society of Petroleum Engineers Journal*, 7 (3), 283–294.

Wong, L. N. Y., Maruvanchery, V., Liu, G. (2016). Water Effects on Rock Strength and Stiffness Degradation. *Acta Geotechnica*, 11, 713–737.

Yagiz, S. (2009). Assessment of Brittleness Using Rock Strength and Density with Punch Penetration Test. *Tunnelling and Underground Space Technology*. 24, 66–74.

Zehnder, A. (2012). Fracture Mechanics. Netherlands, Springer.

Appendix I-I: Stress Paths and Failure Envelopes (Sandstones)

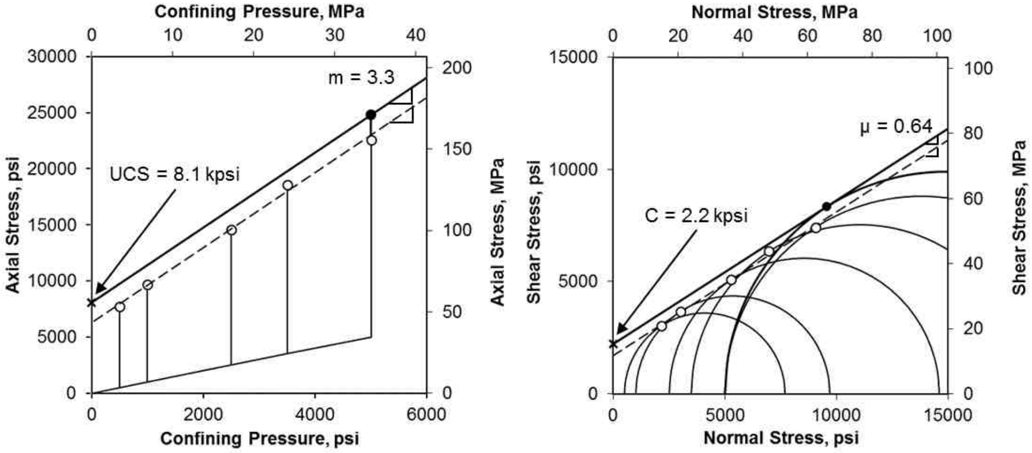

Figure AI-I.1 Stress path and failure envelope of dry Berea sandstone

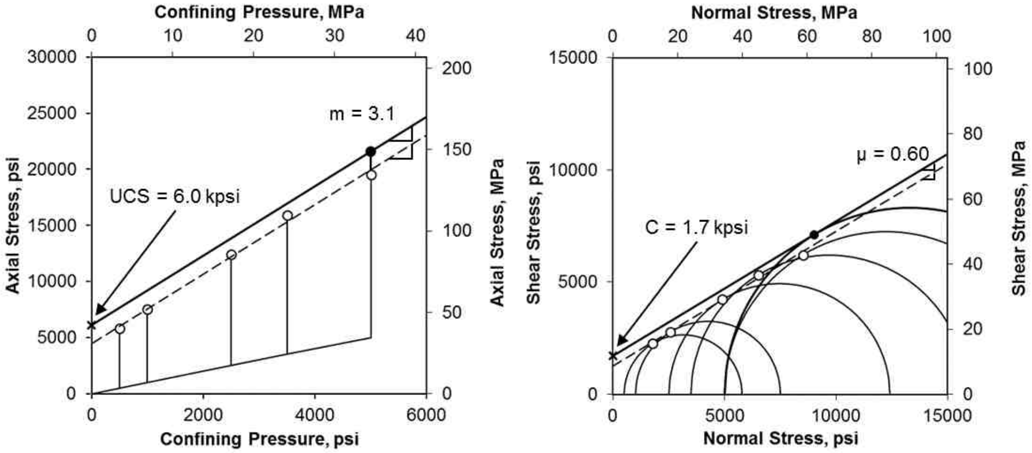

Figure AI-I.2 Stress path and failure envelope of brine saturated Berea sandstone

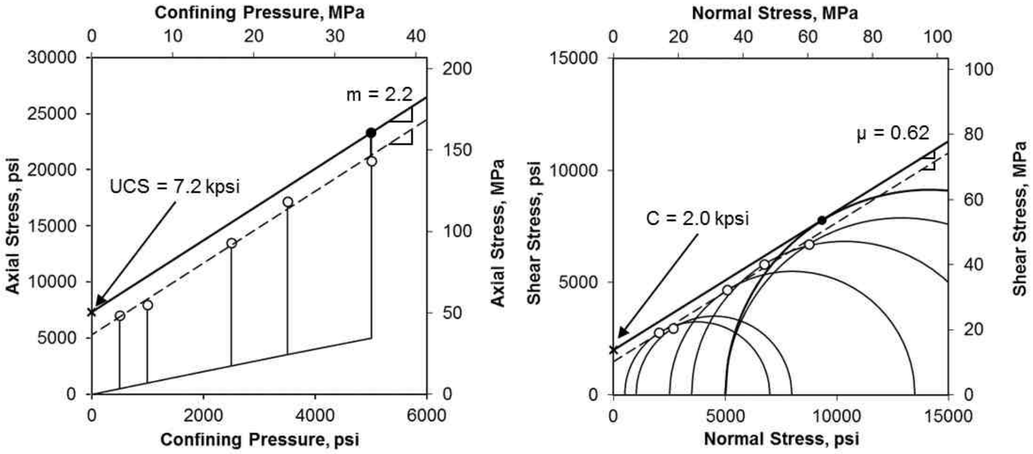

Figure AI-I.3 Stress path and failure envelope of dodecane saturated Berea sandstone

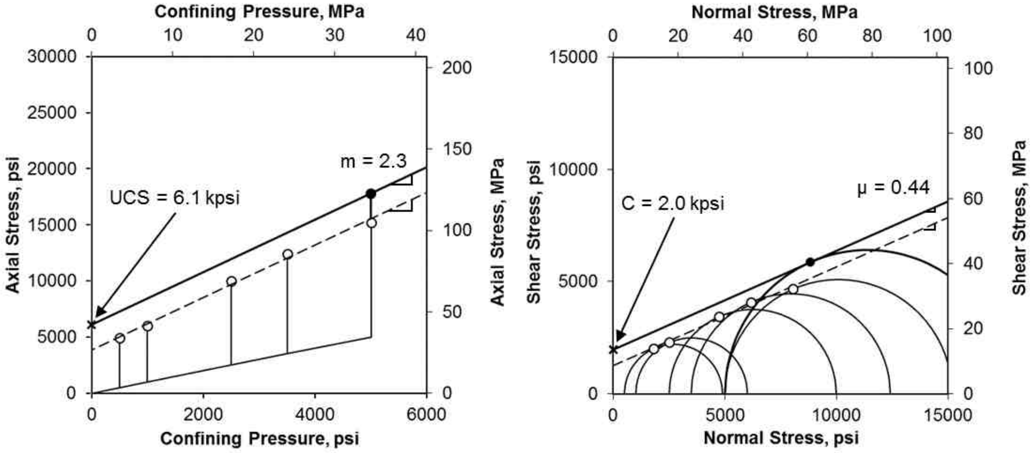

Figure AI-I.4 Stress path and failure envelope of dry Bandera sandstone

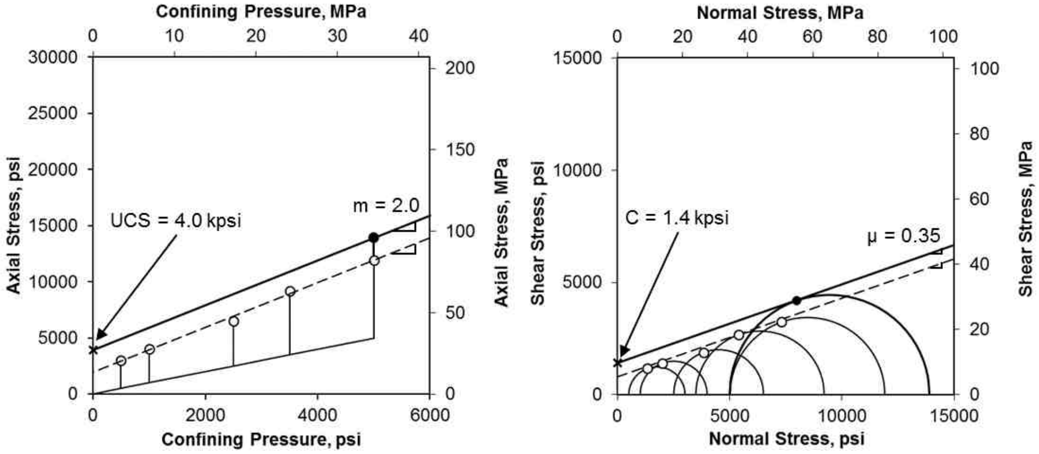

Figure AI-I.5 Stress path and failure envelope of brine saturated Bandera sandstone

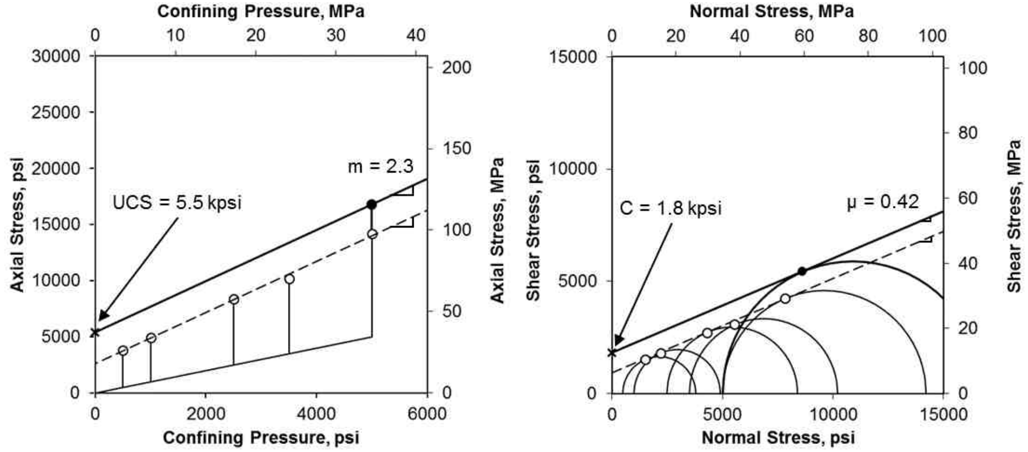

Figure AI-I.6 Stress path and failure envelope of dodecane saturated Bandera sandstone

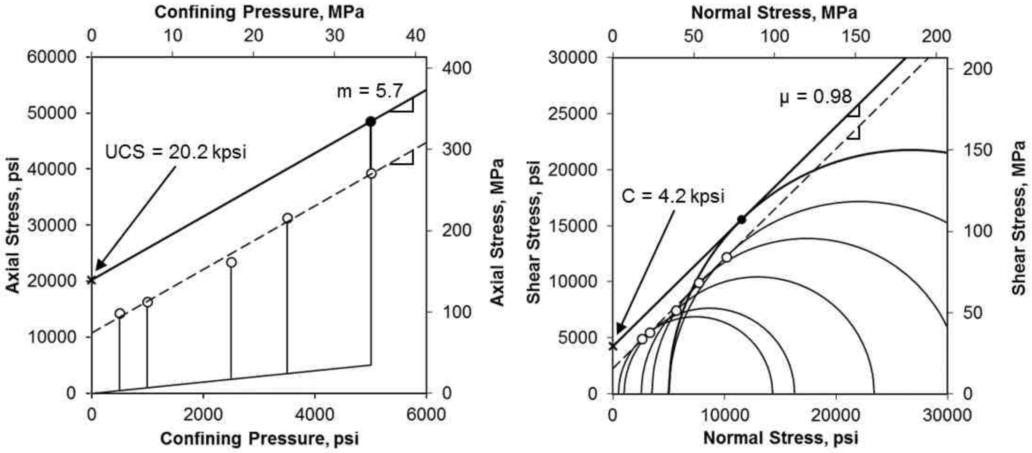

Figure AI-I.7 Stress path and failure envelope of dry Lyons sandstone

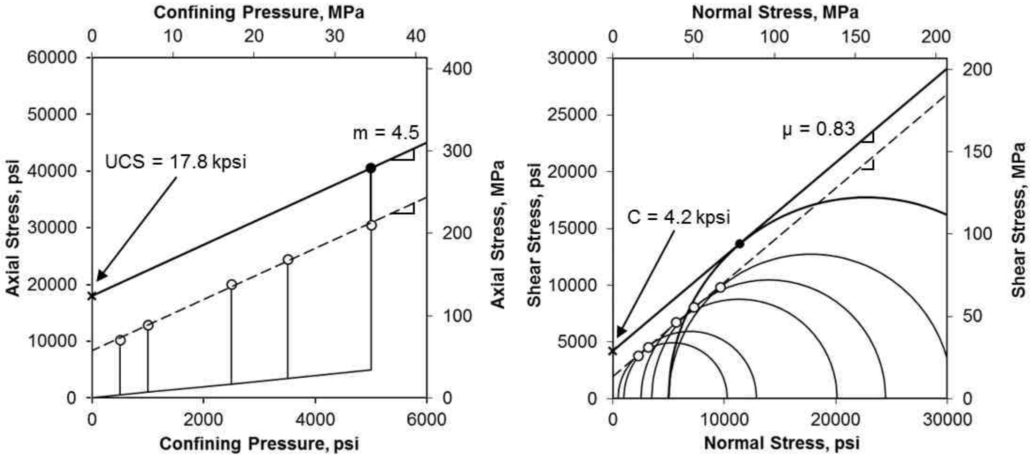

Figure AI-I.8 Stress path and failure envelope of brine saturated Lyons sandstone

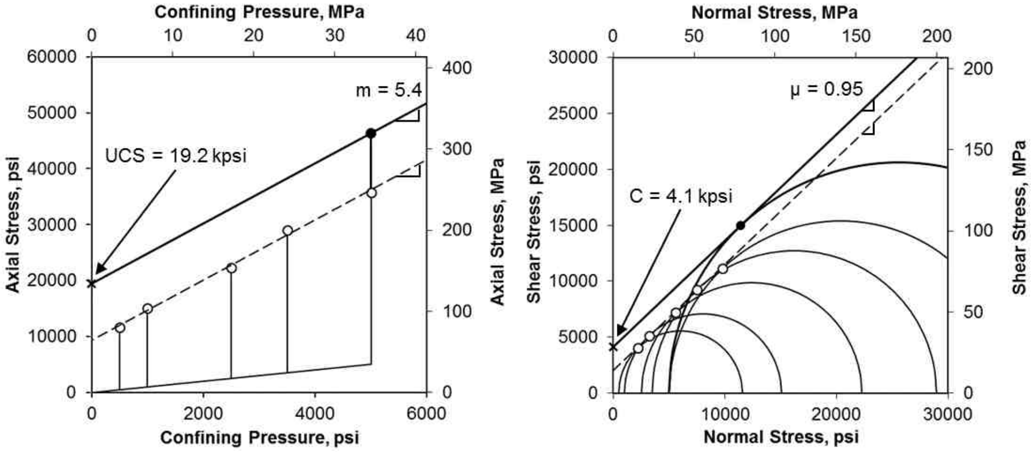

Figure AI-I.9 Stress path and failure envelope of dodecane saturated Lyons sandstone

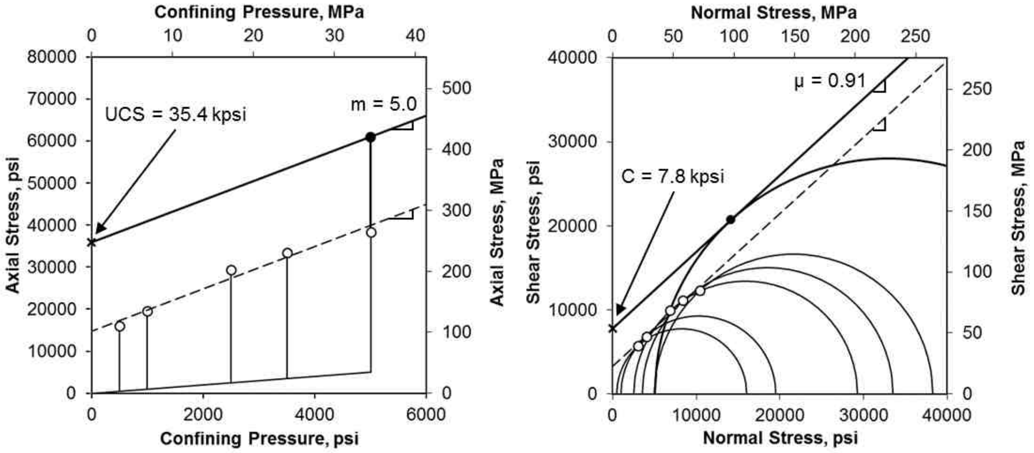

Figure AI-I.10 Stress path and failure envelope of dry Tennessee sandstone

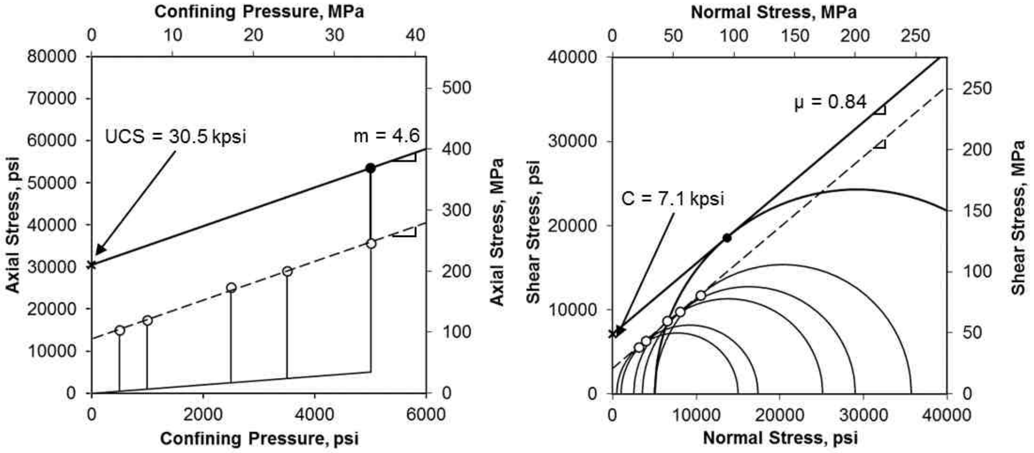

Figure AI-I.11 Stress path and failure envelope of brine saturated Tennessee sandstone

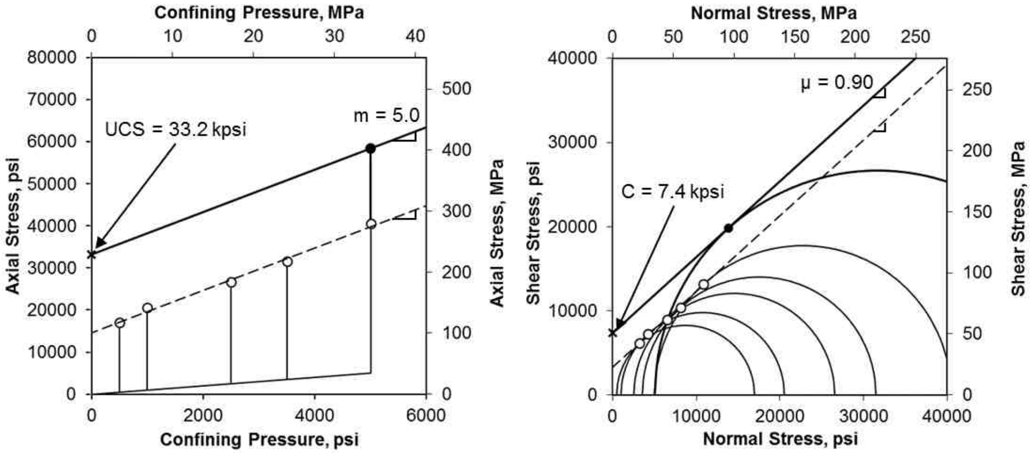

Figure AI-I.12 Stress path and failure envelope of dodecane saturated Tennessee sandstone

Appendix I-II: Stress Paths and Failure Envelopes (Shales)

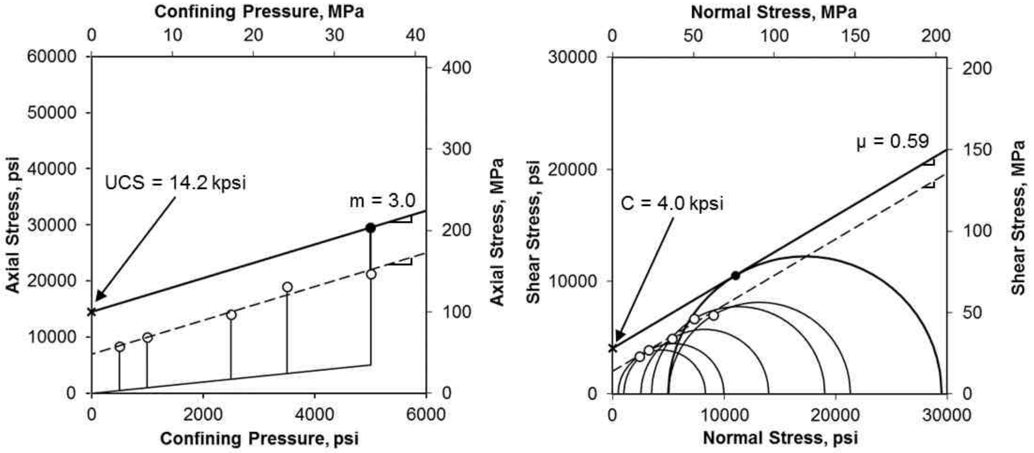

Figure AI-II.1 Stress path and failure envelope of Woodford 9654.29’

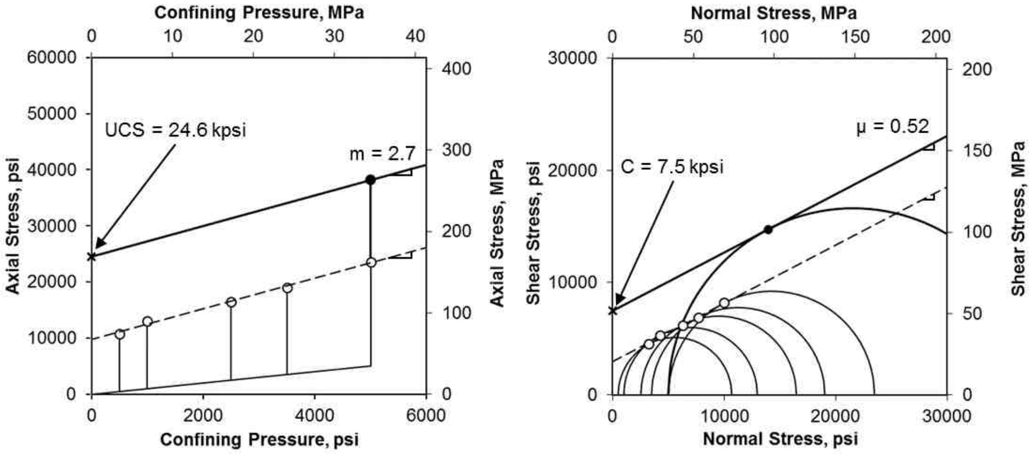

Figure AI-II.2 Stress path and failure envelope of Eagle Ford 11094.89’

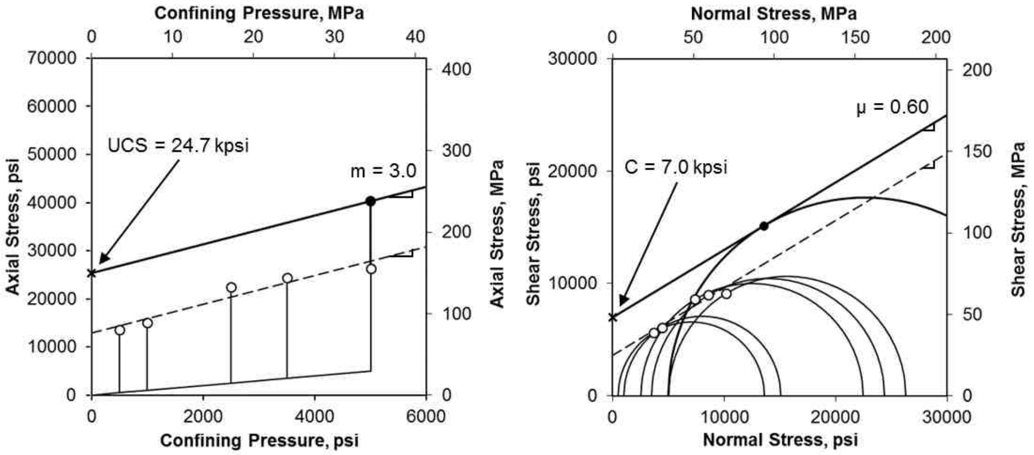

Figure AI-II.3 Stress path and failure envelope of Eagle Ford 11115.35’

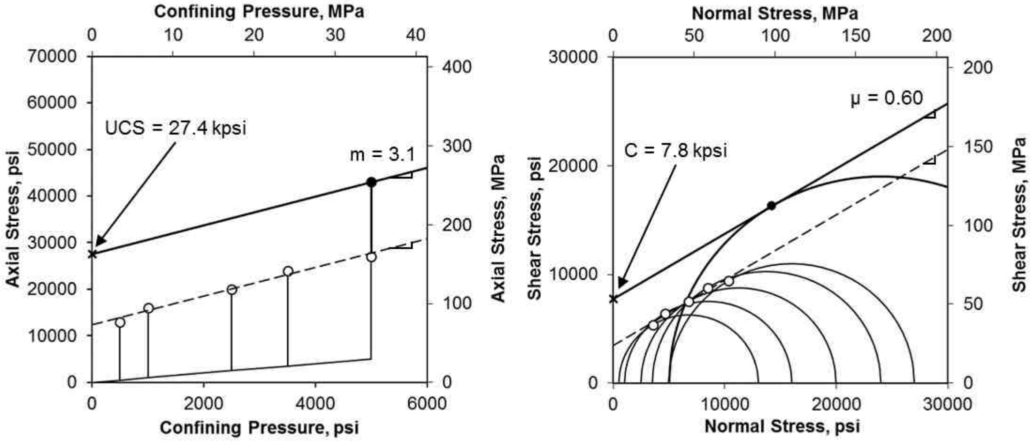

Figure AI-II.4 Stress path and failure envelope of Eagle Ford 11204.47’

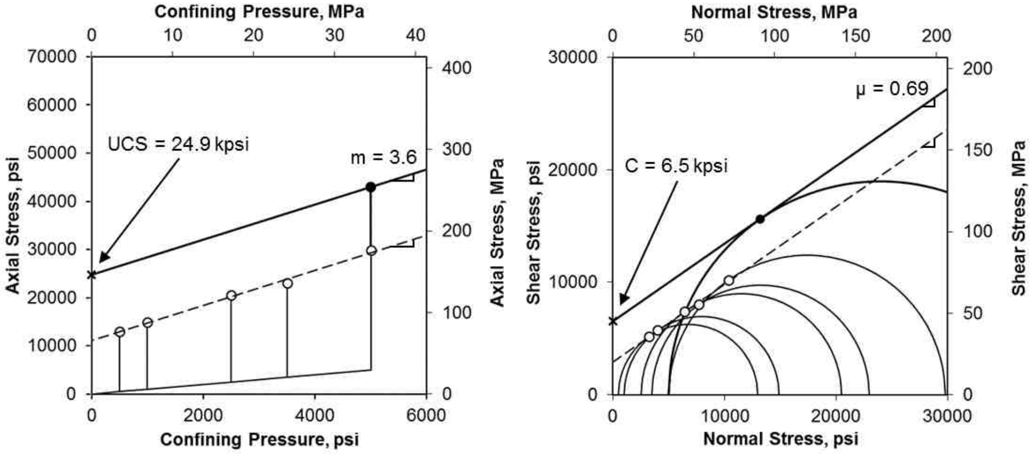

Figure AI-II.5 Stress path and failure envelope of Eagle Ford 11216.15’

Appendix II-I: Stress-Strain Curves and AE Counts (Sandstones)

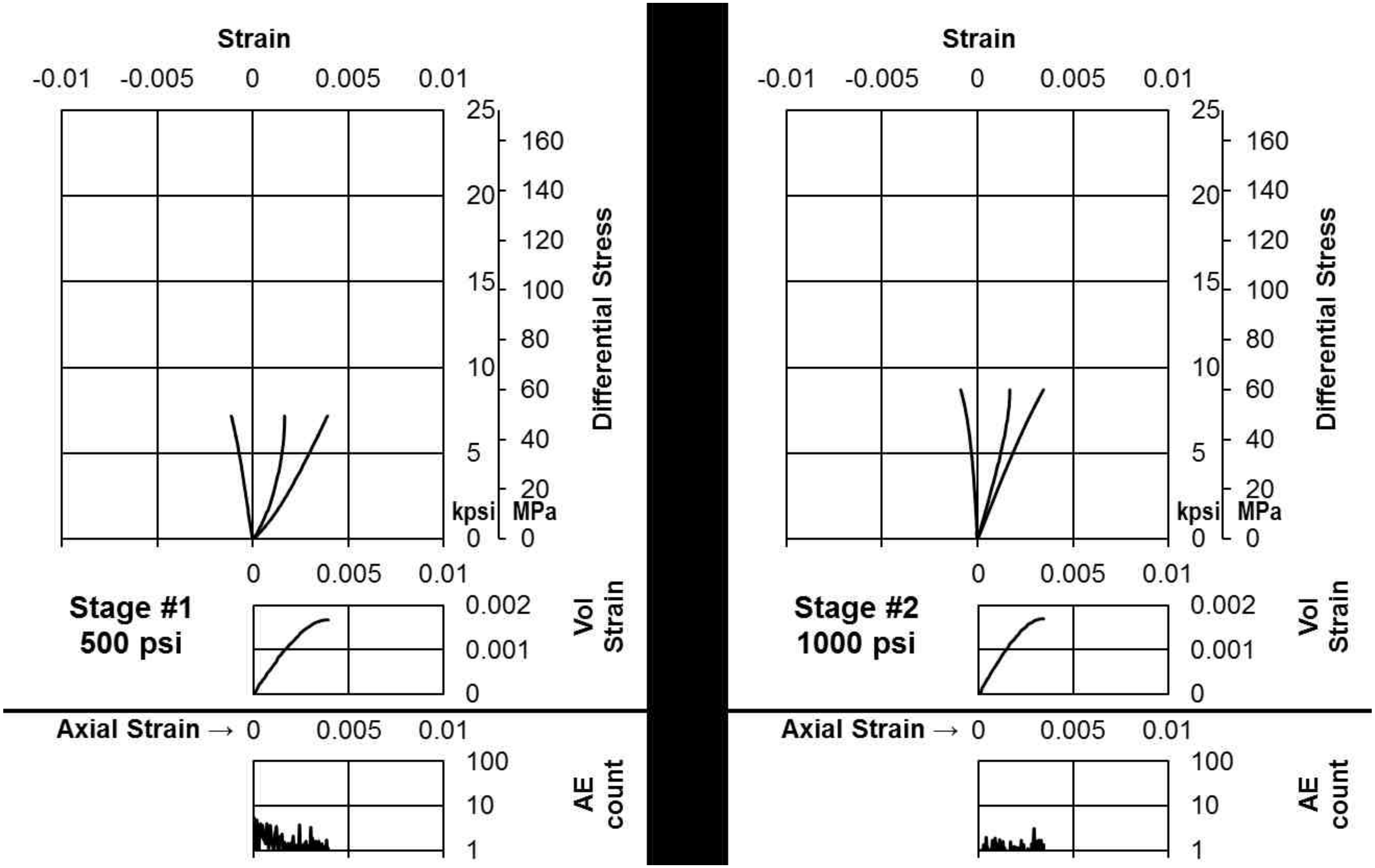

Figure AII-I.1a Stress-strain curves of room dry Berea Sandstone (Stage 1 and 2)

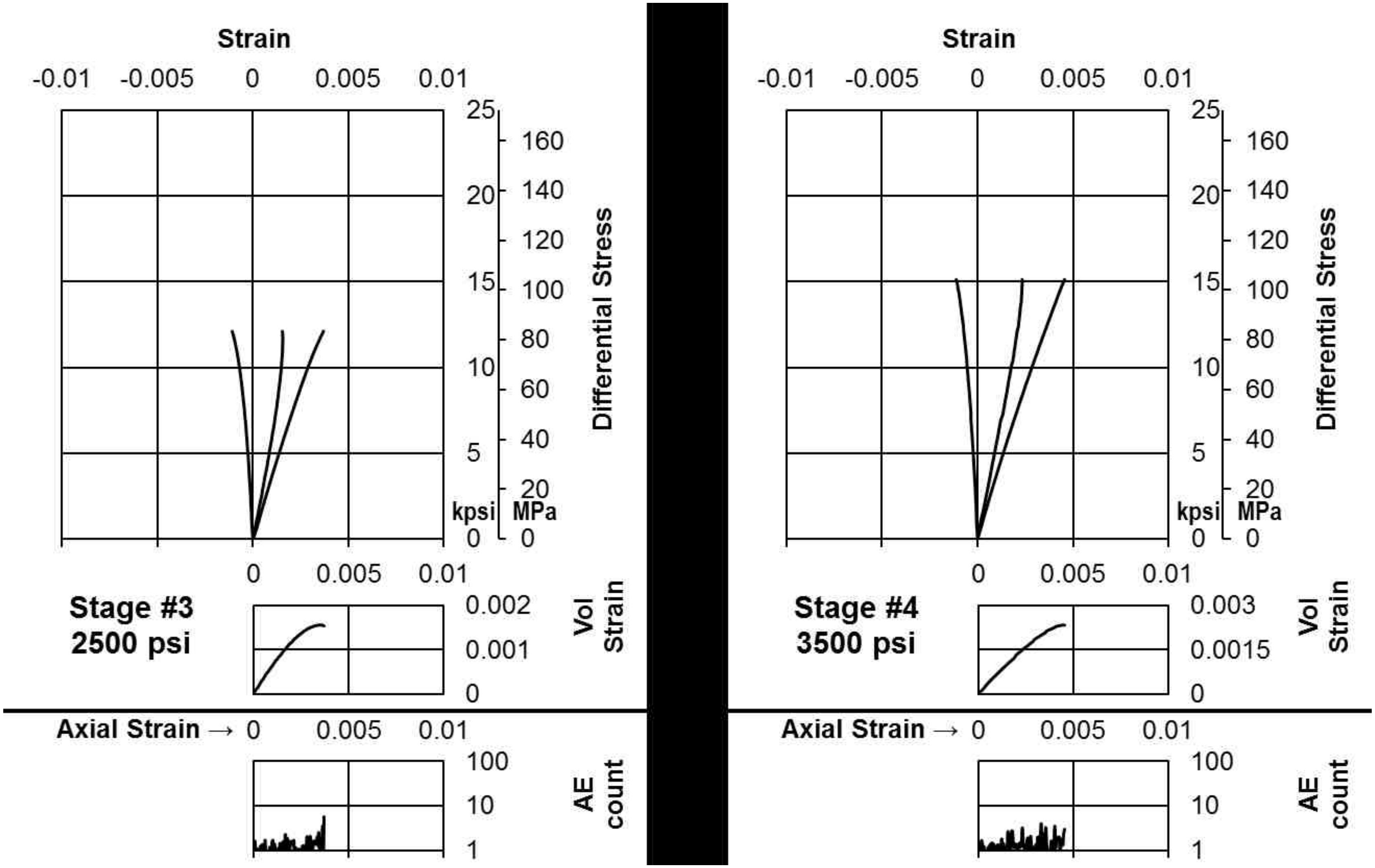

Figure AII-I.1b Stress-strain curves of room dry Berea Sandstone (Stage 3 and 4)

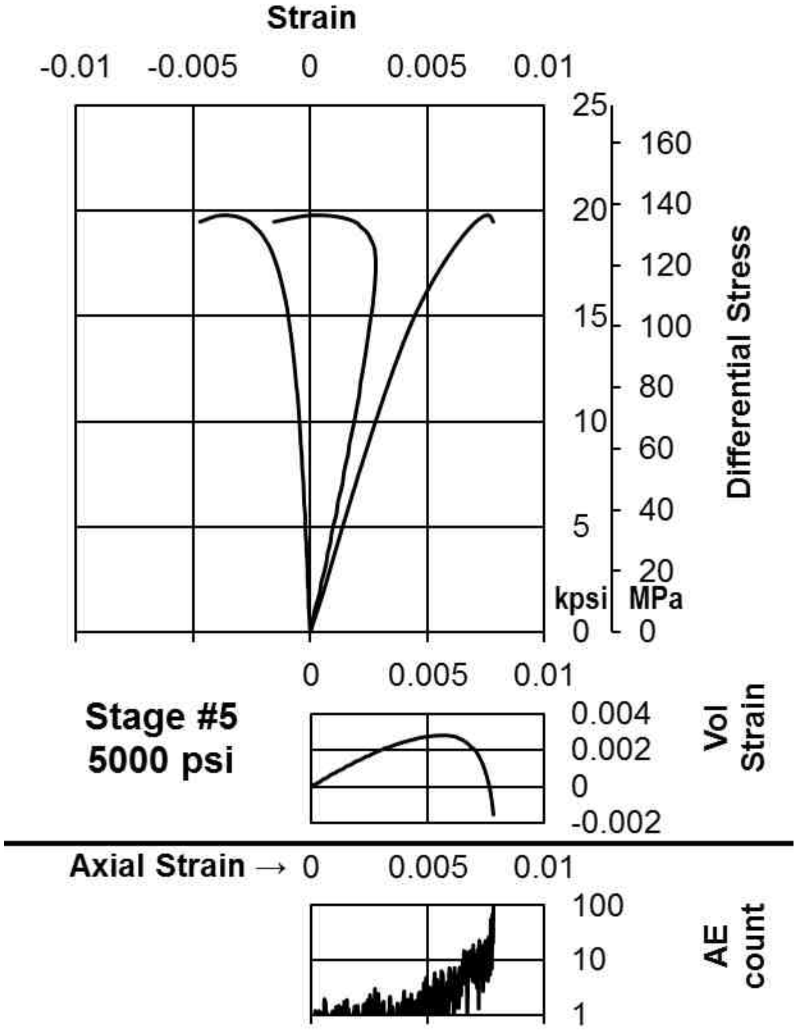

Figure AII-I.1c Stress-strain curves of room dry Berea Sandstone (Stage 5)

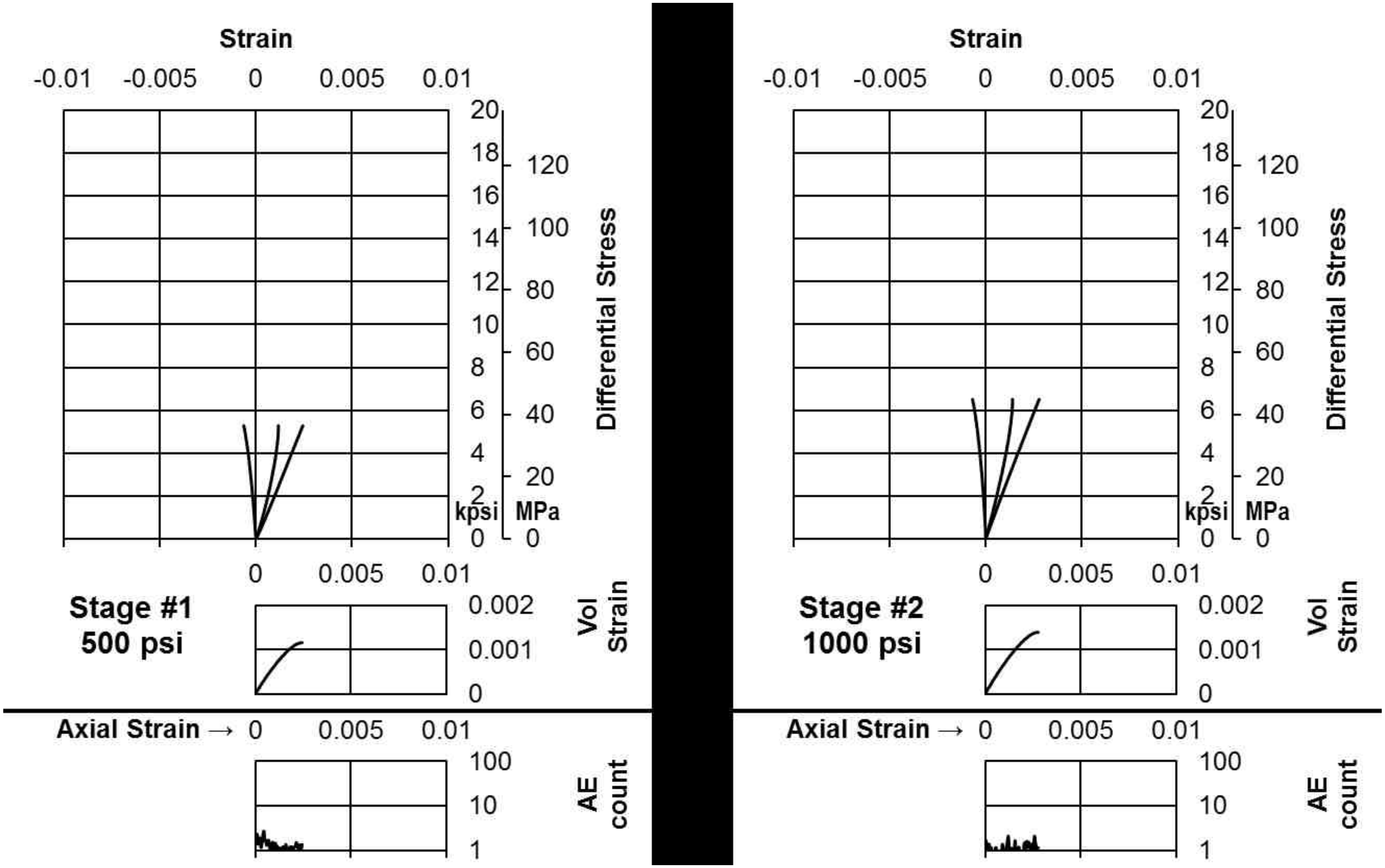

Figure AII-I.2a Stress-strain curves of brine saturated Berea Sandstone (Stage 1 and 2)

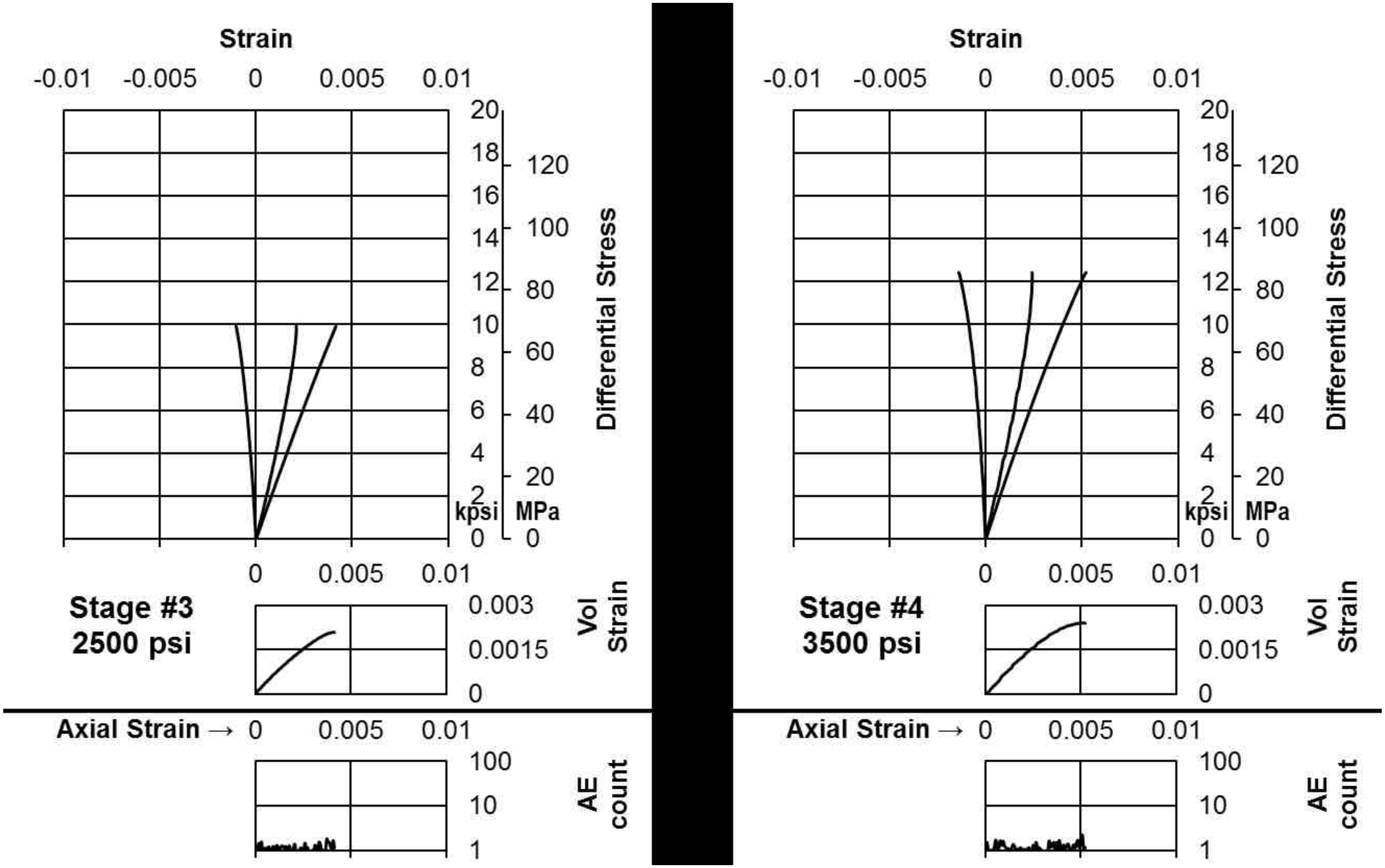

Figure AII-I.2b Stress-strain curves of brine saturated Berea Sandstone (Stage 3 and 4)

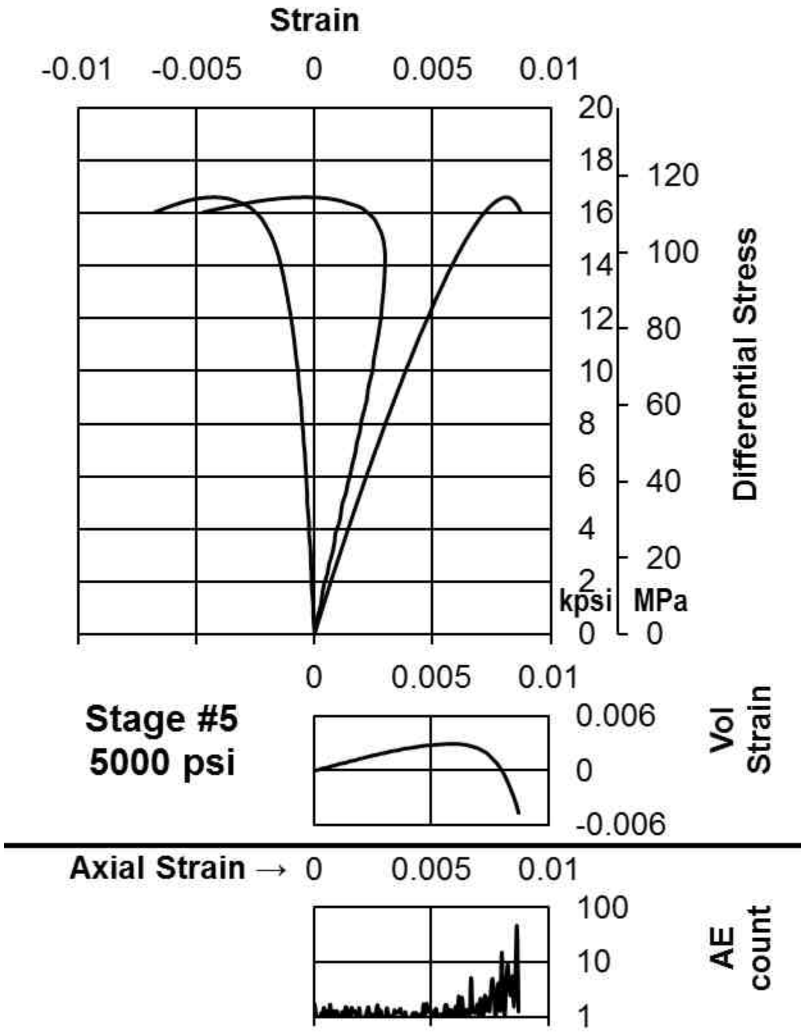

Figure AII-I.2c Stress-strain curves of brine saturated Berea Sandstone (Stage 5)

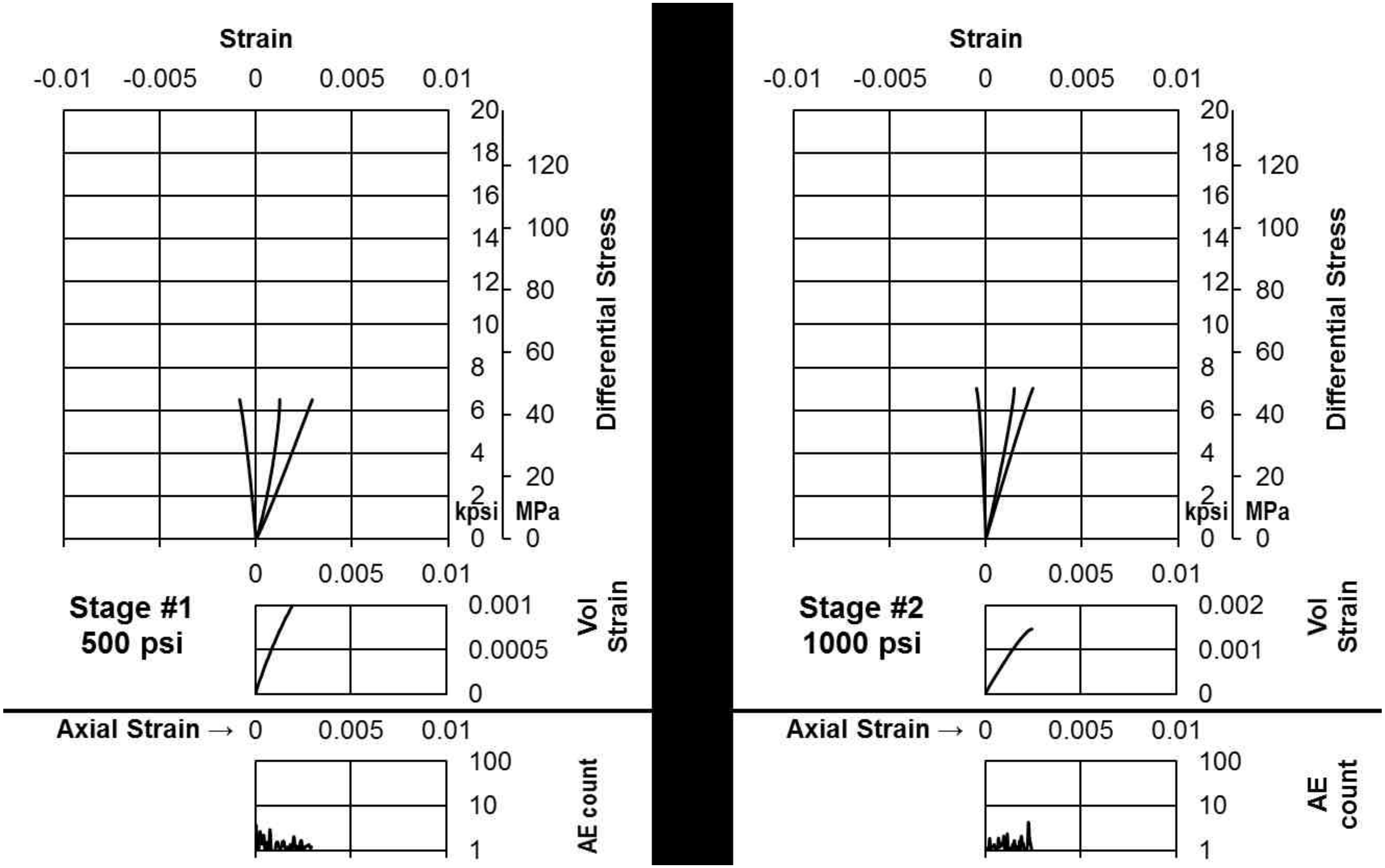

Figure AII-I.3a Stress-strain curves of dodecane saturated Berea Sandstone (Stage 1 and 2)

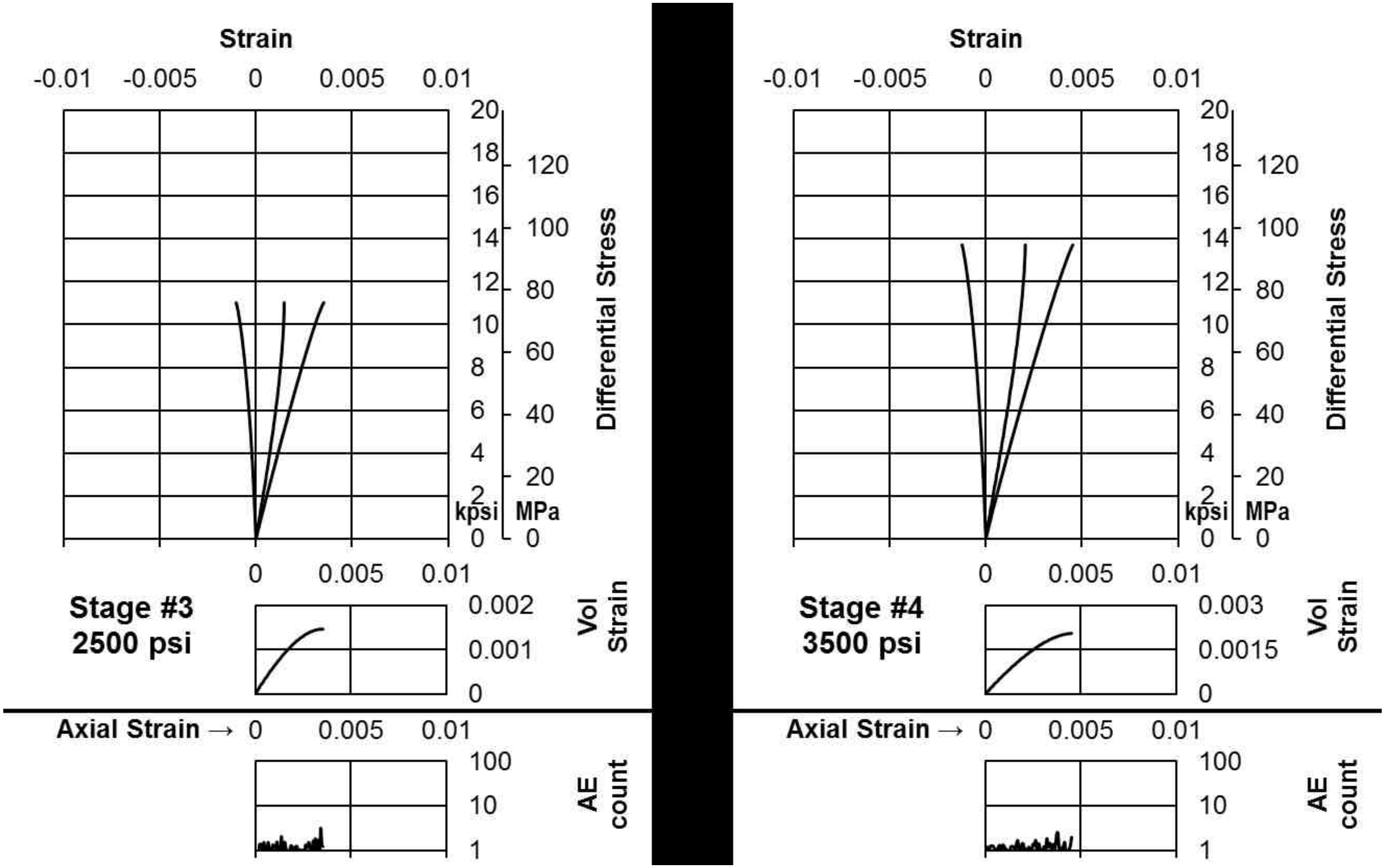

Figure AII-I.3b Stress-strain curves of dodecane saturated Berea Sandstone (Stage 3 and 4)

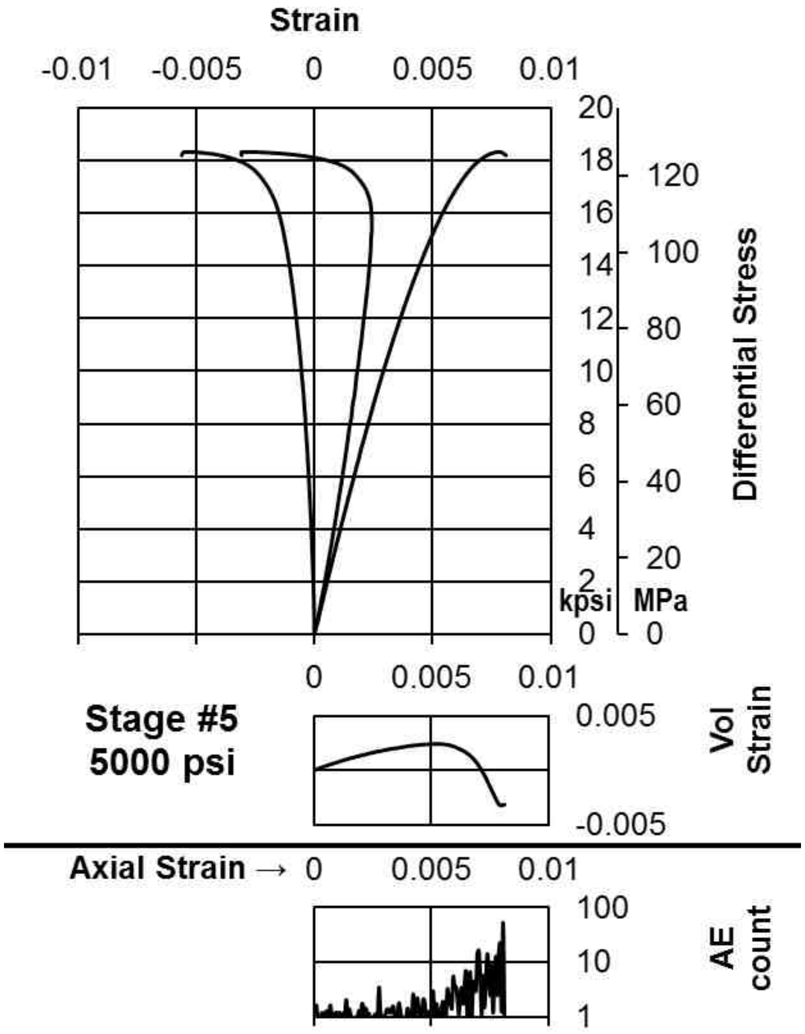

Figure AII-I.3c Stress-strain curves of dodecane saturated Berea Sandstone (Stage 5)

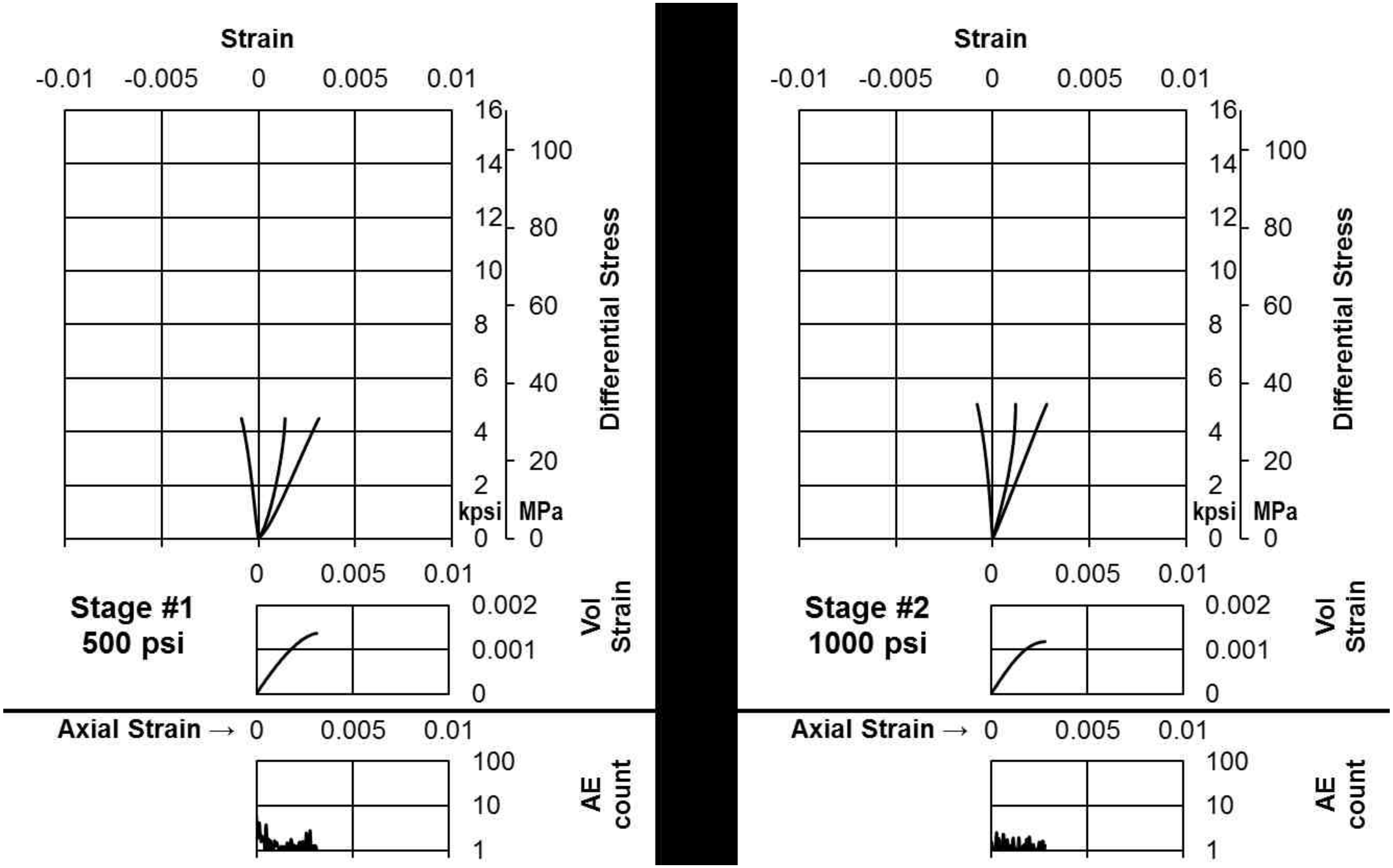

Figure AII-I.4a Stress-strain curves of room dry Bandera Sandstone (Stage 1 and 2)

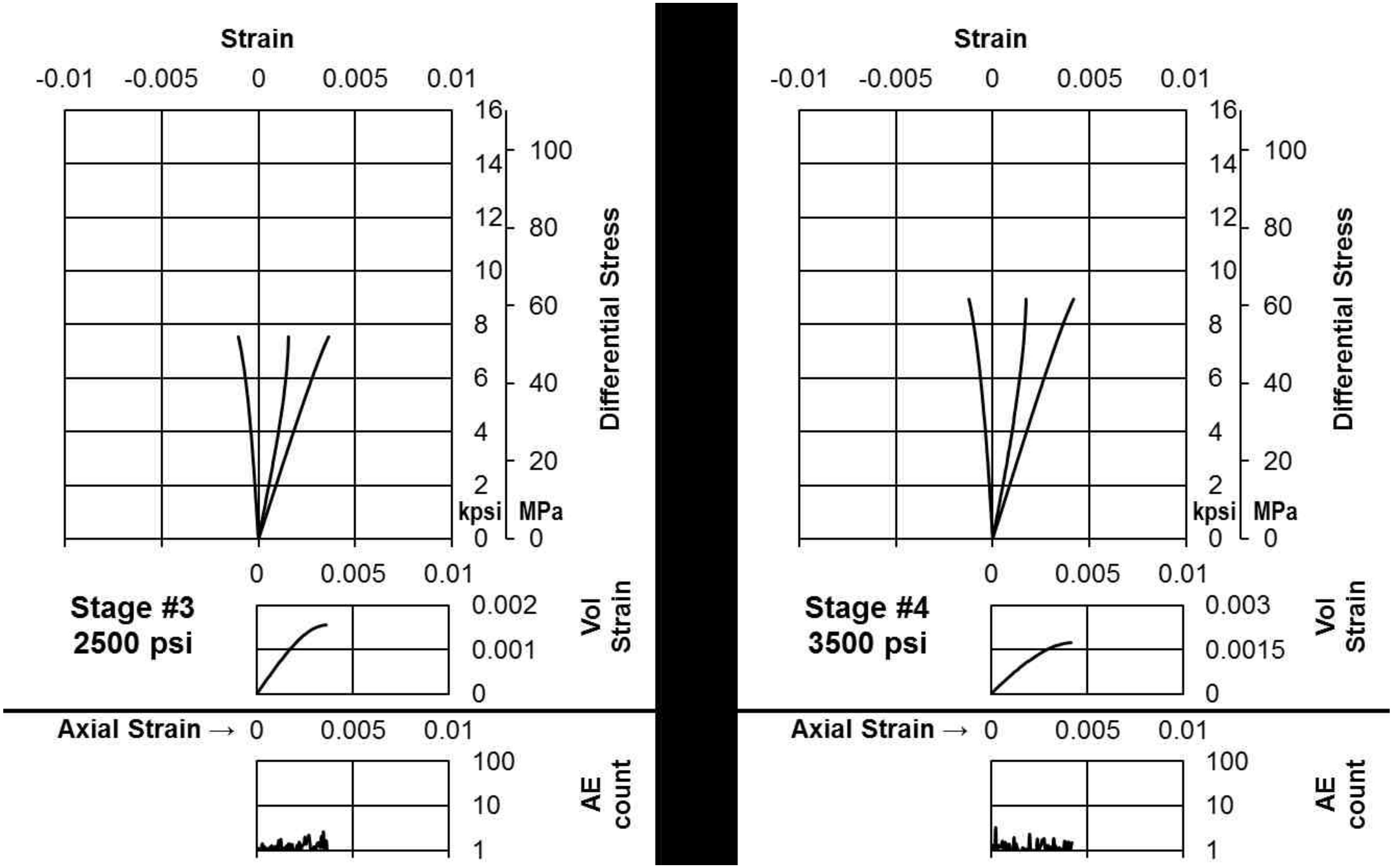

Figure AII-I.4b Stress-strain curves of room dry Bandera Sandstone (Stage 2 and 3)

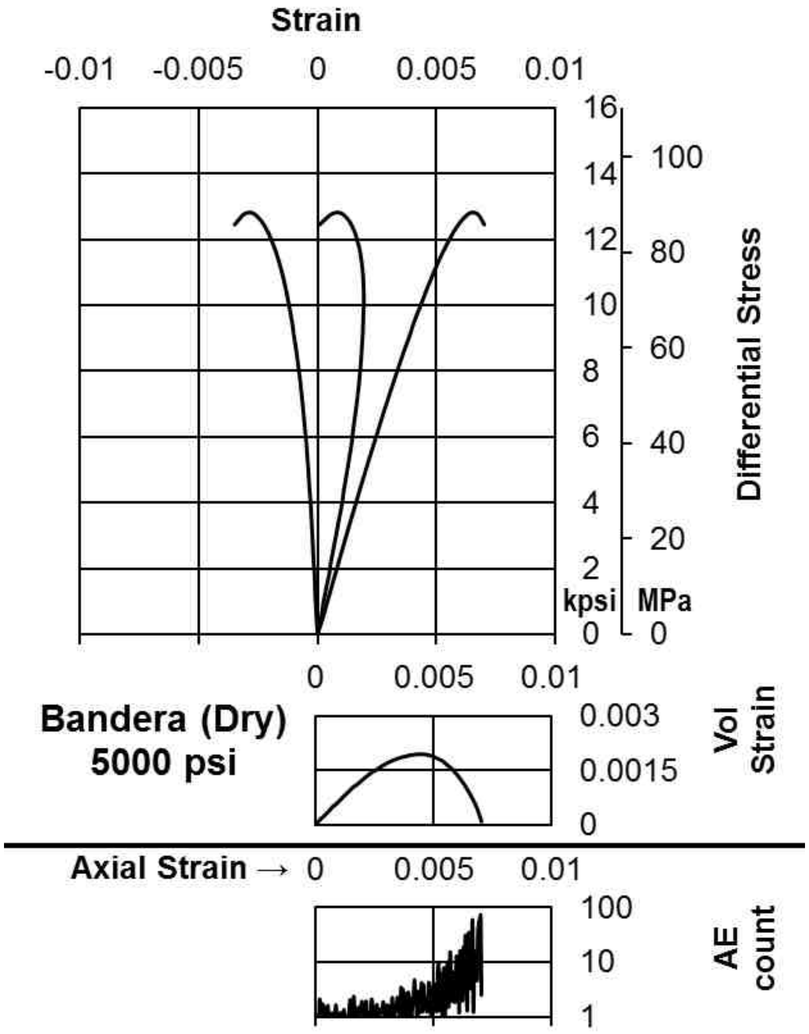

Figure AII-I.4c Stress-strain curves of room dry Bandera Sandstone (Stage 5)

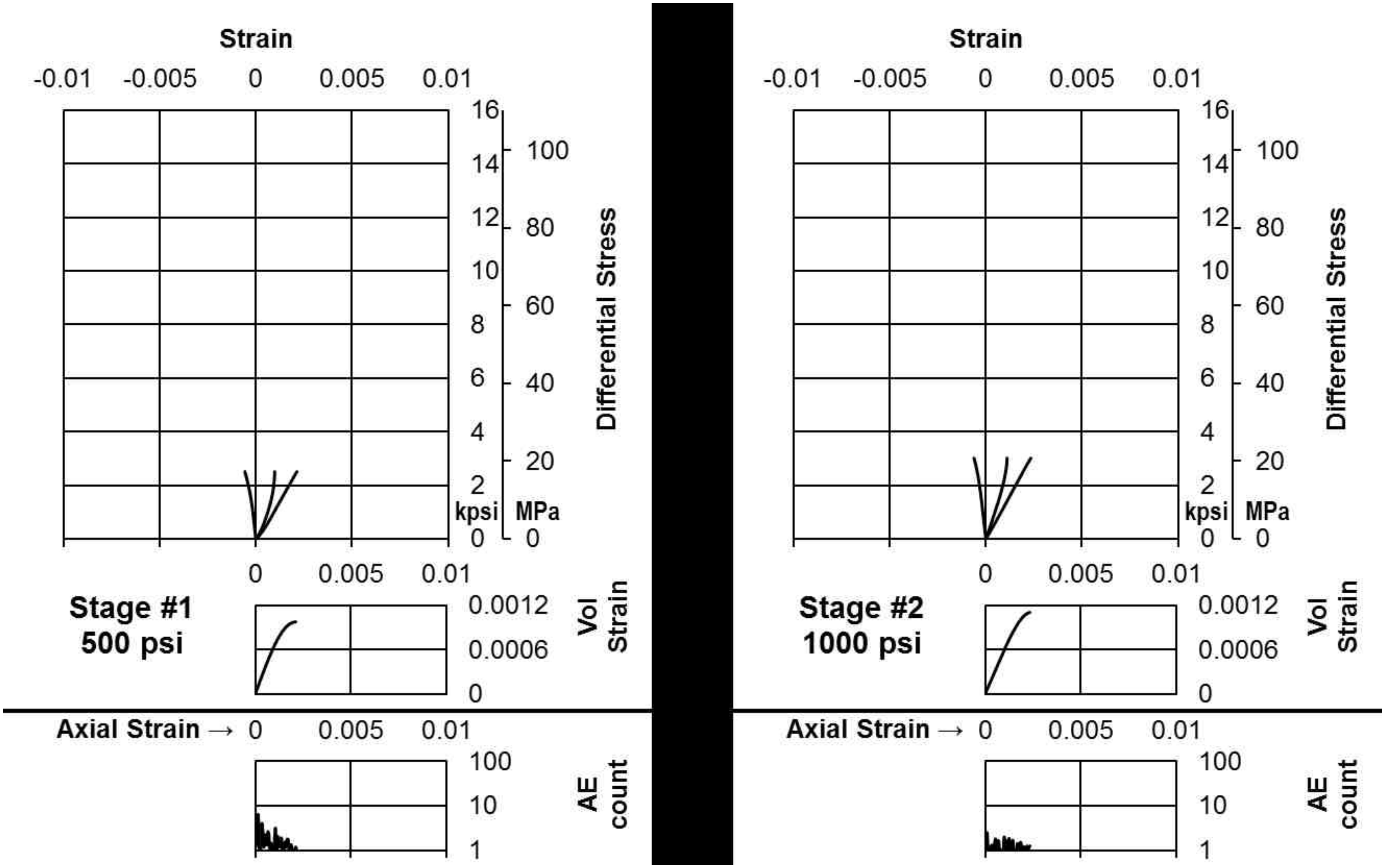

Figure AII-I.5a Stress-strain curves of brine saturated Bandera Sandstone (Stage 1 and 2)

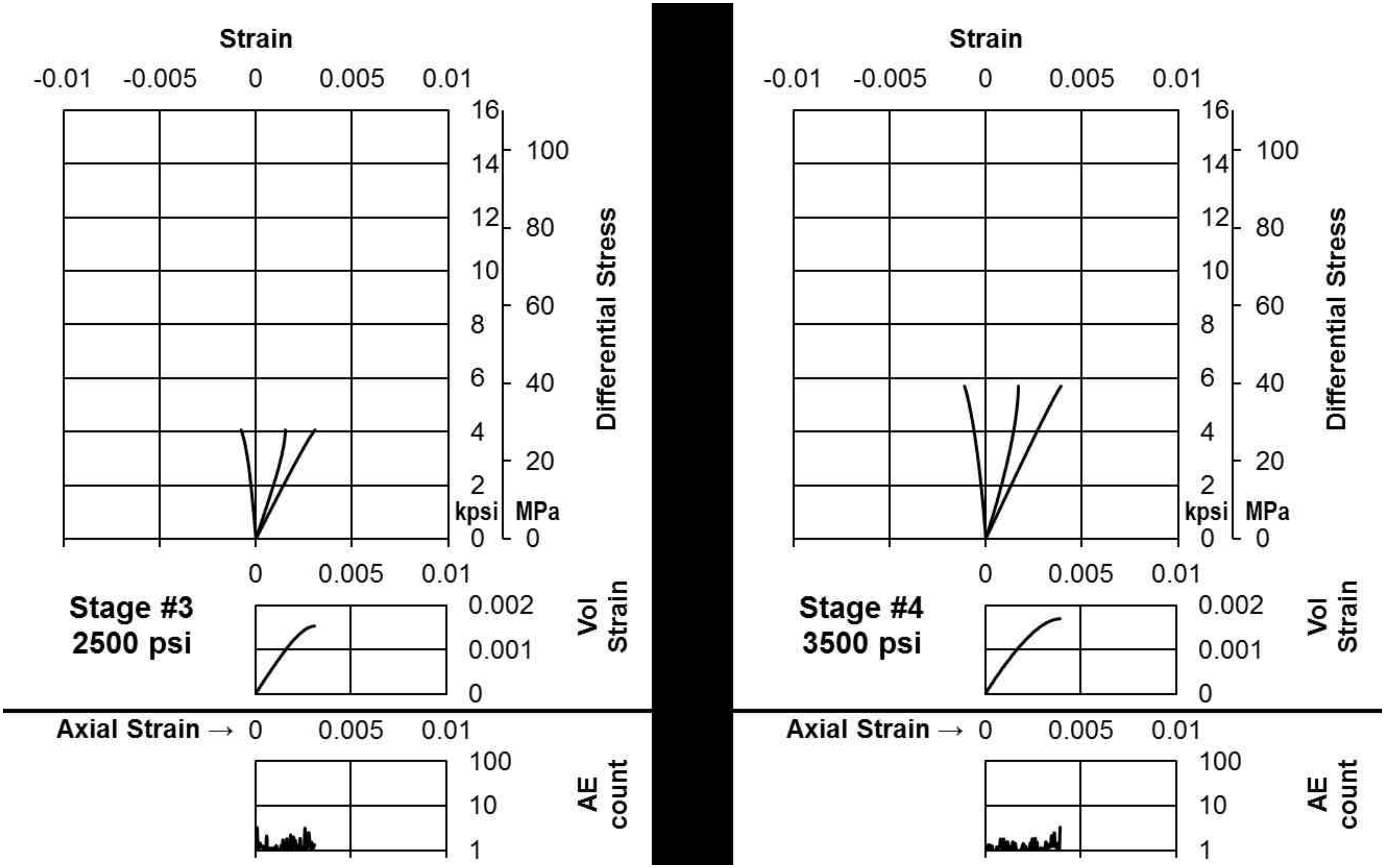

Figure AII-I.5b Stress-strain curves of brine saturated Bandera Sandstone (Stage 3 and 4)

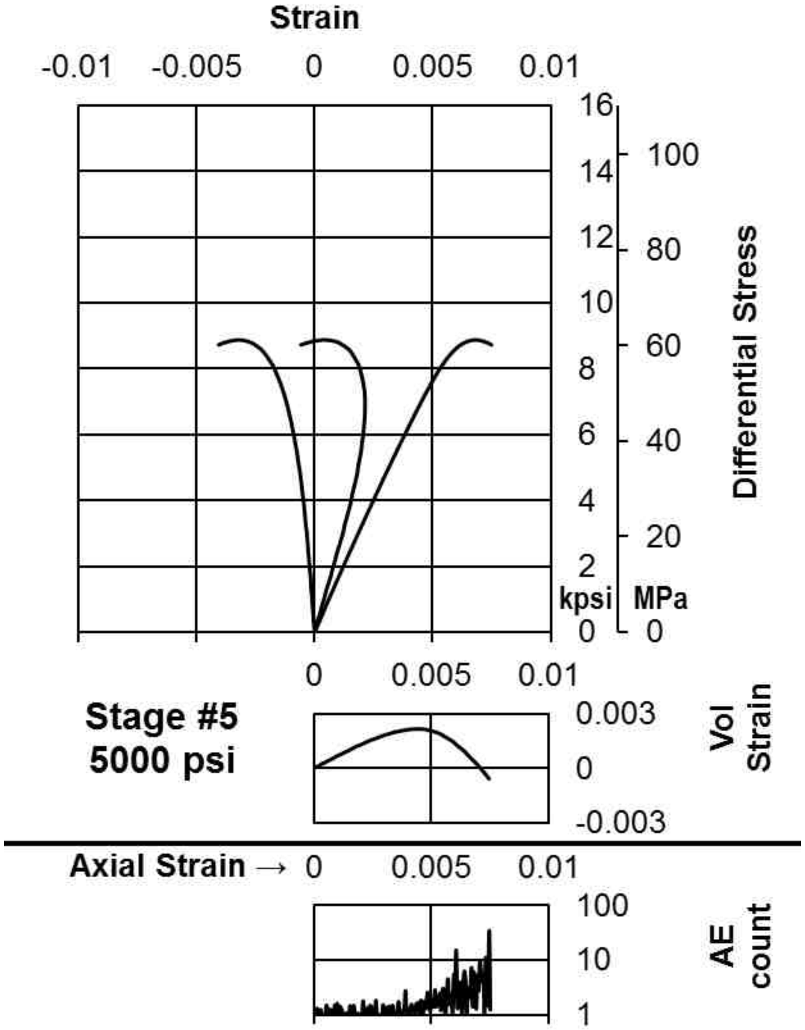

Figure AII-I.5c Stress-strain curves of brine saturated Bandera Sandstone (Stage 5)

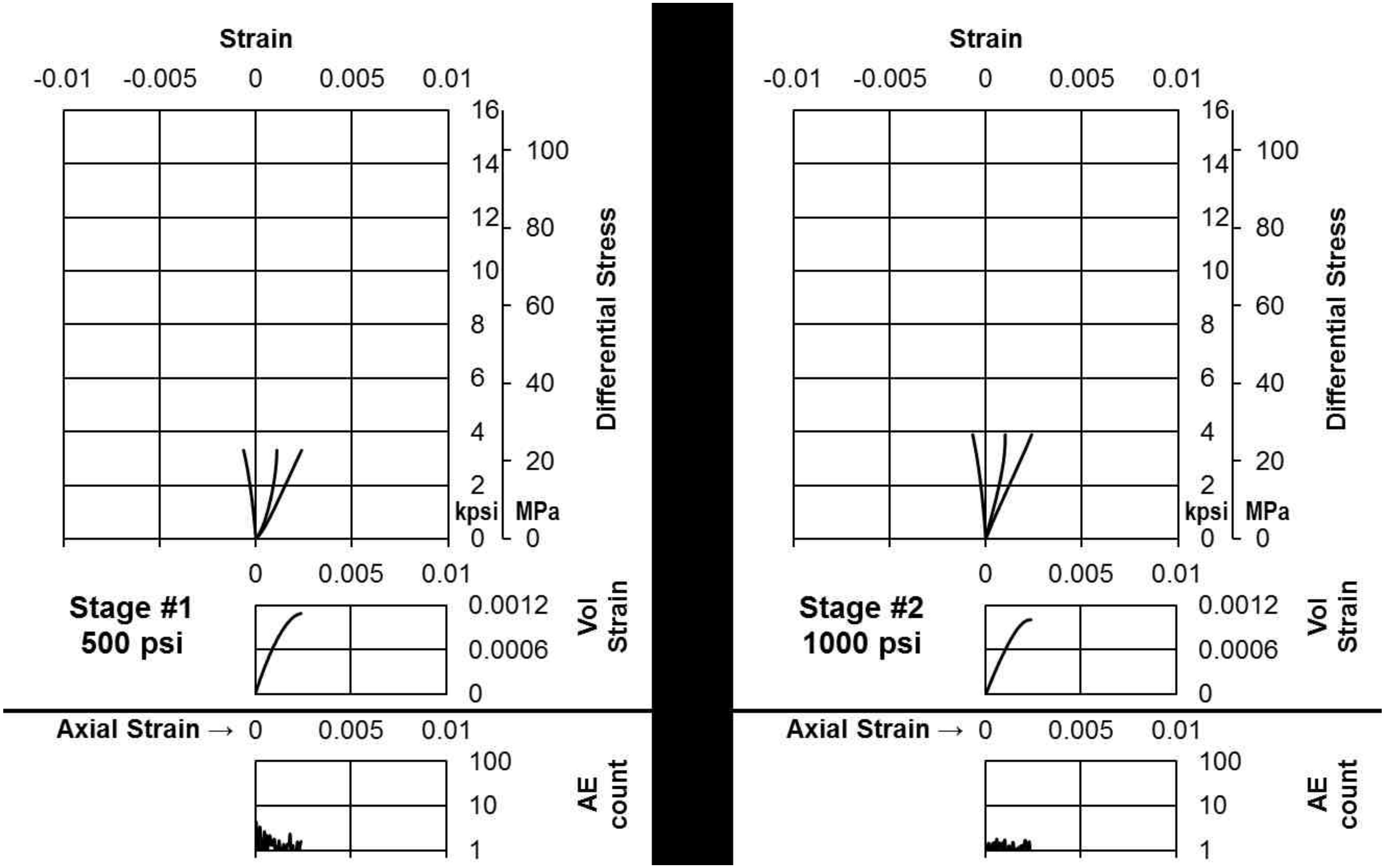

Figure AII-I.6a Stress-strain curves of dodecane saturated Bandera Sandstone (Stage 1 and 2)

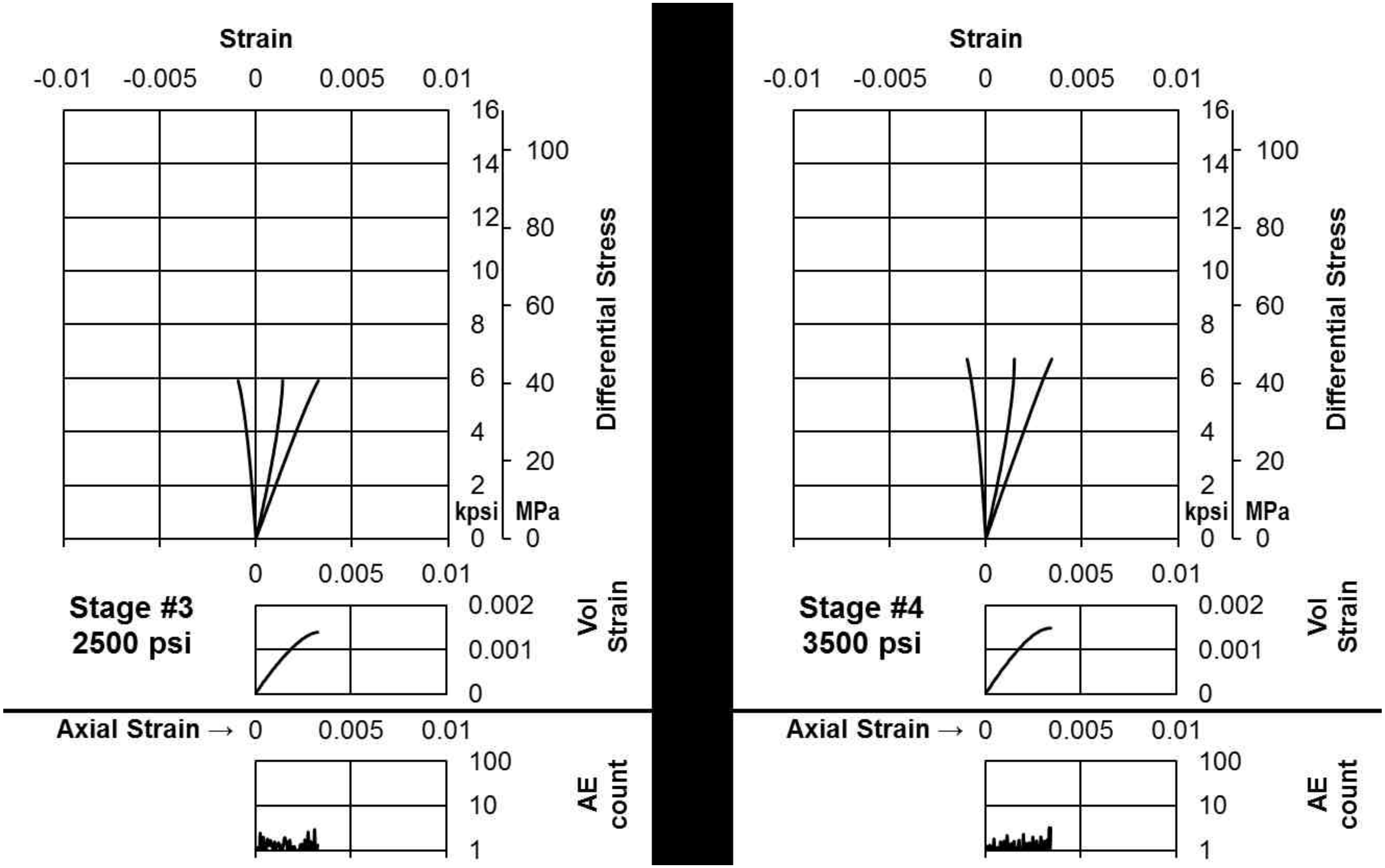

Figure AII-I.6b Stress-strain curves of dodecane saturated Bandera Sandstone (Stage 3 and 4)

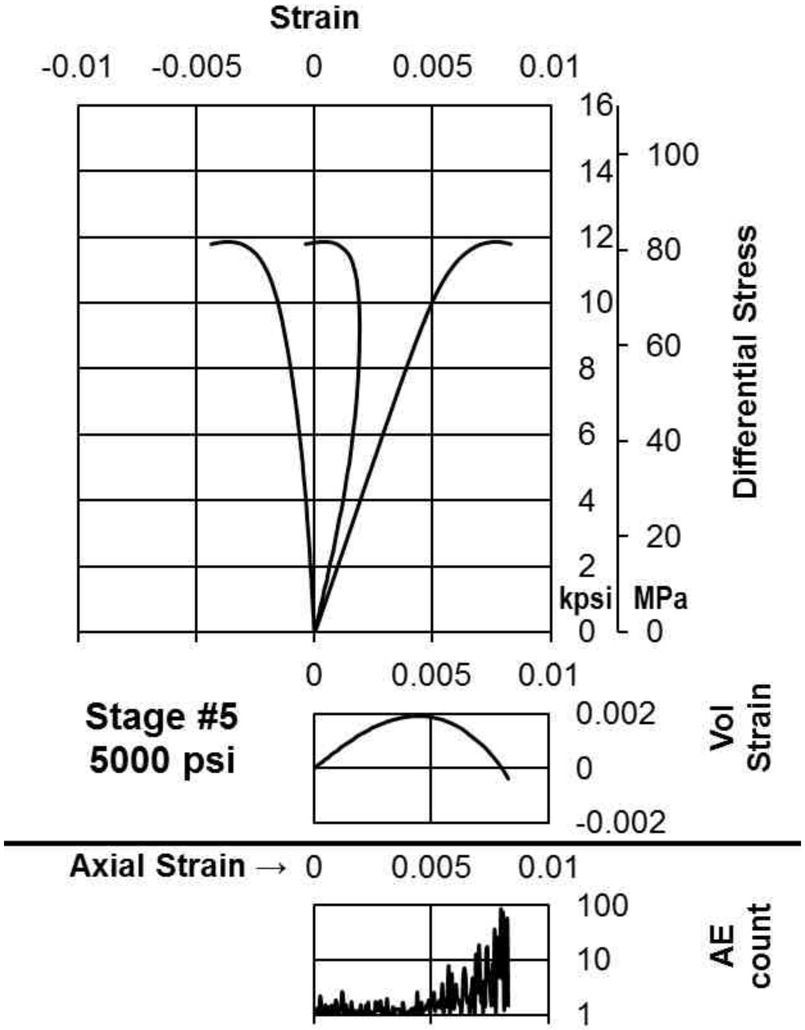

Figure AII-I.6c Stress-strain curves of dodecane saturated Bandera Sandstone (Stage 5)

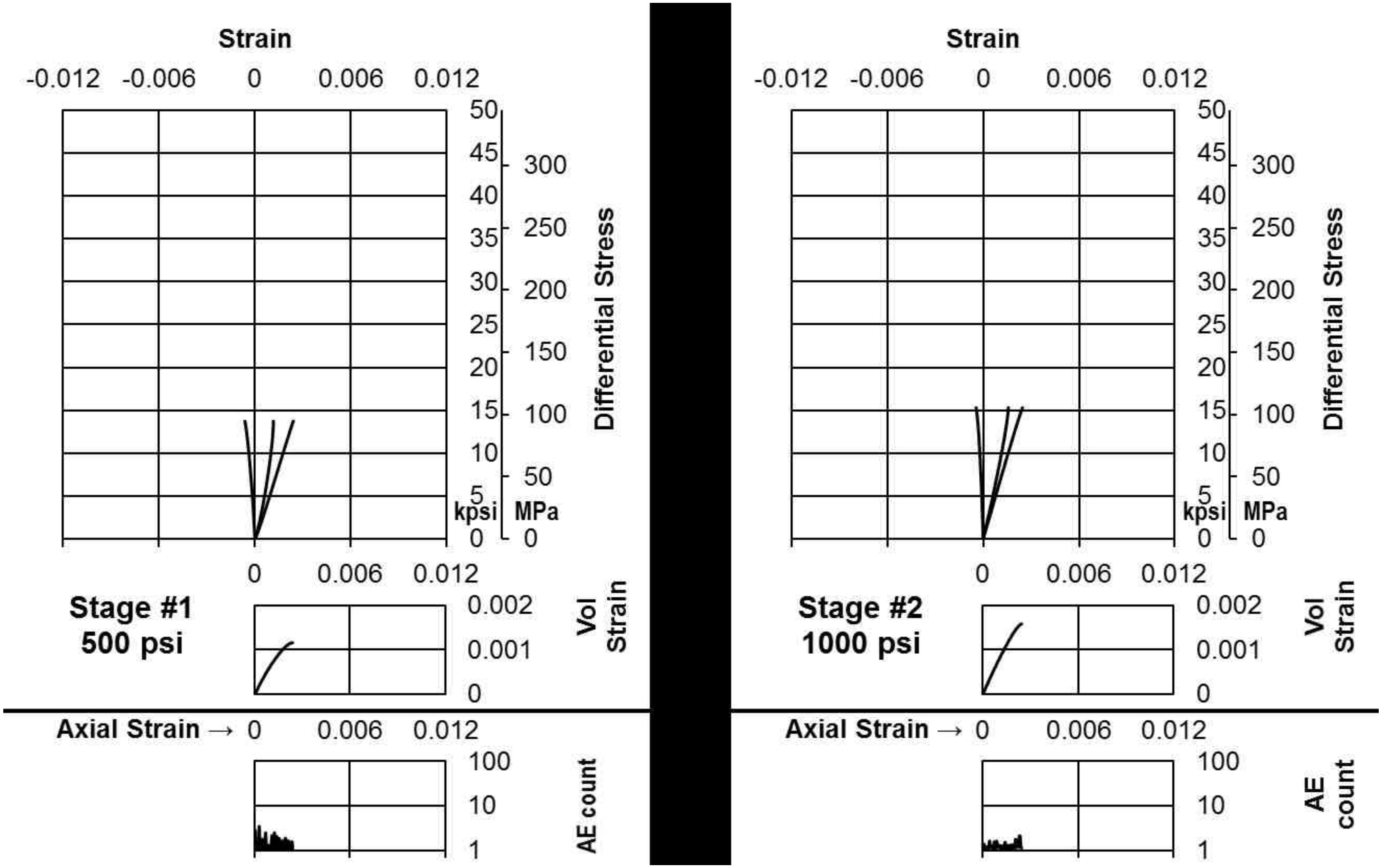

Figure AII-I.7a Stress-strain curves of room dry Lyons Sandstone (Stage 1 and 2)

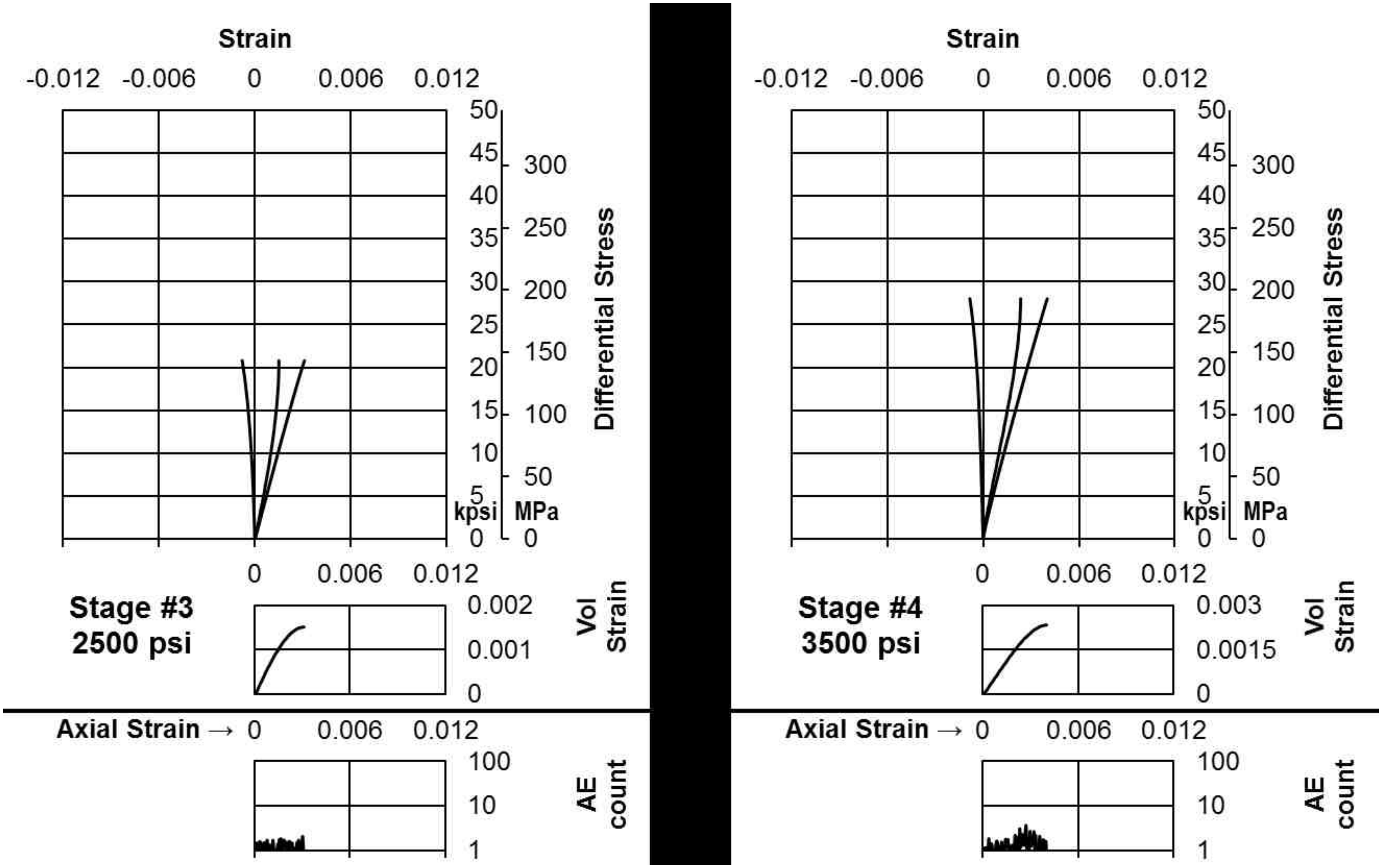

Figure AII-I.7b Stress-strain curves of room dry Lyons Sandstone (Stage 2 and 3)

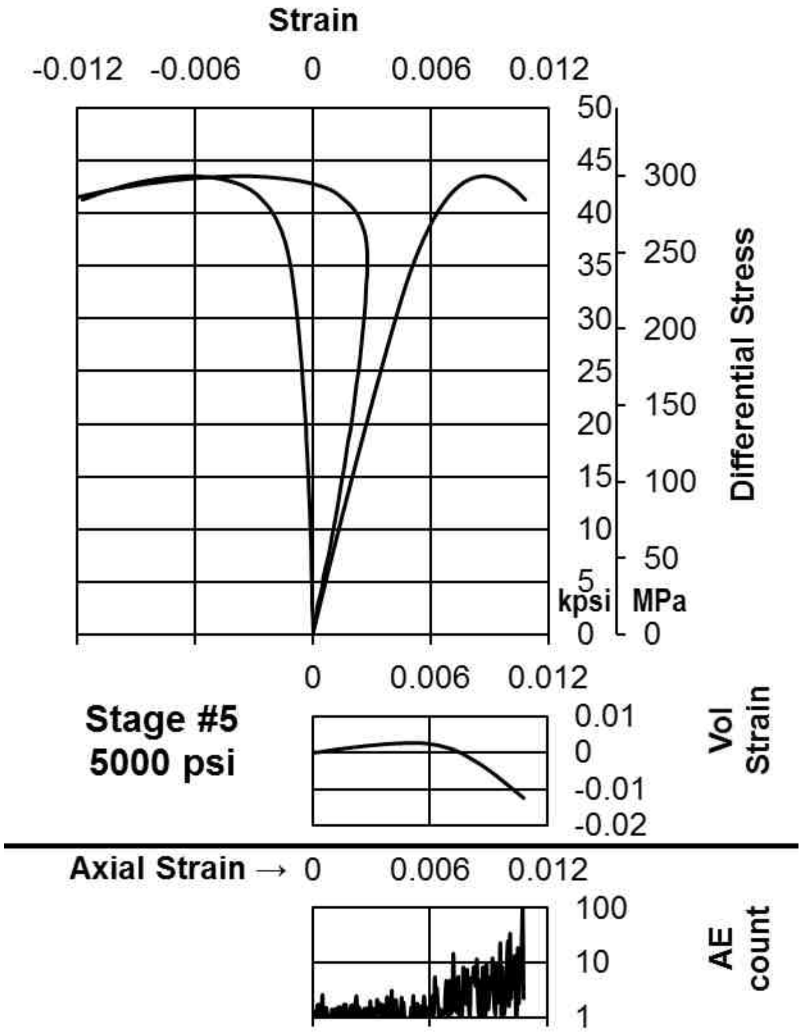

Figure AII-I.7c Stress-strain curves of room dry Lyons Sandstone (Stage 5)

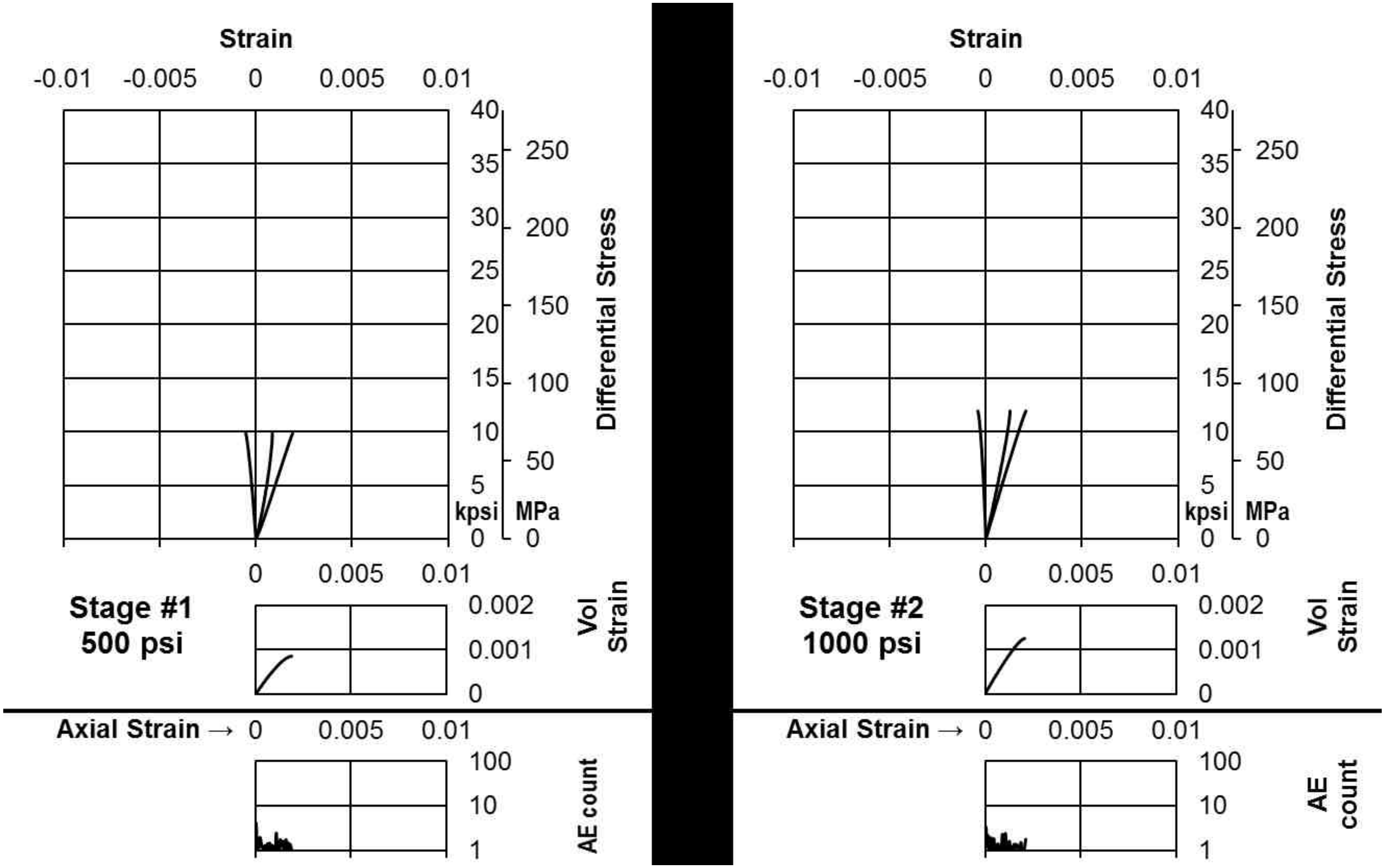

Figure AII-I.8a Stress-strain curves of brine saturated Lyons Sandstone (Stage 1 and 2)

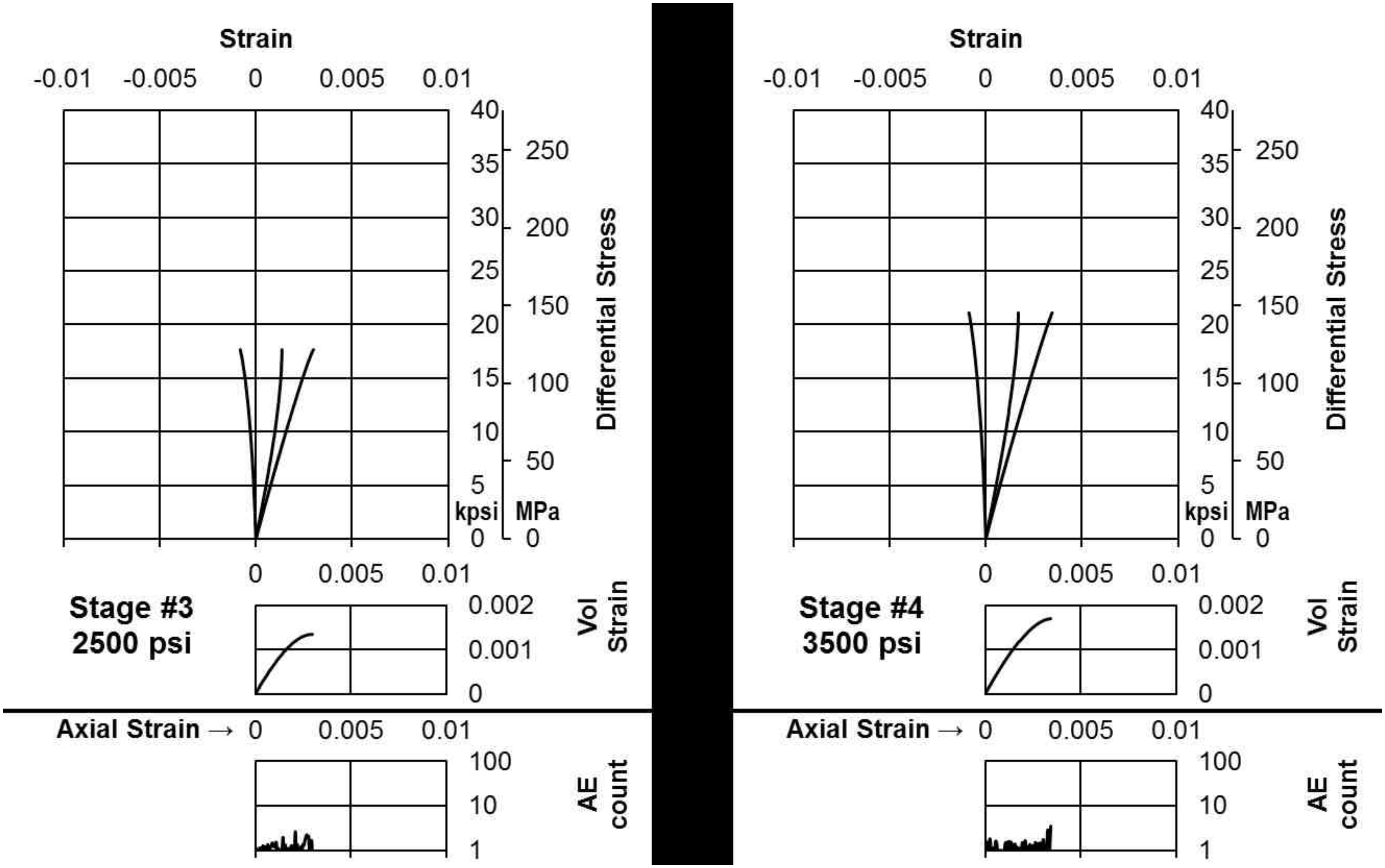

Figure AII-I.8b Stress-strain curves of brine saturated Lyons Sandstone (Stage 3 and 4)

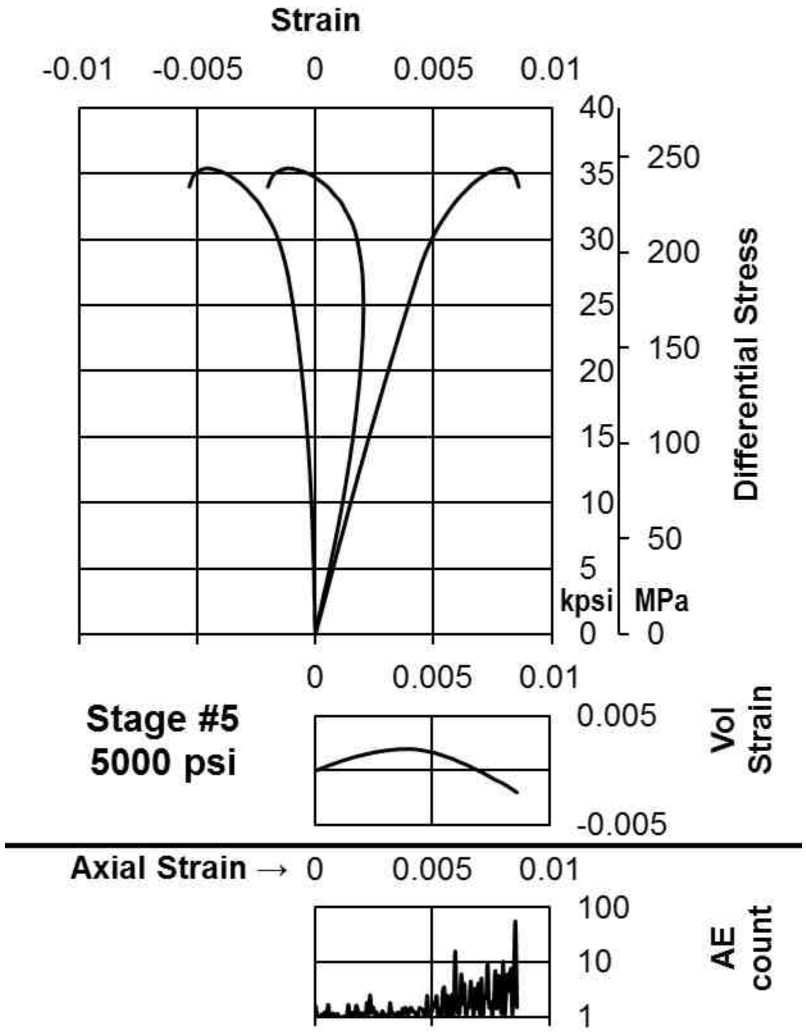

Figure AII-I.8c Stress-strain curves of brine saturated Lyons Sandstone (Stage 5)

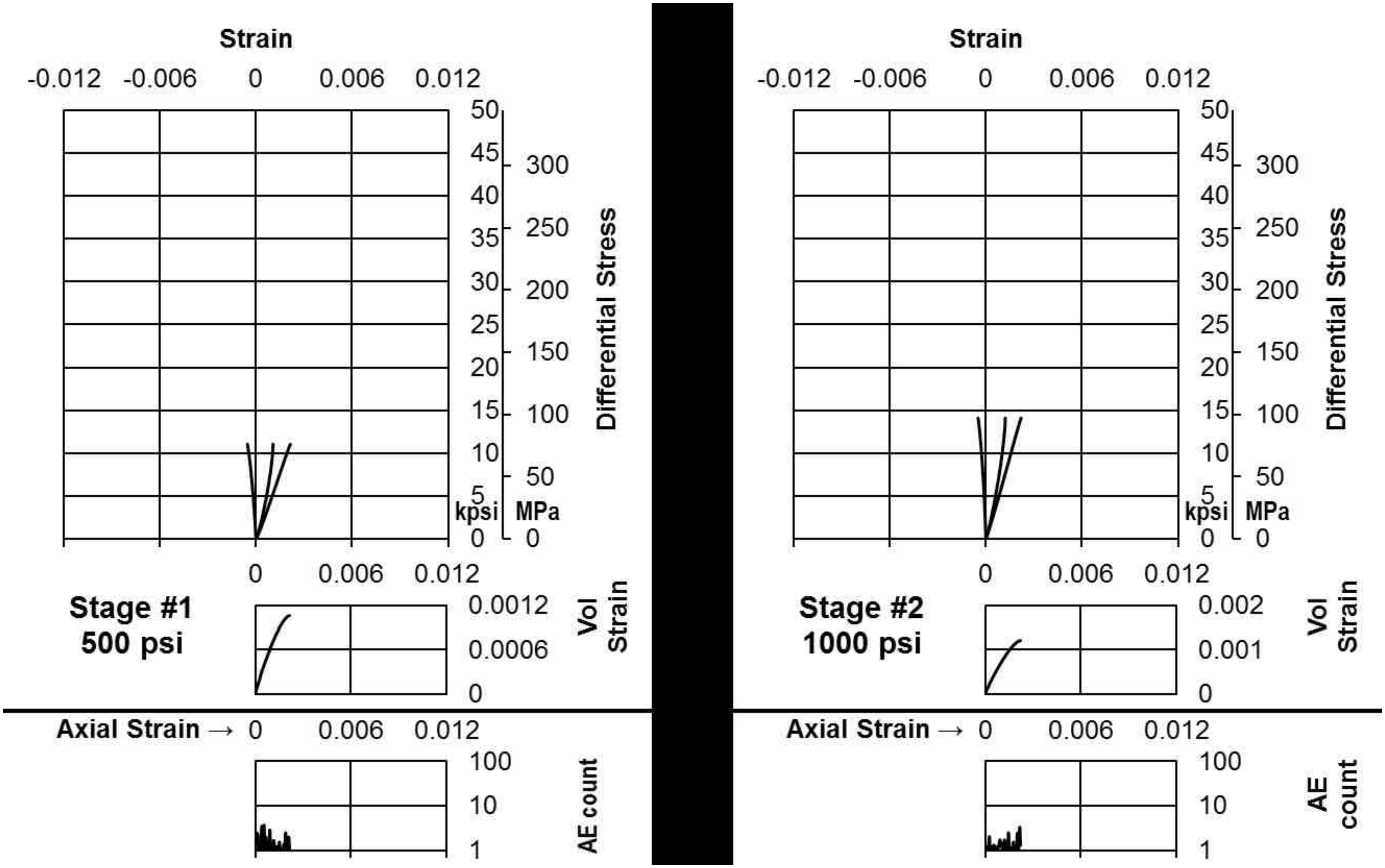

Figure AII-I.9a Stress-strain curves of dodecane saturated Lyons Sandstone (Stage 1 and 2)

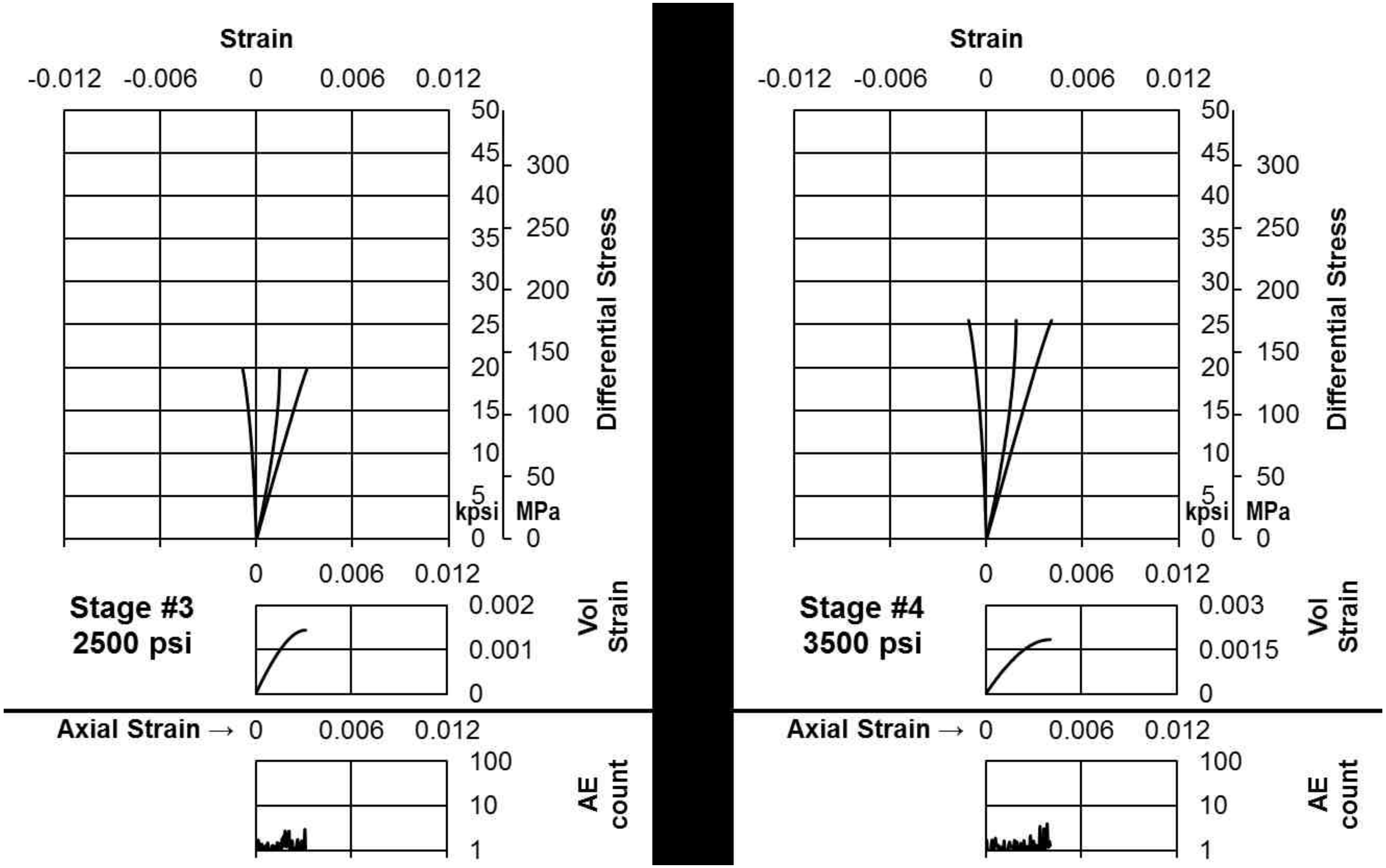

Figure AII-I.9b Stress-strain curves of dodecane saturated Lyons Sandstone (Stage 3 and 4)

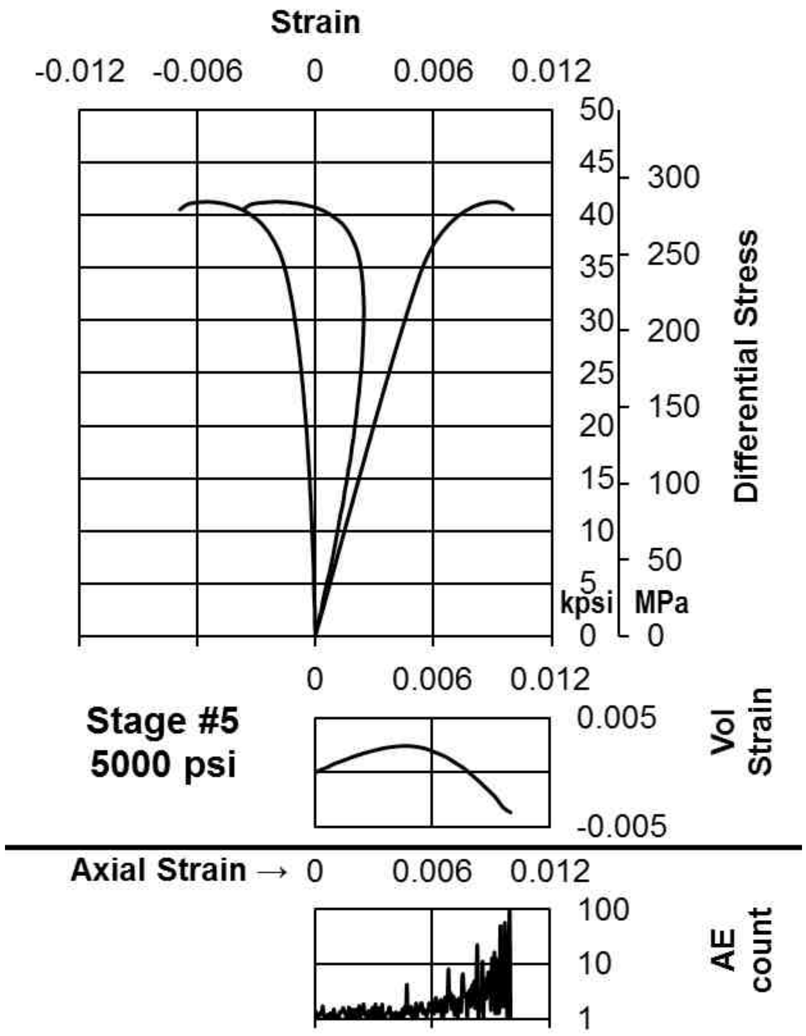

Figure AII-I.9c Stress-strain curves of dodecane saturated Lyons Sandstone (Stage 5)

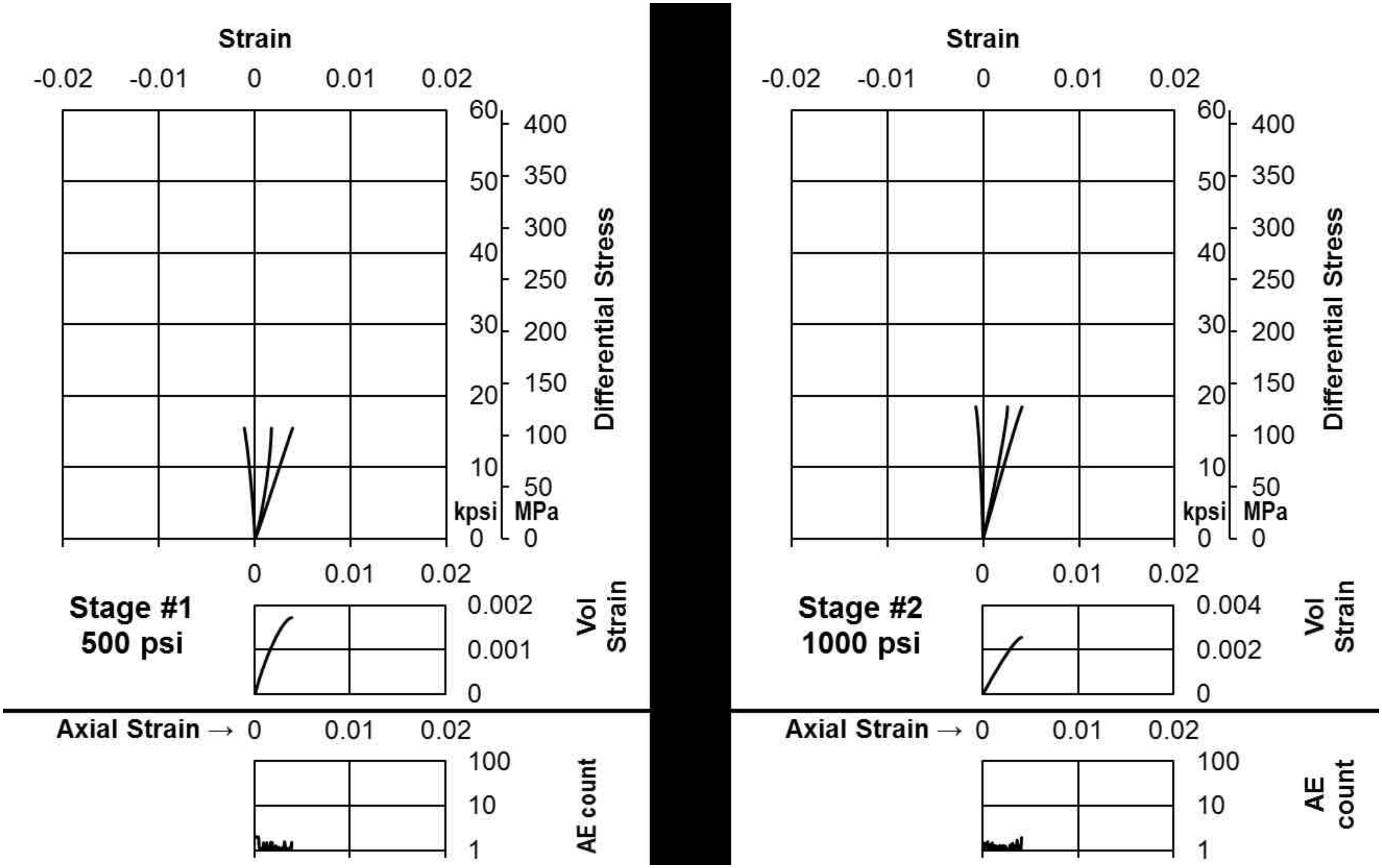

Figure AII-I.10a Stress-strain curves of room dry Tennessee Sandstone (Stage 1 and 2)

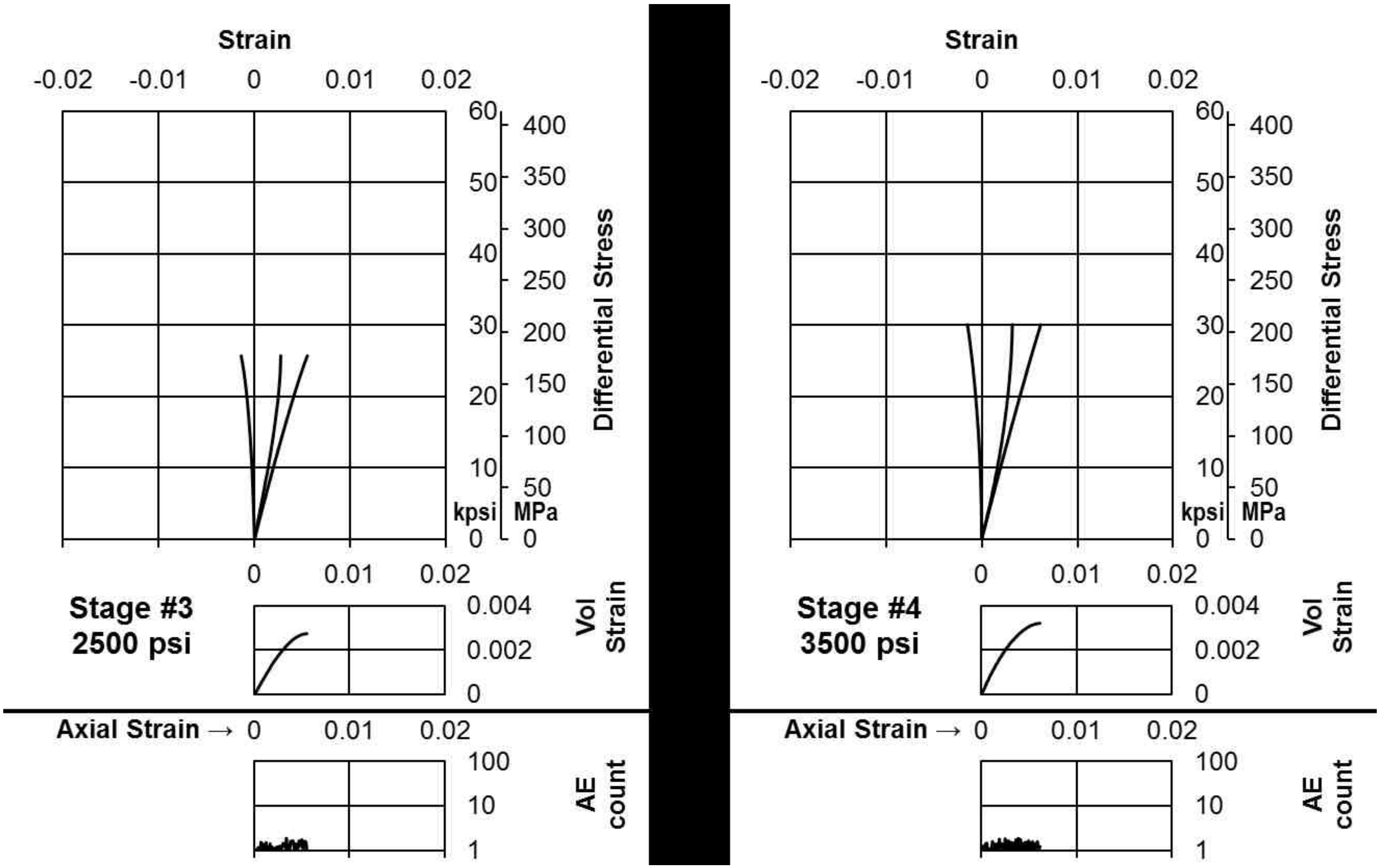

Figure AII-I.10b Stress-strain curves of room dry Tennessee Sandstone (Stage 3 and 4)

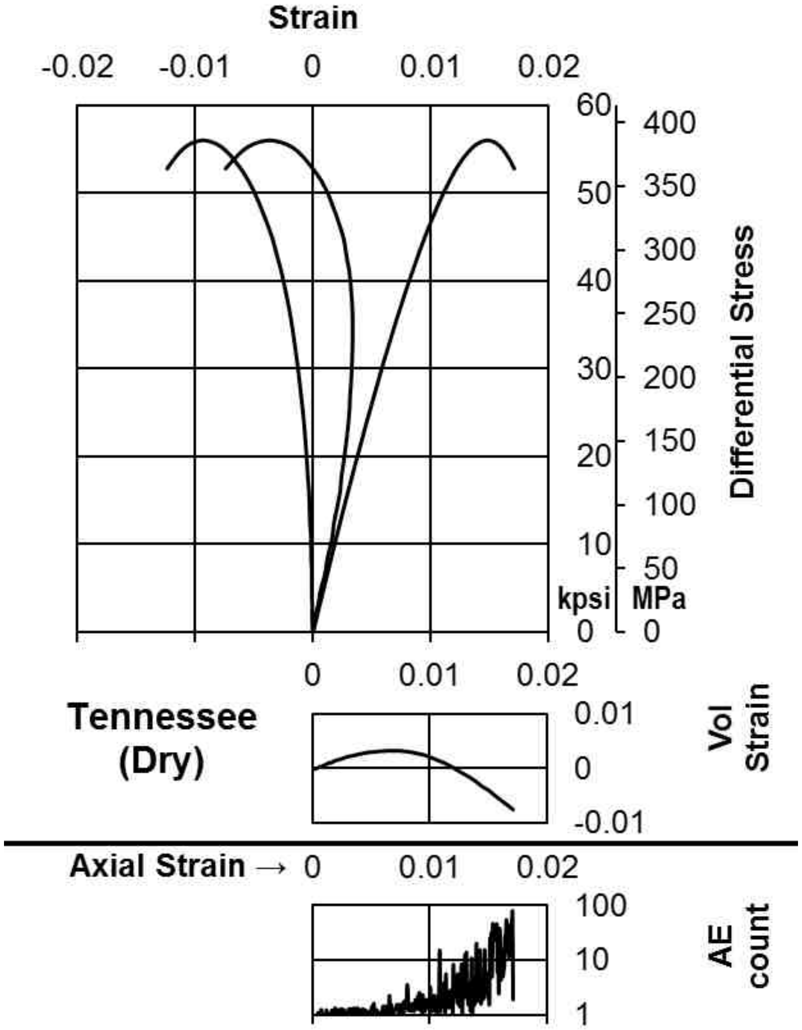

Figure AII-I.10c Stress-strain curves of room dry Tennessee Sandstone (Stage 5)

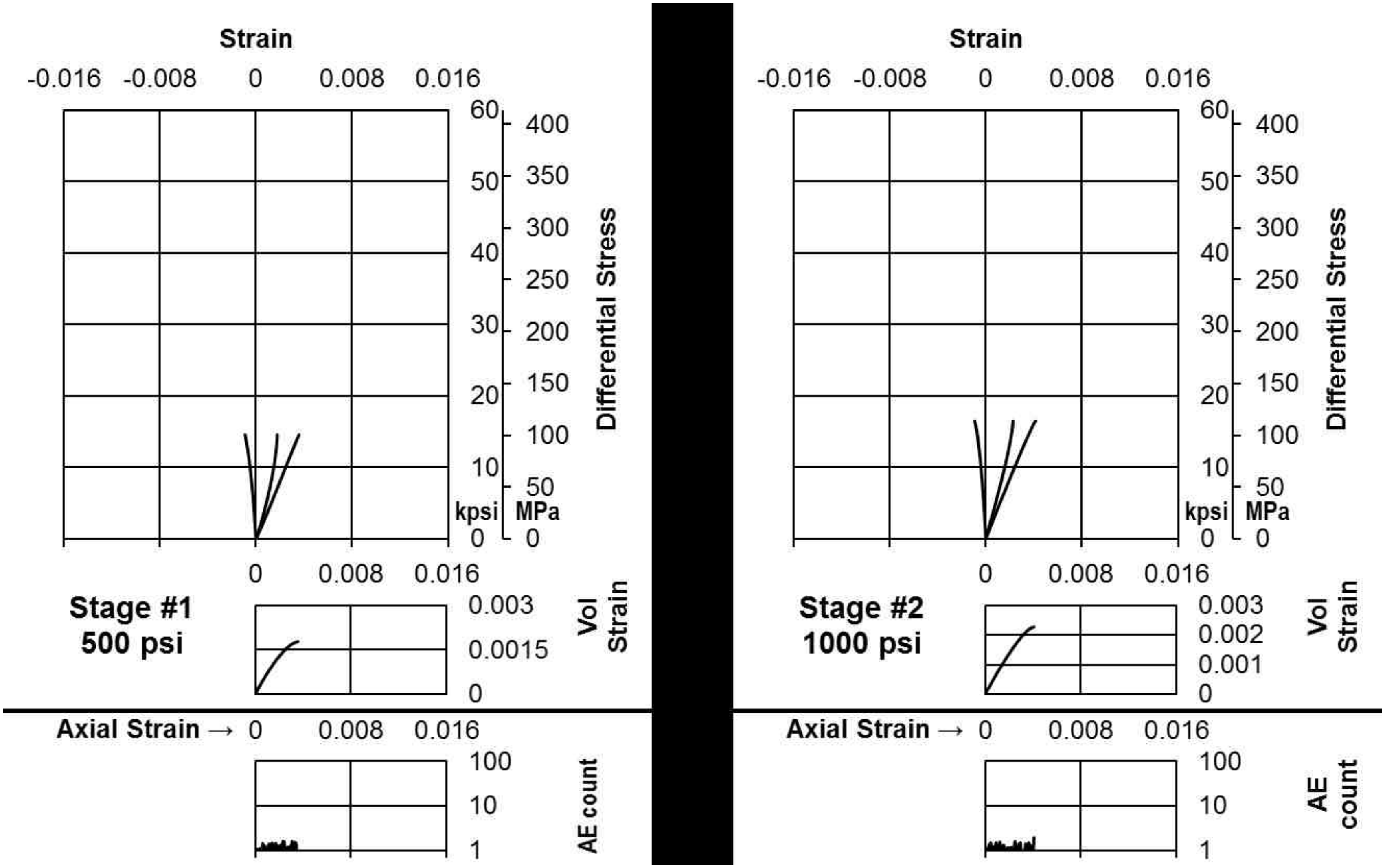

Figure AII-I.11a Stress-strain curves of brine saturated Tennessee Sandstone (Stage 1 and 2)

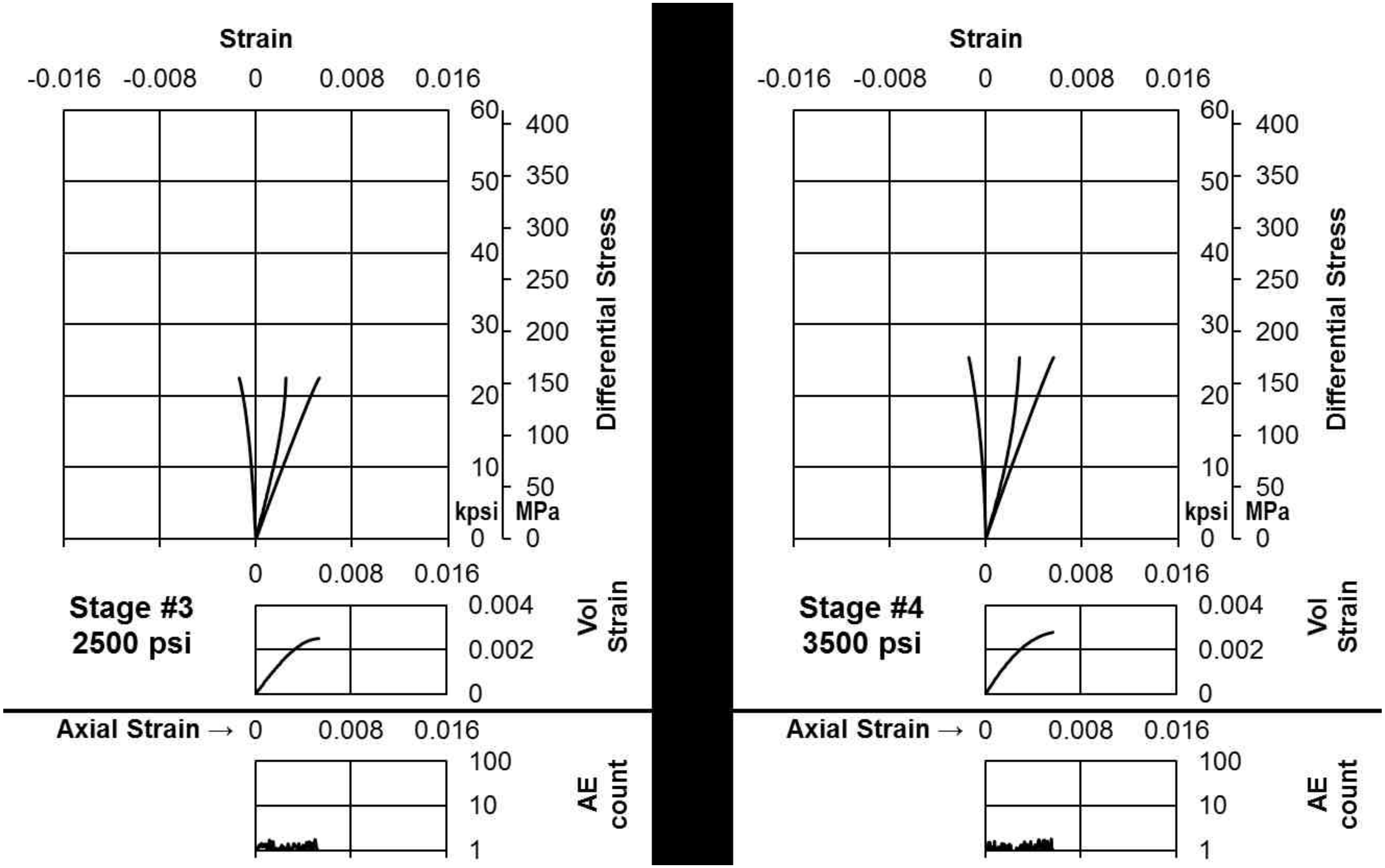

Figure AII-I.11b Stress-strain curves of brine saturated Tennessee Sandstone (Stage 3 and 4)

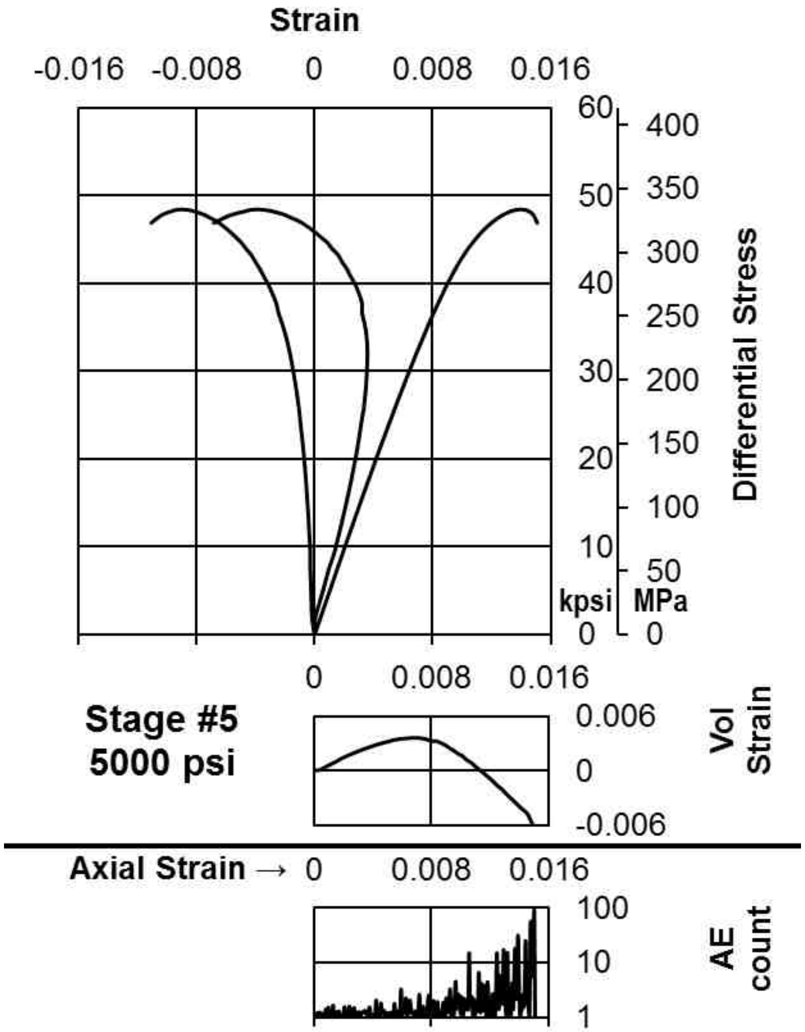

Figure AII-I.11c Stress-strain curves of brine saturated Tennessee Sandstone (Stage 5)

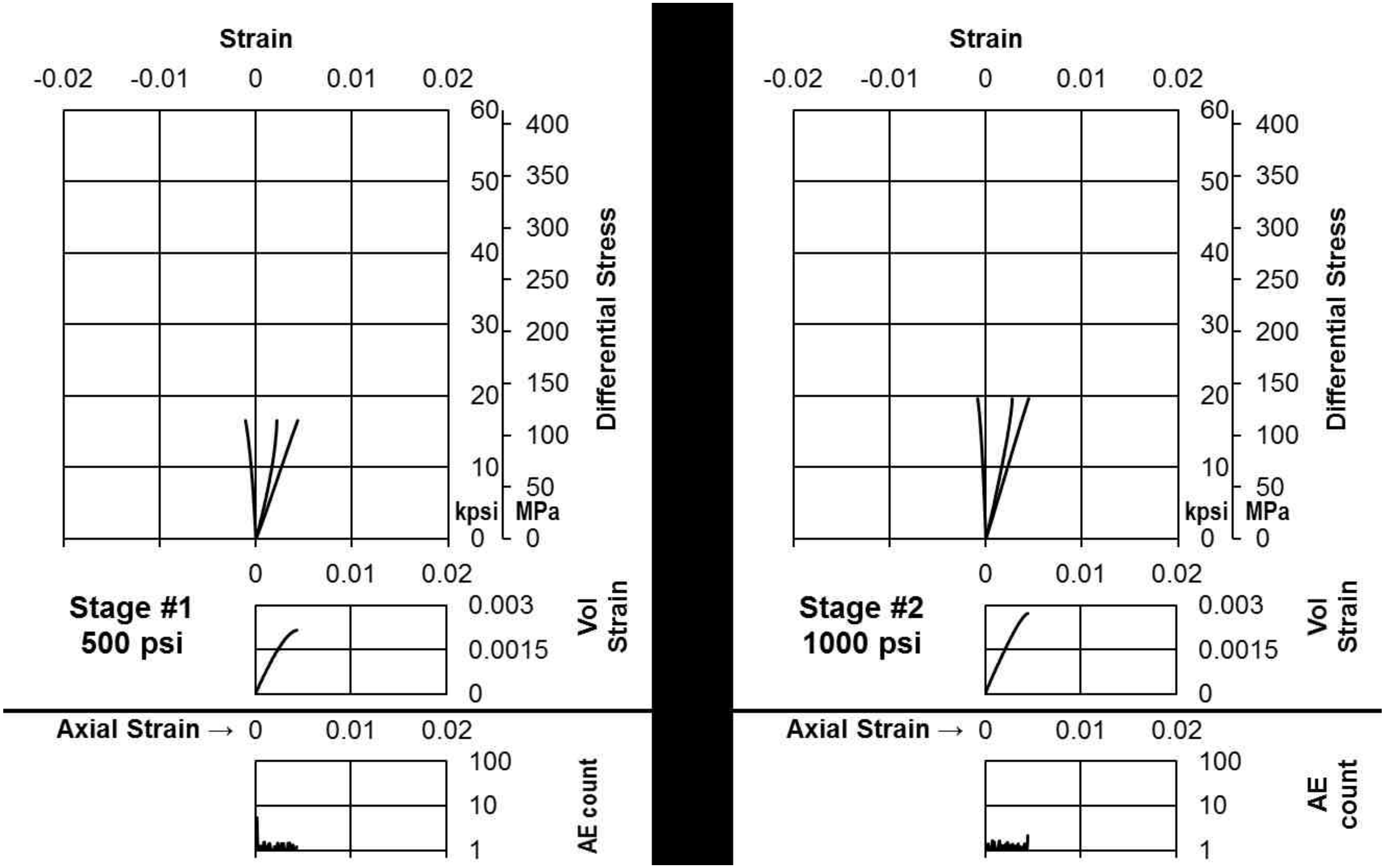

Figure AII-I.12a Stress-strain curves of dodecane saturated Tennessee Sandstone (Stage 1 and 2)

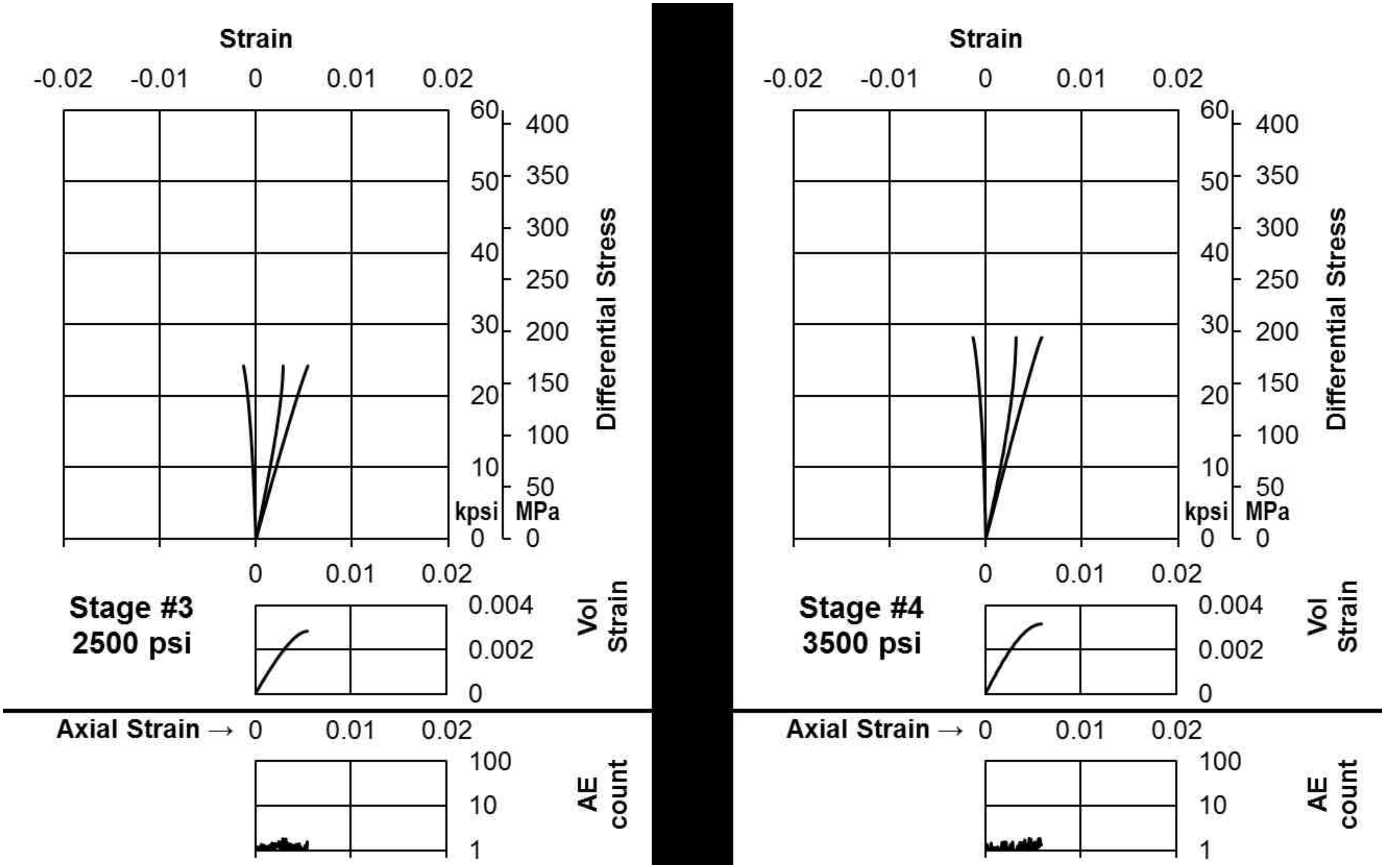

Figure AII-I.12b Stress-strain curves of dodecane saturated Tennessee Sandstone (Stage 3 and 4)

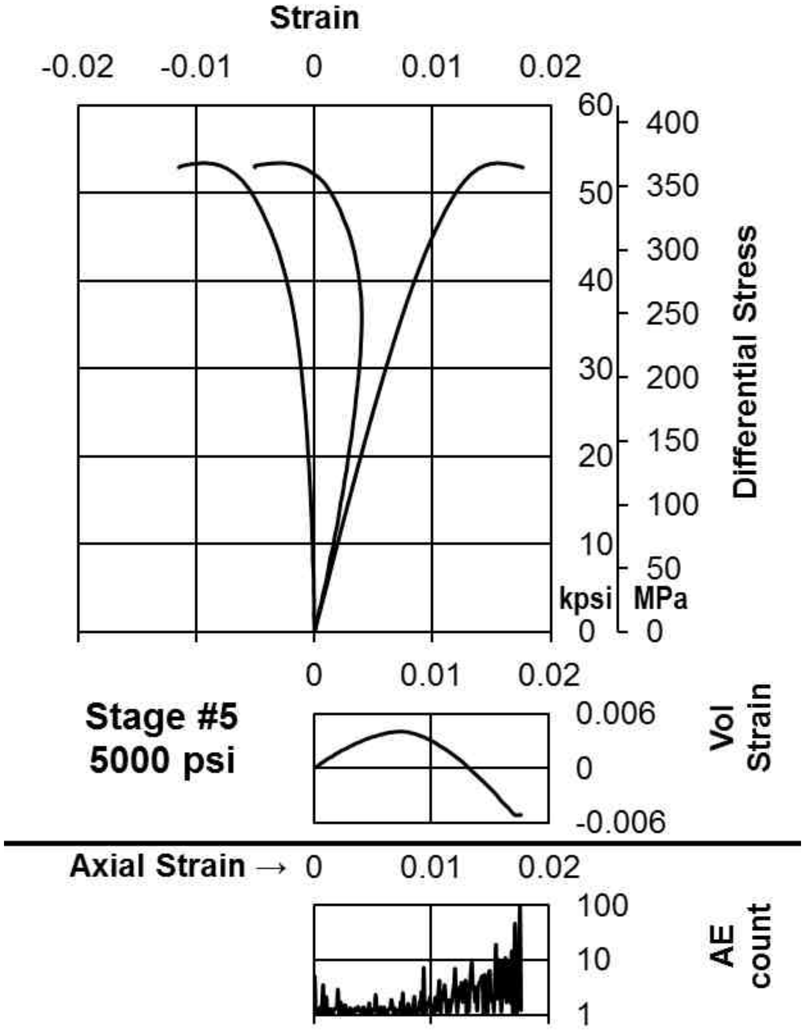

Figure AII-I.12c Stress-strain curves of dodecane saturated Tennessee Sandstone (Stage 5)

Appendix II-II: Stress-Strain Curves and AE Counts (Shales)

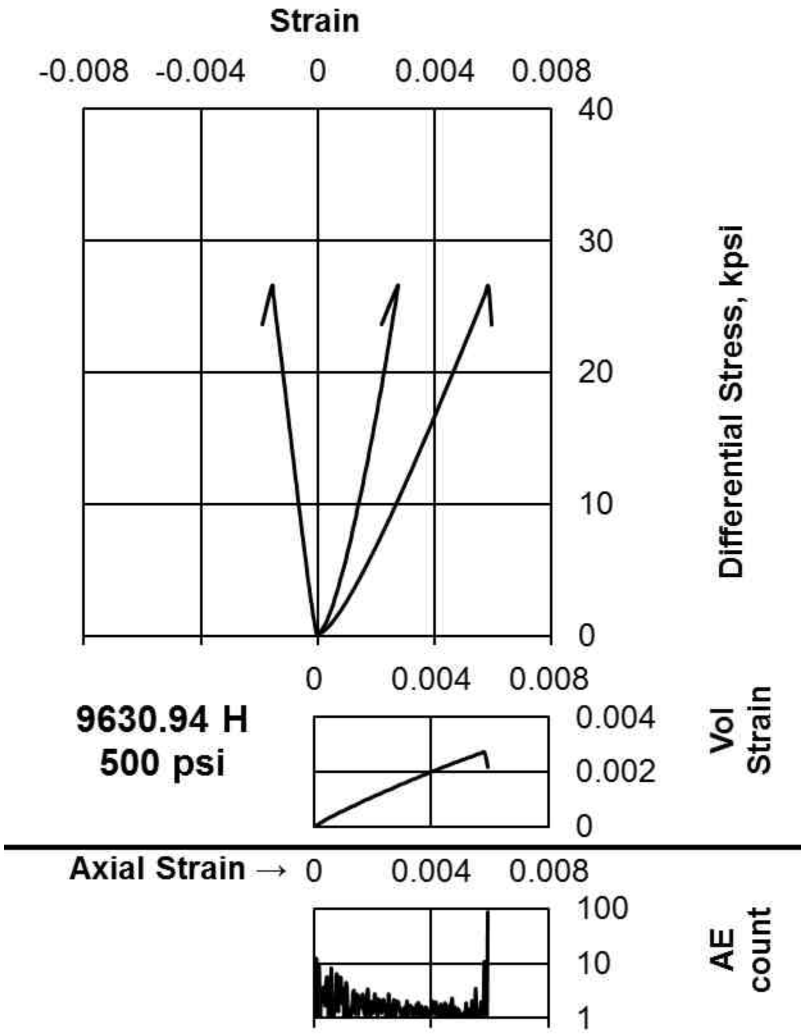

Figure AII-II.1a Stress-strain curves of Woodford 9630.94’ (Single stage)

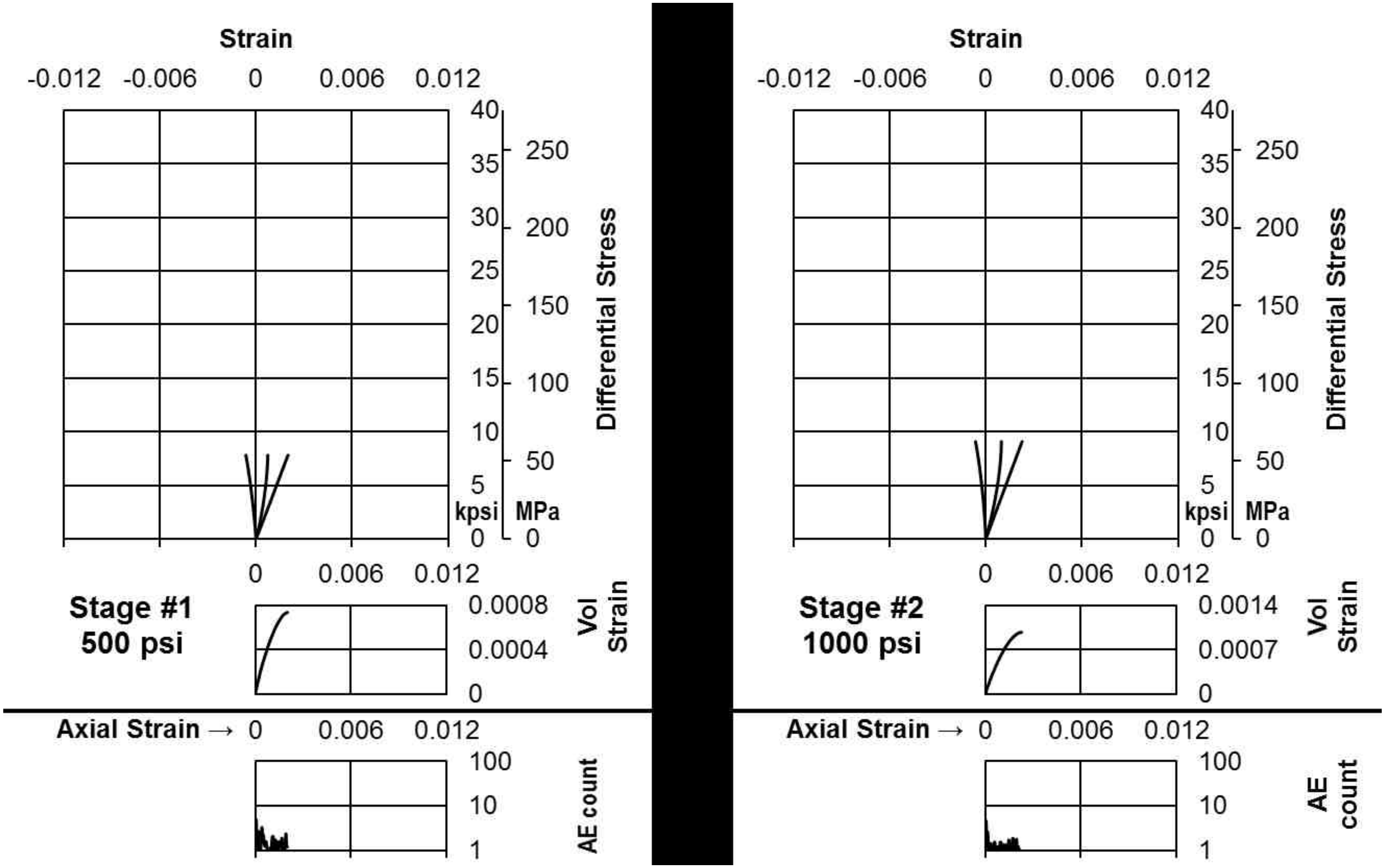

Figure AII-II.2a Stress-strain curves of Woodford 9654.29’ (Stage 1 and 2)

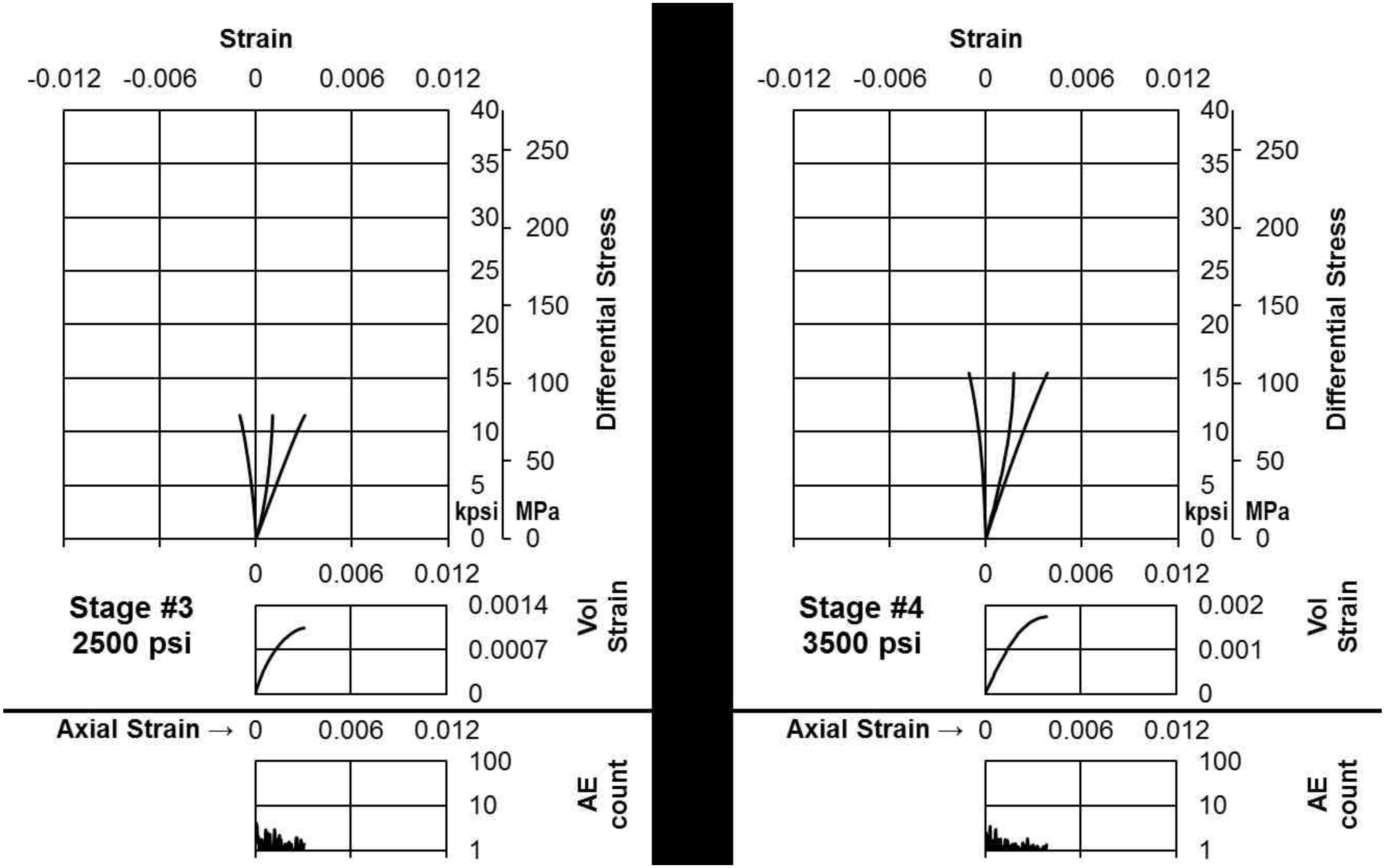

Figure AII-II.2b Stress-strain curves of Woodford 9654.29’ (Stage 3 and 4)

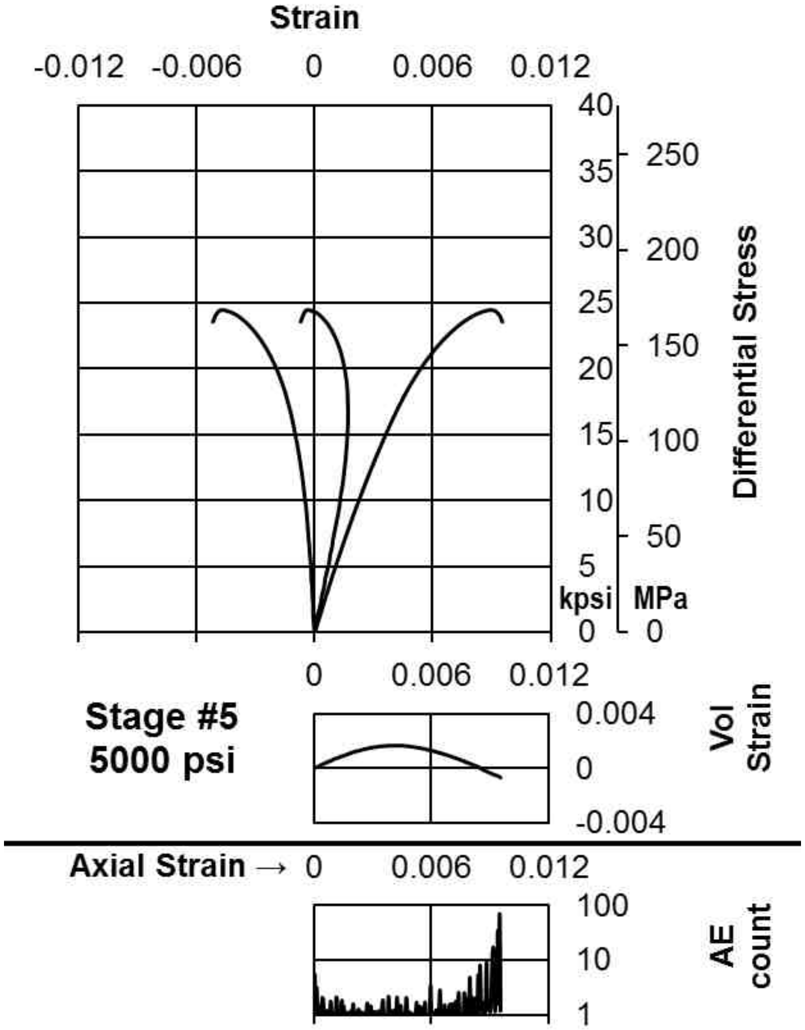

Figure AII-II.2c Stress-strain curves of Woodford 9654.29’ (Stage 5)

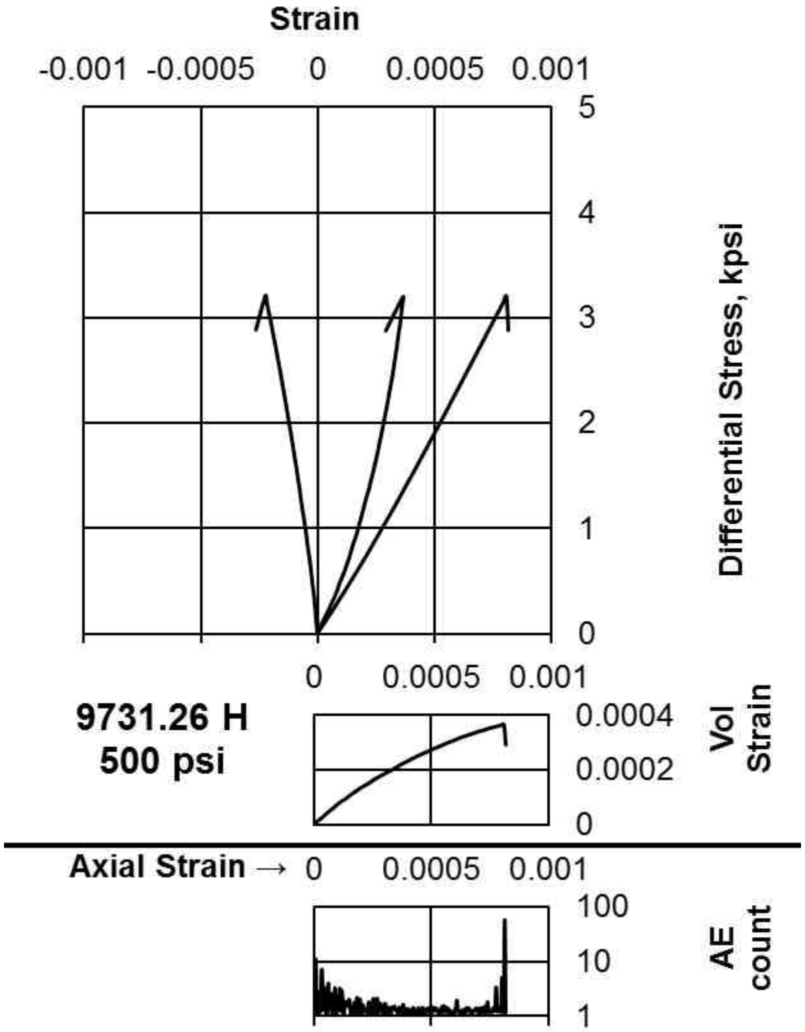

Figure AII-II.3a Stress-strain curves of Woodford 9731.26' (Single stage)

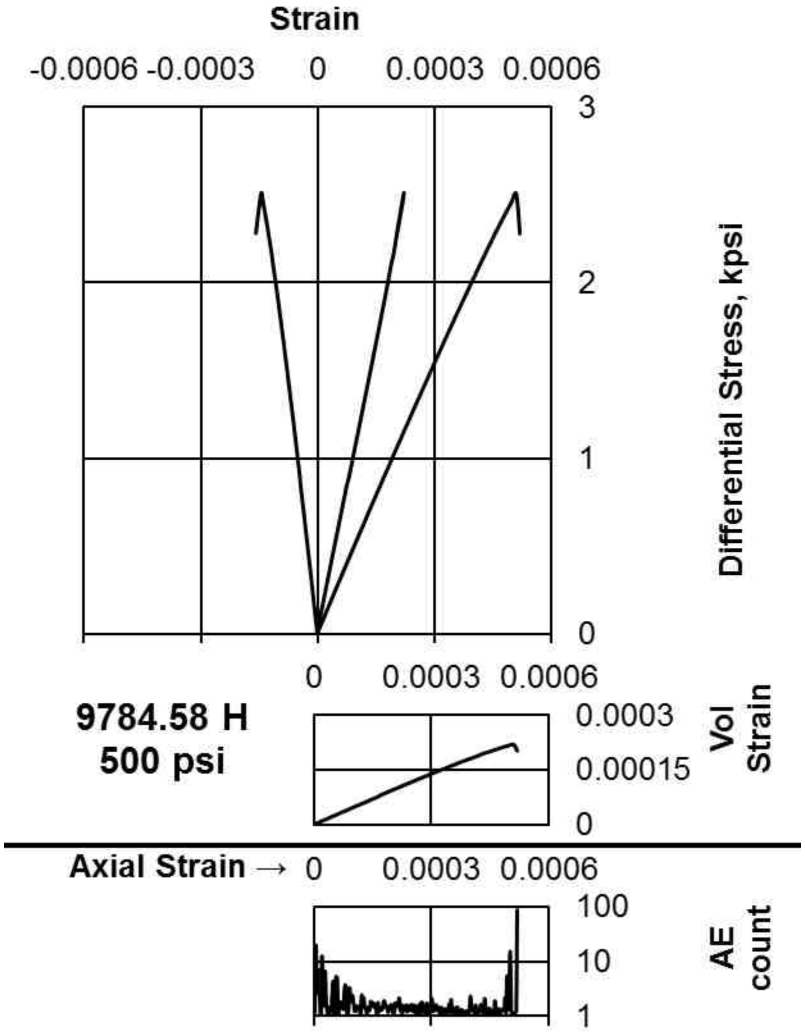

Figure AII-II.4a Stress-strain curves of Woodford 9784.58’ (Single stage)

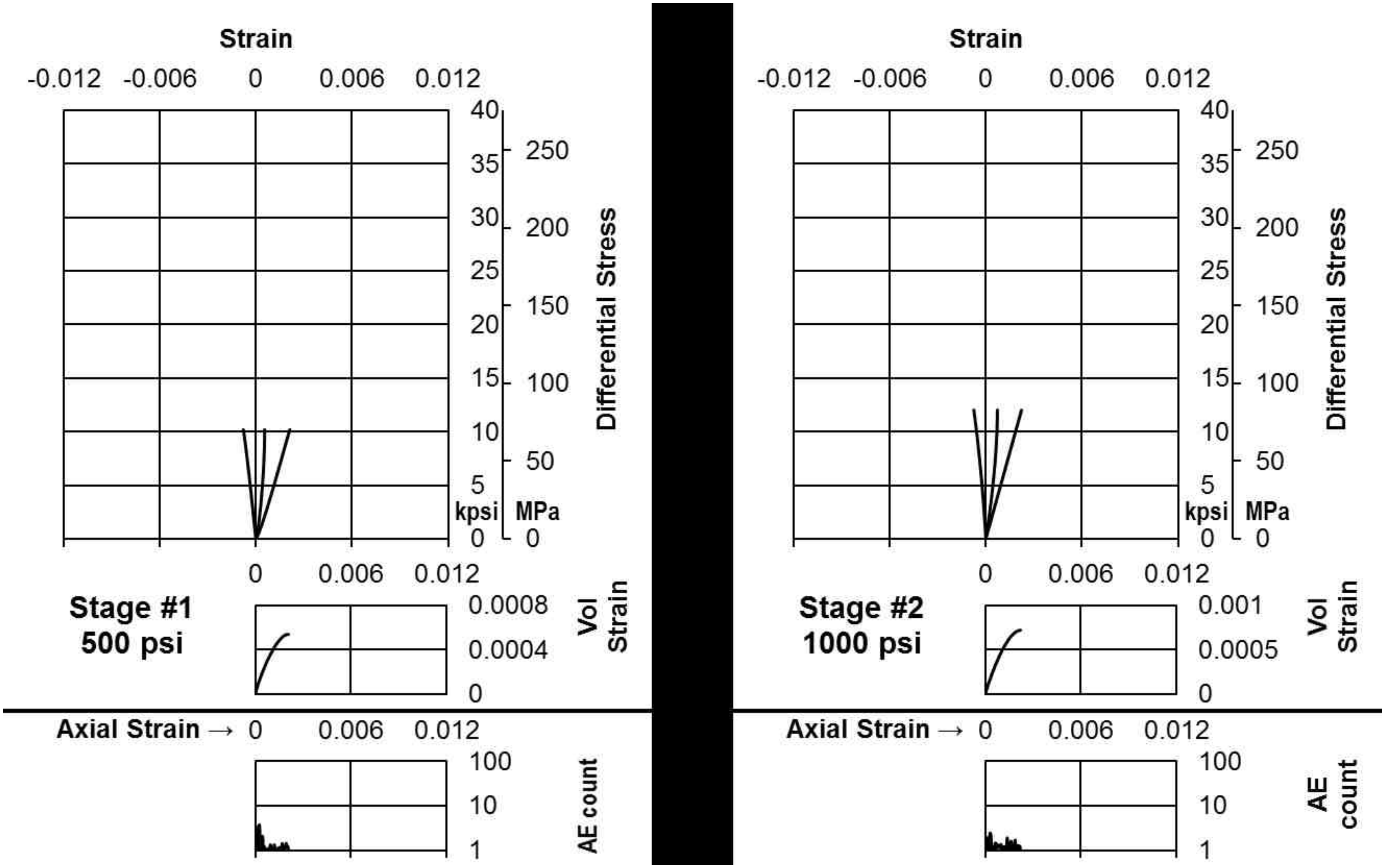

Figure AII-II.5a Stress-strain curves of Eagle Ford 11094.89' (Stage 1 and 2)

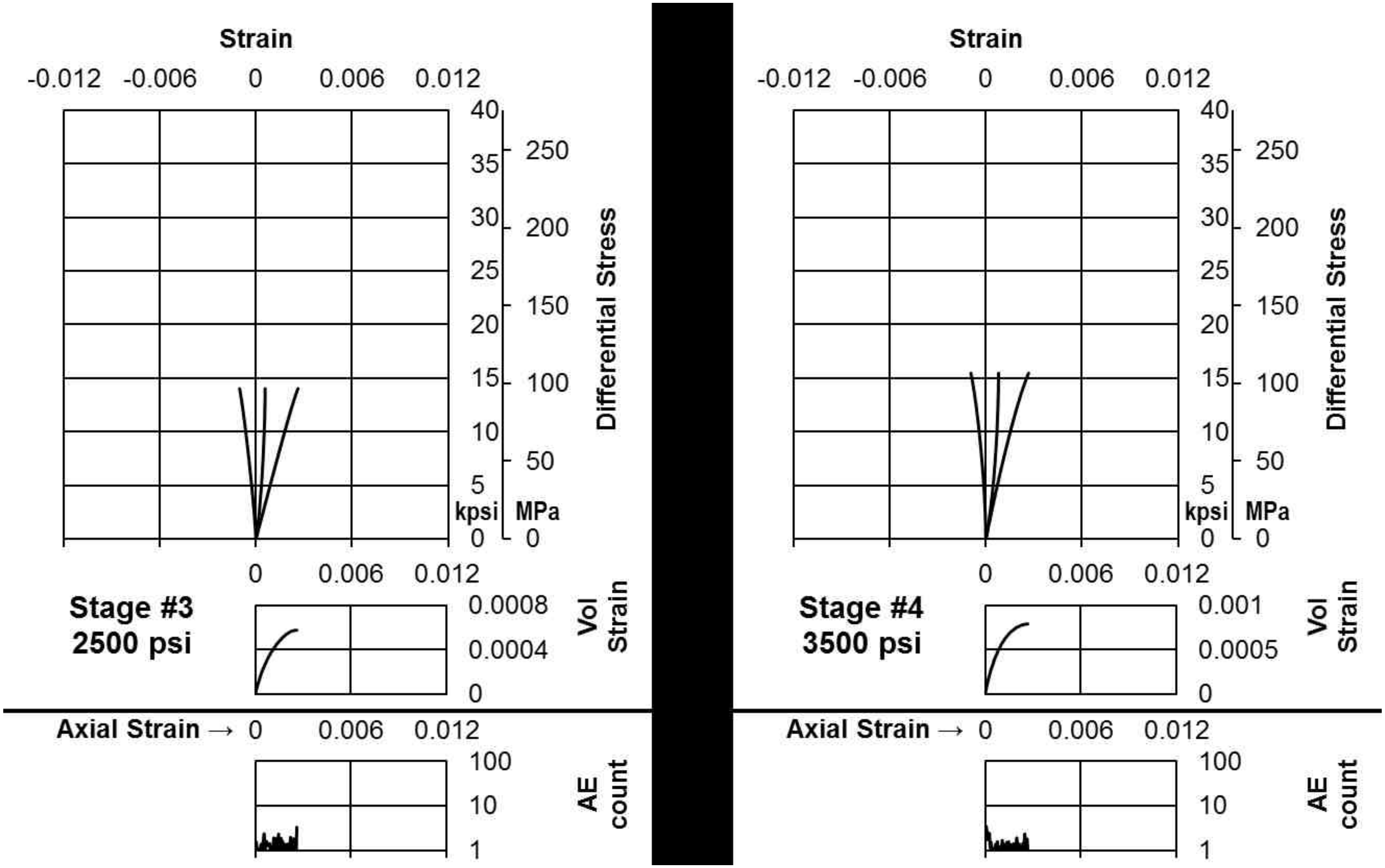

Figure AII-II.5b Stress-strain curves of Eagle Ford 11094.89' (Stage 3 and 4)

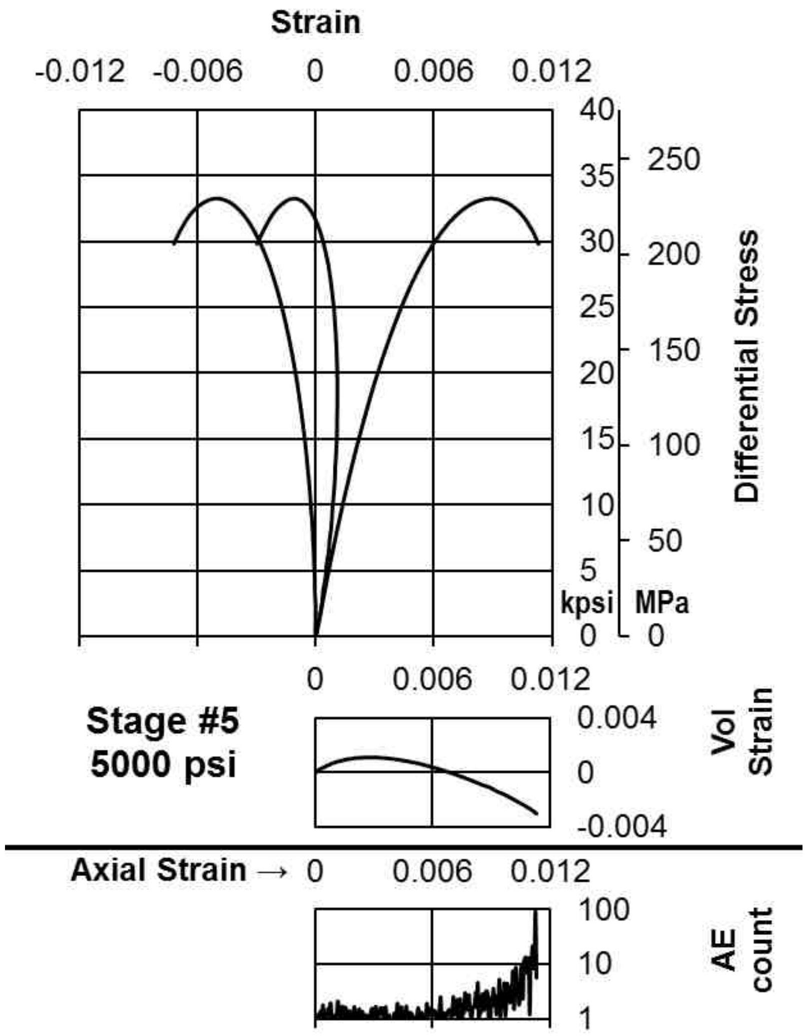

Figure AII-II.5c Stress-strain curves of Eagle Ford 11094.89’ (Stage 5)

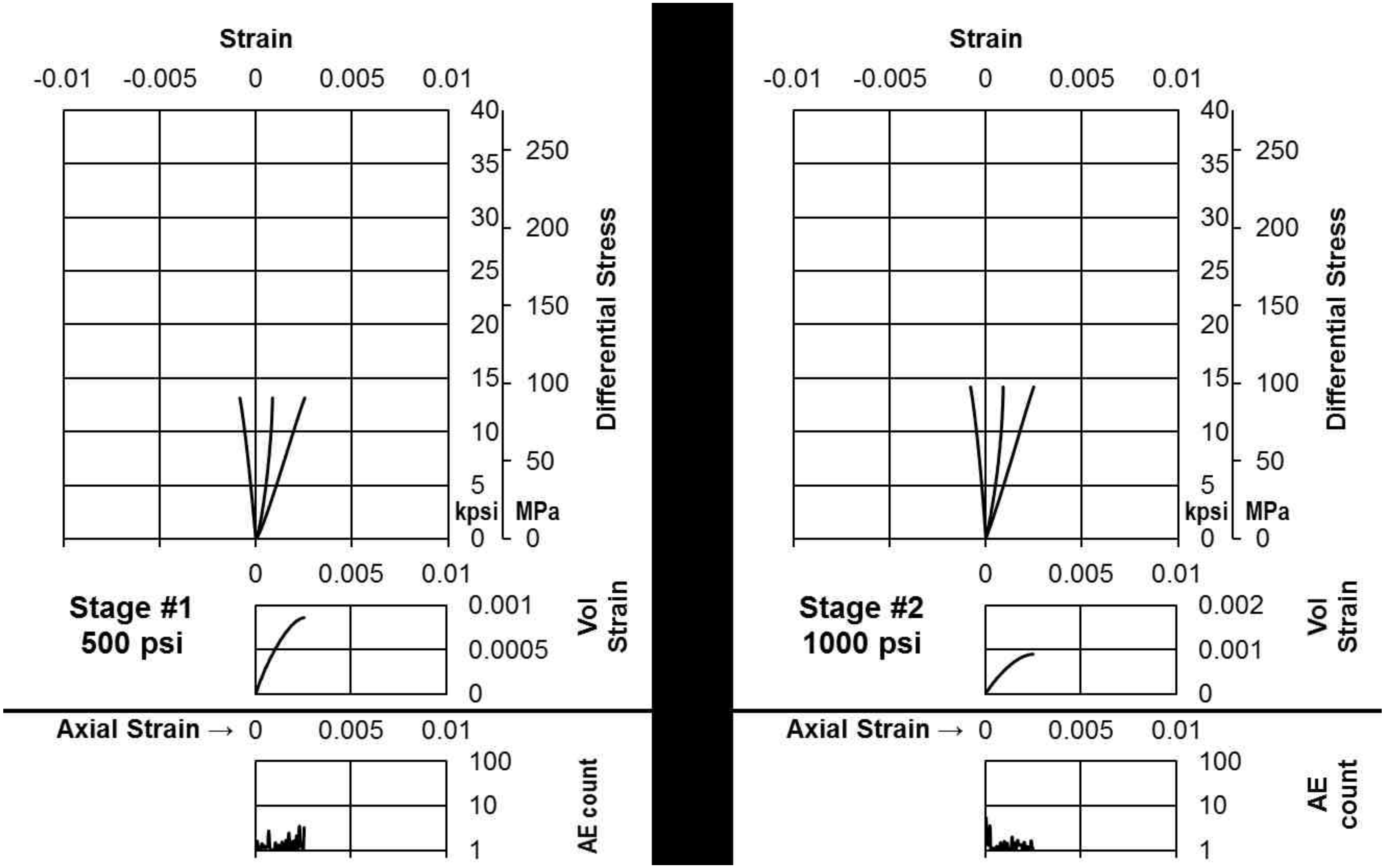

Figure AII-II.6a Stress-strain curves of Eagle Ford 11115.35’ (Stage 1 and 2)

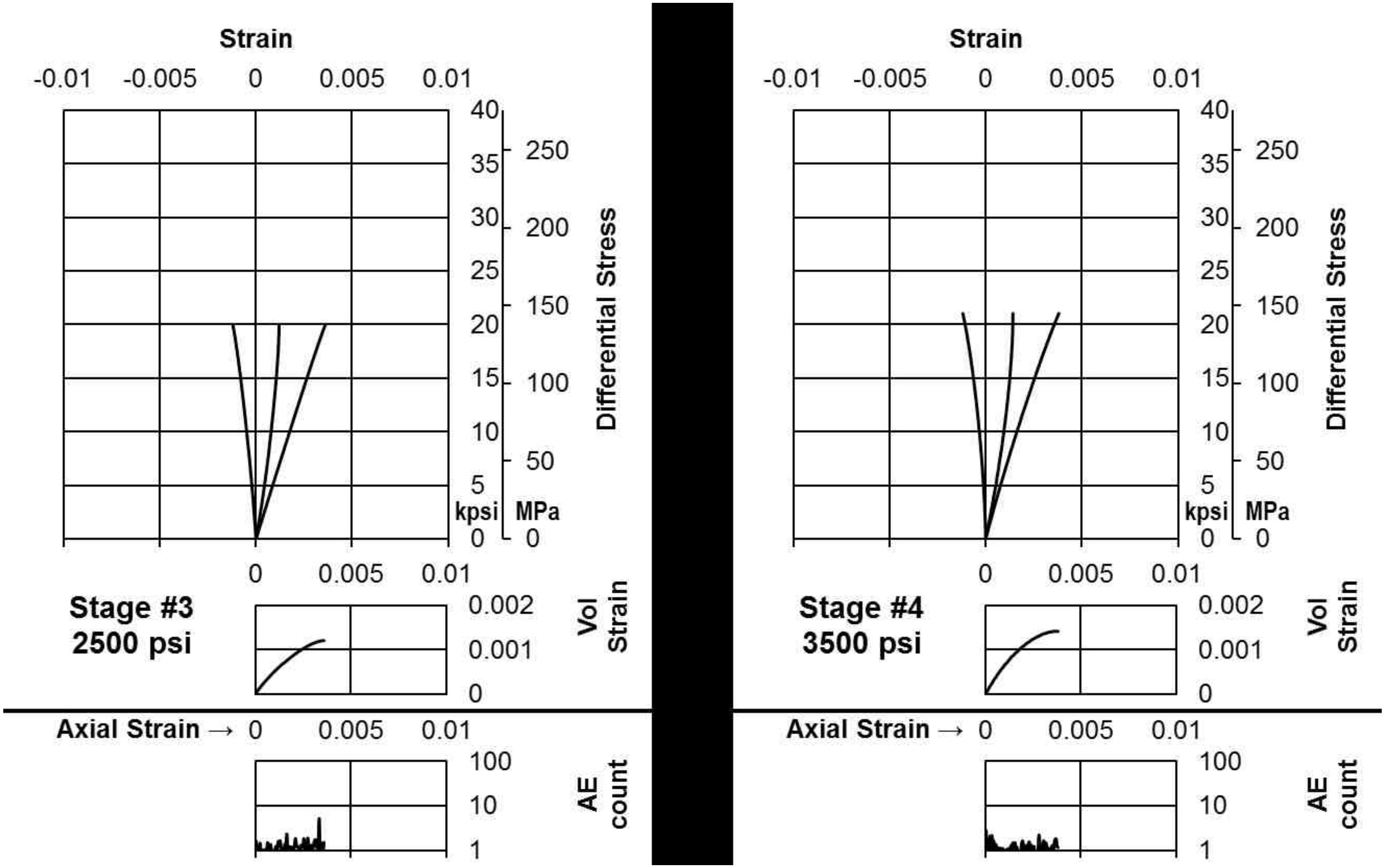

Figure AII-II.6b Stress-strain curves of Eagle Ford 11115.35’ (Stage 3 and 4)

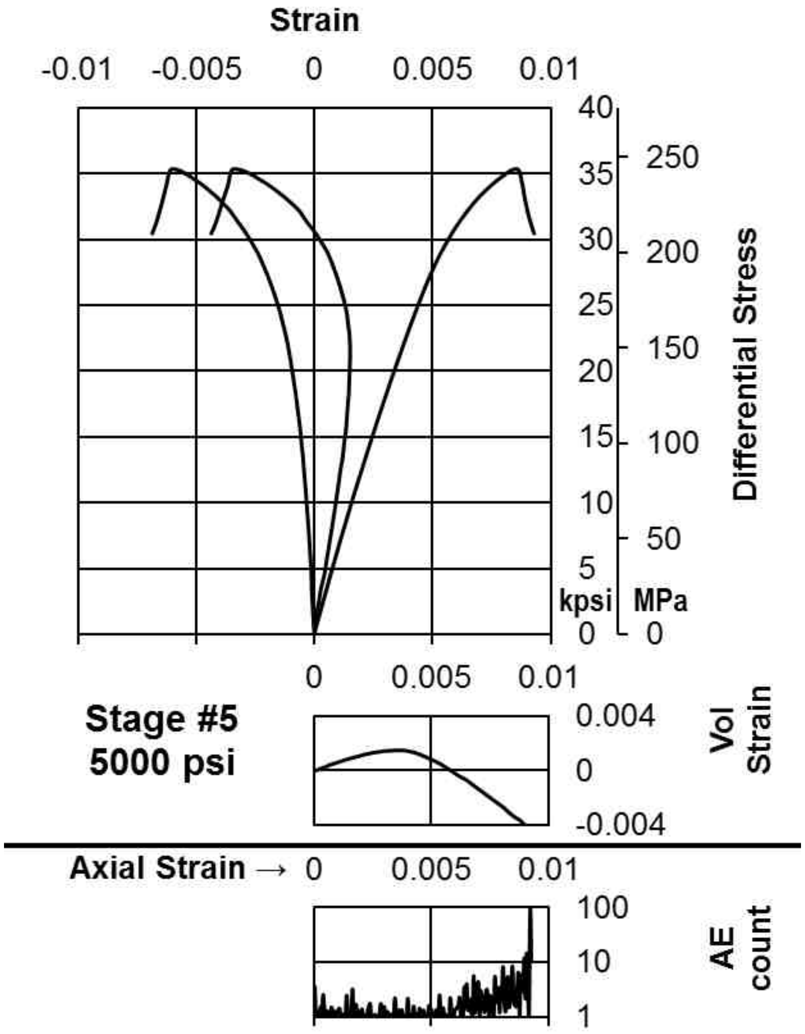

Figure AII-II.6c Stress-strain curves of Eagle Ford 11115.35’ (Stage 5)

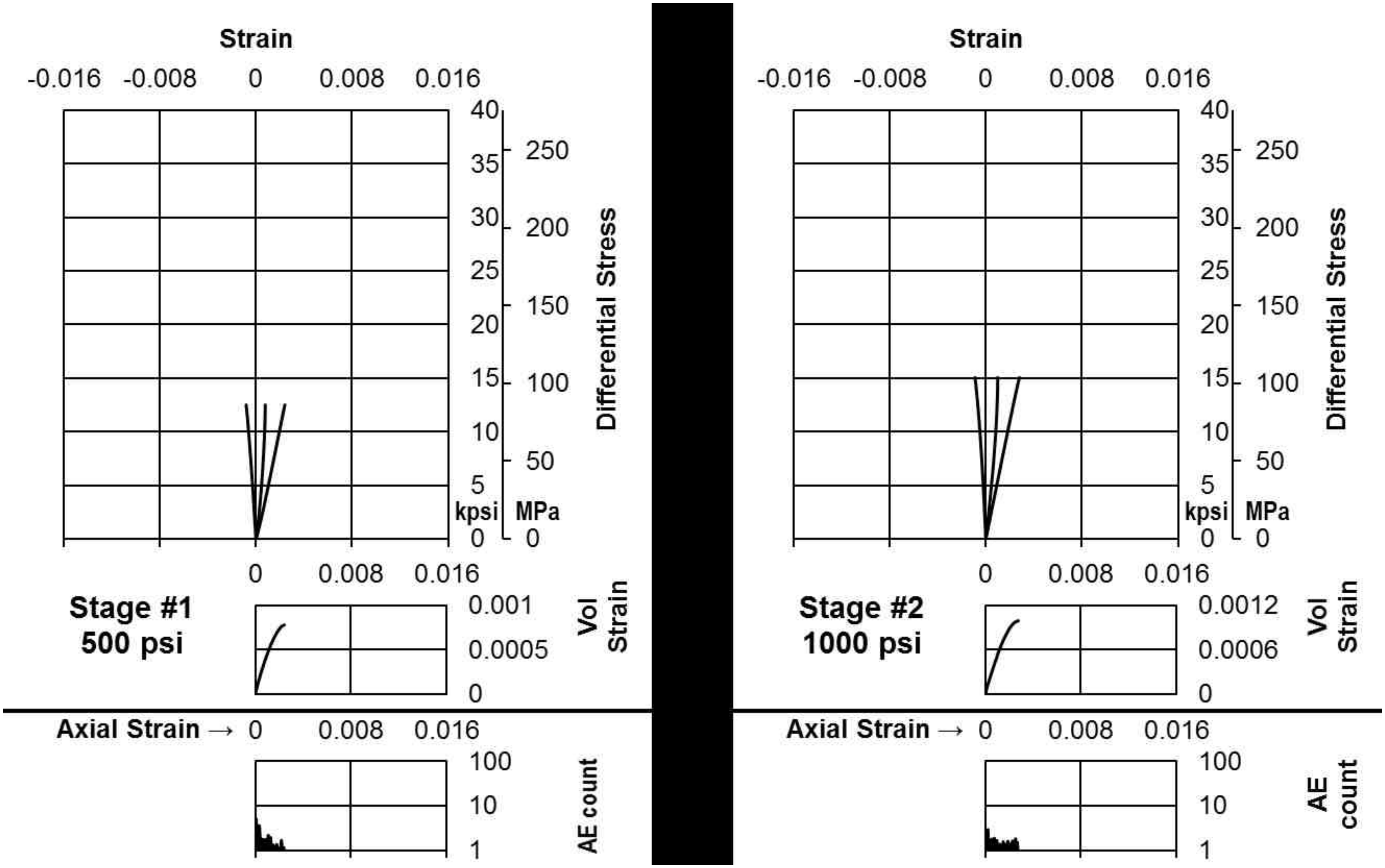

Figure AII-II.7a Stress-strain curves of Eagle Ford 11204.47’ (Stage 1 and 2)

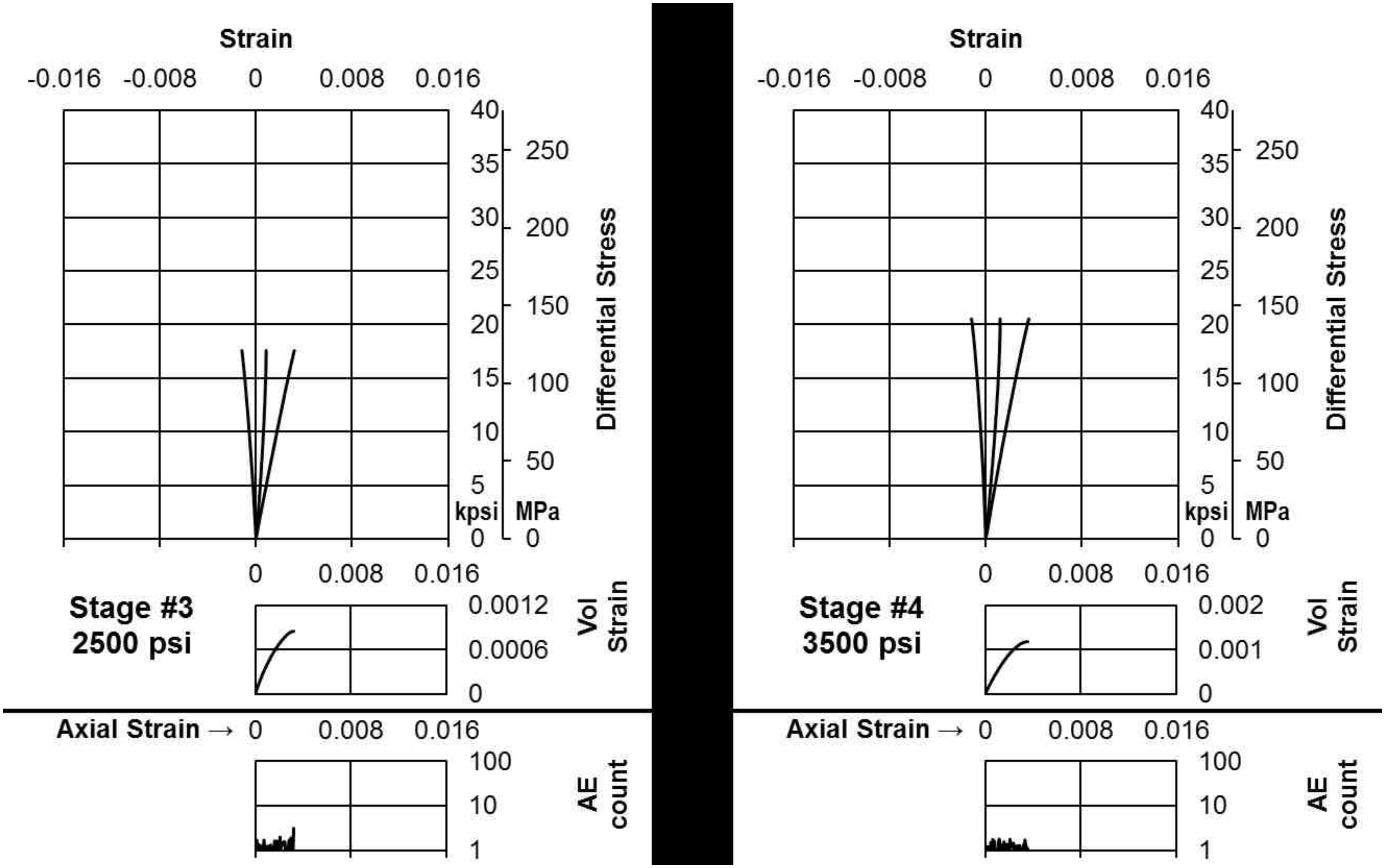

Figure AII-II.7b Stress-strain curves of Eagle Ford 11204.47’ (Stage 3 and 4)

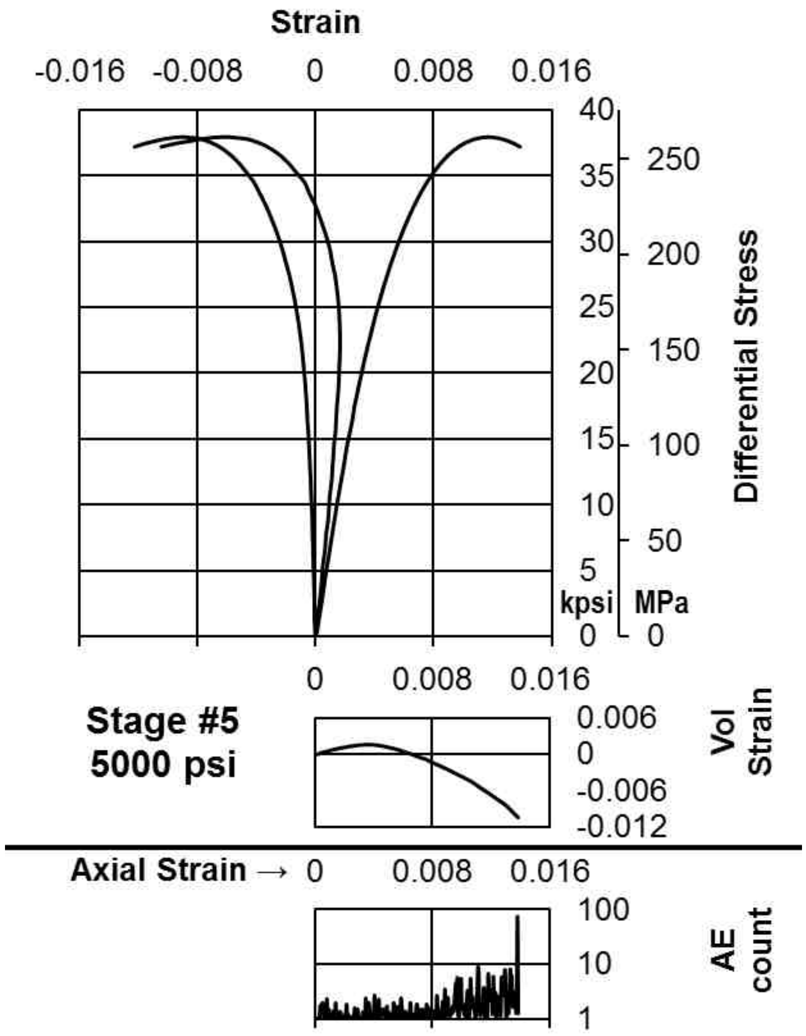

Figure AII-II.7c Stress-strain curves of Eagle Ford 11204.47’ (Stage 5)

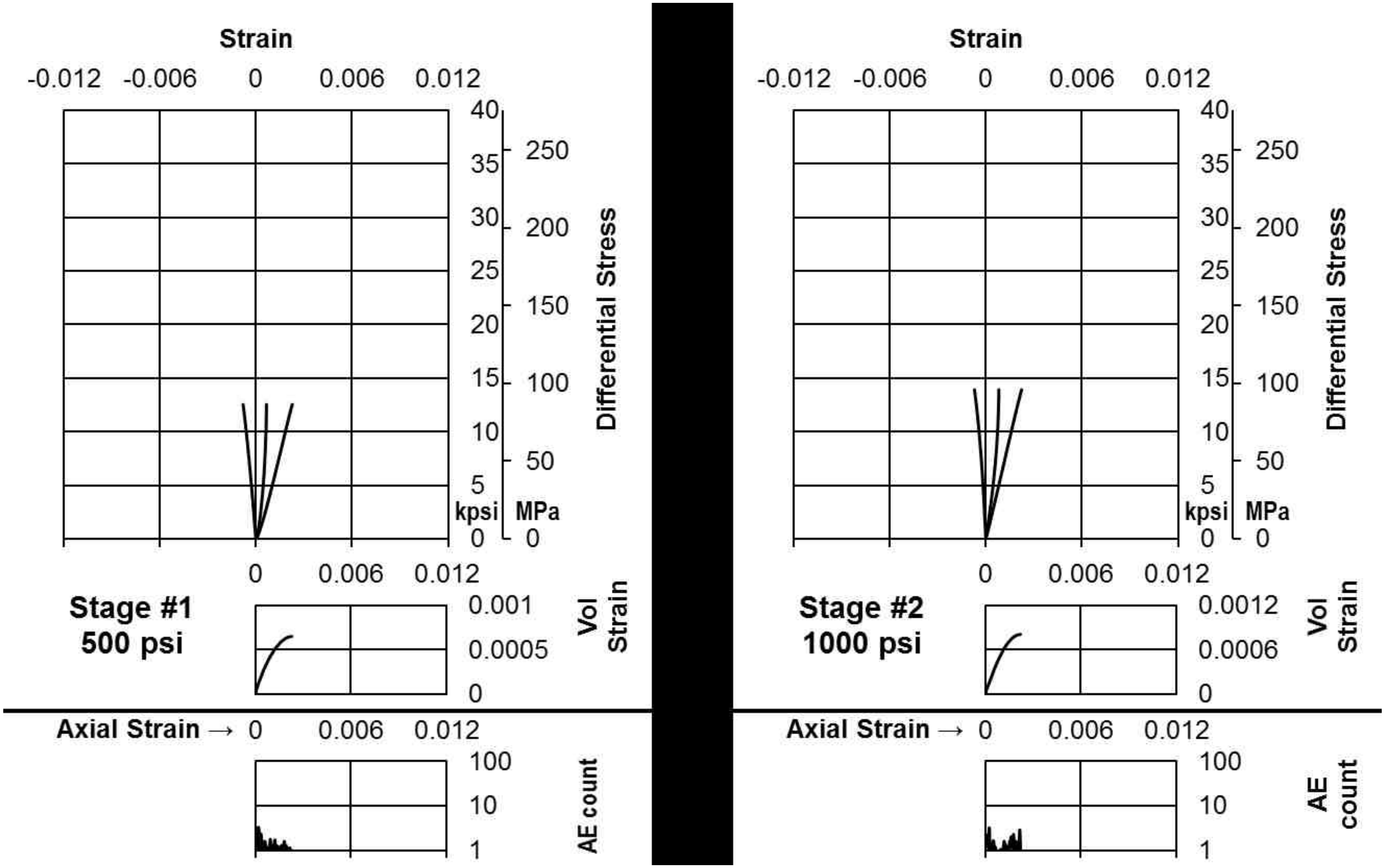

Figure AII-II.8a Stress-strain curves of Eagle Ford 11216.15’ (Stage 1 and 2)

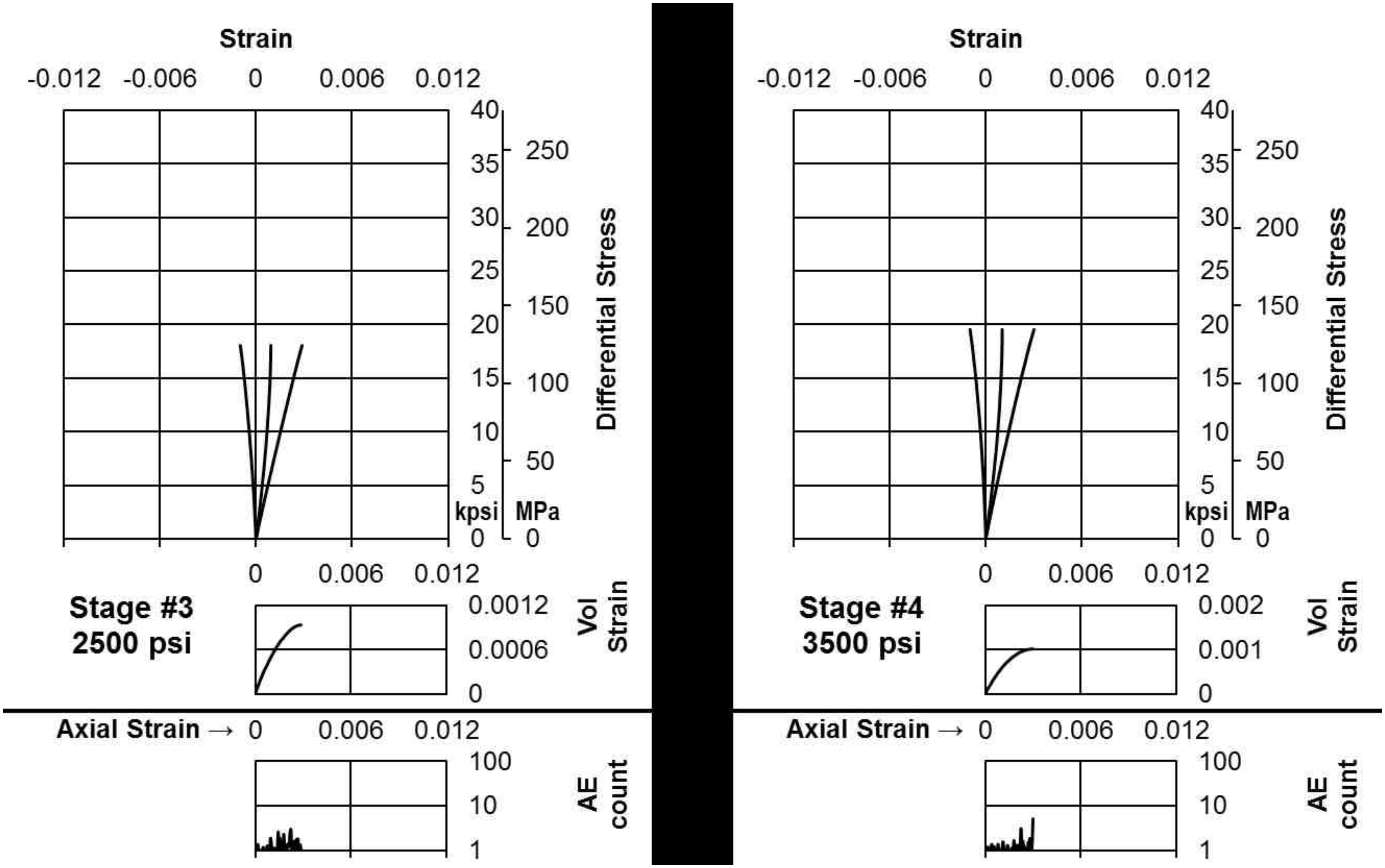

Figure AII-II.8b Stress-strain curves of Eagle Ford 11216.15' (Stage 3 and 4)

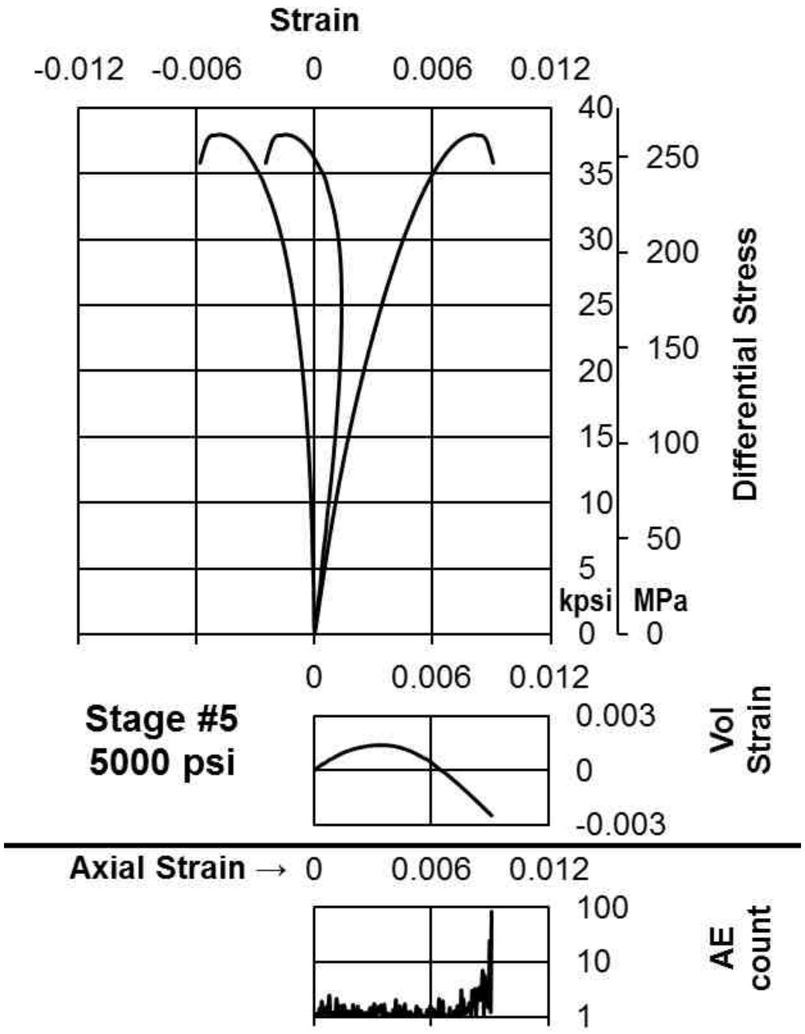

Figure AII-II.8c Stress-strain curves of Eagle Ford 11216.15’ (Stage 5)

Appendix III: Sample Photographs

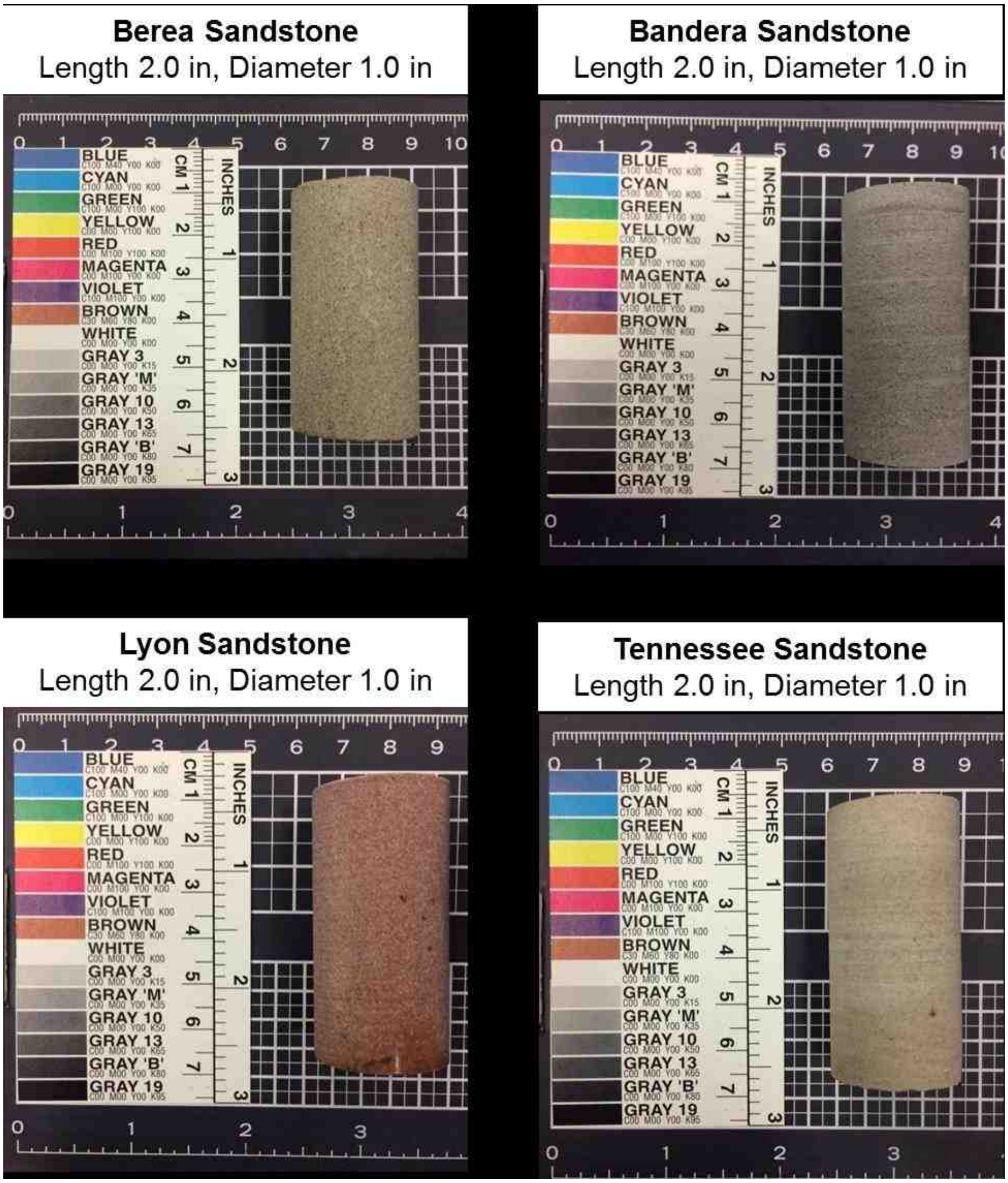

Berea Sandstone
Length 2.0 in, Diameter 1.0 in

Bandera Sandstone
Length 2.0 in, Diameter 1.0 in

Lyon Sandstone
Length 2.0 in, Diameter 1.0 in

Tennessee Sandstone
Length 2.0 in, Diameter 1.0 in

Figure AIII.1 Photographs of the tested sandstones

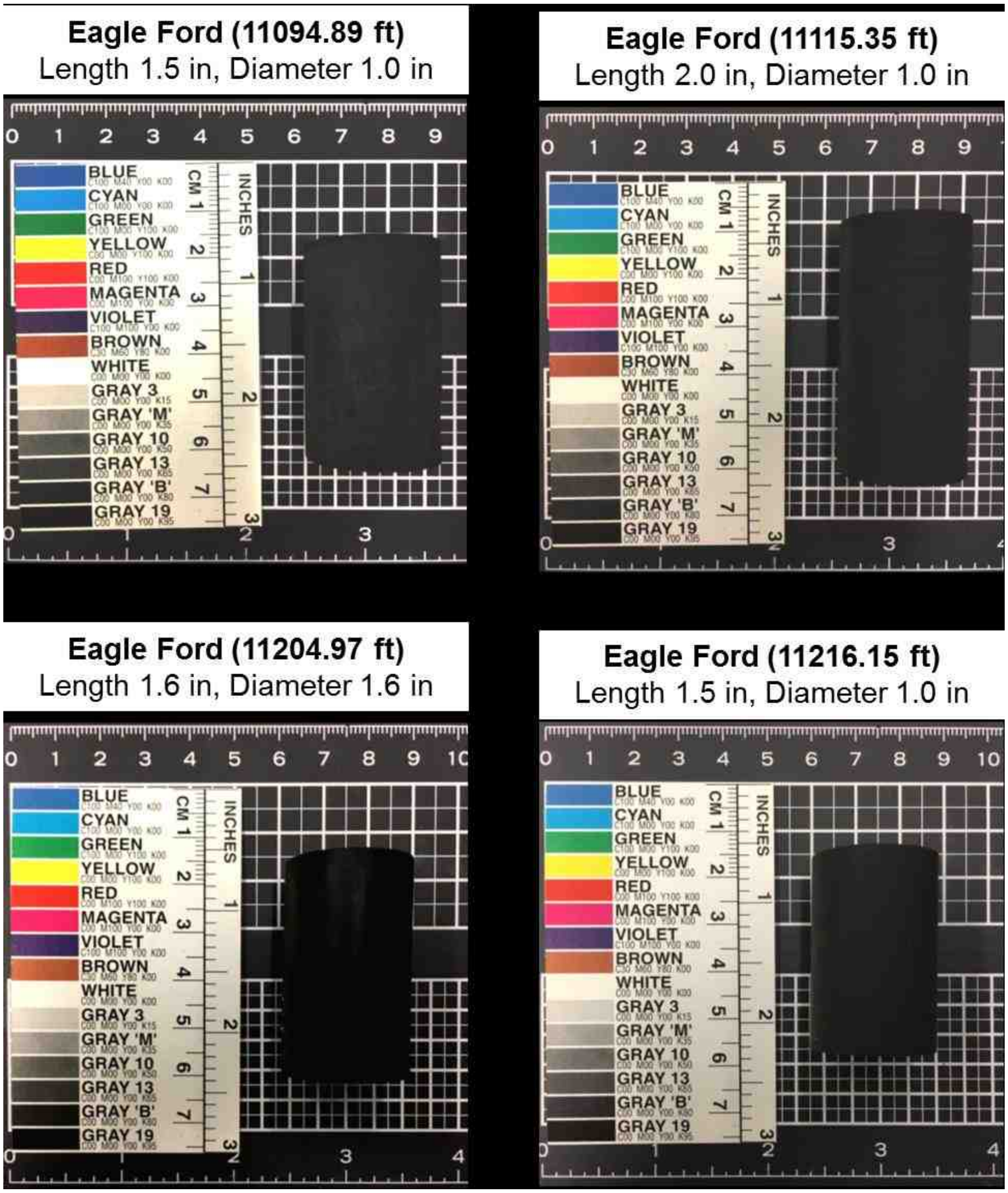

Eagle Ford (11094.89 ft)
Length 1.5 in, Diameter 1.0 in

Eagle Ford (11115.35 ft)
Length 2.0 in, Diameter 1.0 in

Eagle Ford (11204.97 ft)
Length 1.6 in, Diameter 1.6 in

Eagle Ford (11216.15 ft)
Length 1.5 in, Diameter 1.0 in

Figure AIII.2 Photographs of the tested Eagle Ford shale samples

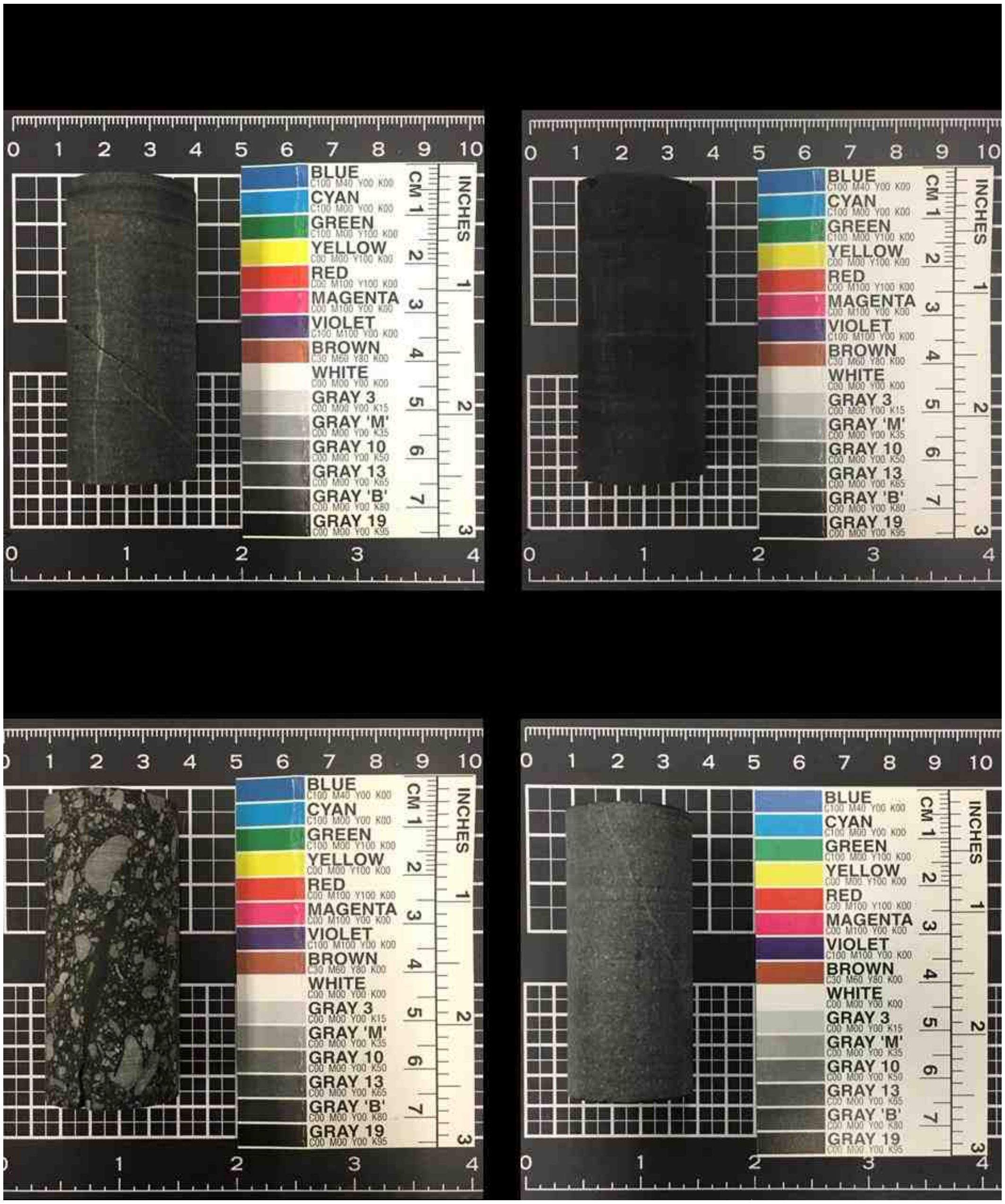

Figure AIII.3 Photographs of the tested Woodford shale samples